CARDIAC MOTION RECOVERY FROM MAGNETIC RESONANCE IMAGES USING INCOMPRESSIBLE DEFORMABLE MODELS

A Dissertation
Presented to
The Academic Faculty

By

Arnaud Bistoquet

In Partial Fulfillment
of the Requirements for the Degree
Doctor of Philosophy
in
Electrical and Computer Engineering

School of Electrical and Computer Engineering
Georgia Institute of Technology
August 2008

CARDIAC MOTION RECOVERY FROM MAGNETIC RESONANCE IMAGES USING INCOMPRESSIBLE DEFORMABLE MODELS

Approved by:

Dr. Oskar Škrinjar, Advisor
Department of Biomedical Engineering
Georgia Institute of Technology

Dr. Patricio Vela
School of ECE
Georgia Institute of Technology

Dr. Allen Tannenbaum
School of ECE
Georgia Institute of Technology

Dr. John Oshinski
Department of Biomedical Engineering
Georgia Institute of Technology

Dr. Anthony Yezzi
School of ECE
Georgia Institute of Technology

Date Approved: May 14th, 2008

ACKNOWLEDGMENTS

This thesis would not have been possible without the help and support of many great people. In particular, I would like to thank:

- my advisor Oskar Škrinjar for his genuine support and guidance.
- John Oshinski for his precious help, expertise and all the data that I used for my research work.
- Allen Tannenbaum, Patricio Vela and Tony Yezzi for their support as committee members.
- my parents, my brother, Remi Brunot, and Oly Diaz: thank you for your unconditional love and support.

TABLE OF CONTENTS

LIST OF TABLES

LIST OF FIGURES

SUMMARY

Cardiovascular diseases remain the leading cause of mortality in the United States. The study of myocardial motion is essential for understanding the normal heart function and developing new treatments for cardiovascular diseases. The goals of my PhD research is to develop new methods for cardiac deformation recovery from 3D magnetic resonance (MR) images. Cine magnetic resonance imaging (MRI) is widely used for the analysis of the cardiac function because of its high soft tissue contrast as compared to other acquisition techniques and relatively short acquisition time as compared to other cardiac MRI methods.

The main contribution of my work is that the proposed methods are guaranteed to generate exactly or nearly incompressible deformations. This is a desirable property since the myocardium has been shown to be close to incompressible. The myocardium needs to be segmented in an initial frame after which the methods automatically determine the tissue deformation everywhere in the myocardium throughout the cardiac cycle. From the recovered deformation, one can directly compute a number of clinically useful parameters, including strains. Two studies were conducted to validate the methods. In the first study, the deformation recovered from a 3D anatomical cine MRI of a healthy volunteer were compared against the manual segmentation of the cardiac wall and against the corresponding 3D tagged cine MRI. Another set of 3D anatomical and tagged MRI scans was taken of the same volunteer four months later. In the second study, the methods were applied to 3D anatomical cine MRI scans of three patients with ventricular dyssynchrony and three age-matched healthy volunteers.

The first method for 3D deformation recovery of the left ventricular wall (LV) from anatomical cine MRI is based on a deformable model that is incompressible. This method is not suitable for the deformation recovery of the biventricular wall. The second method is based on a 3D deformable model that is nearly incompressible. The model uses a matrix-valued radial basis function to represent divergence free displacement fields, which is a first order approximation of incompressibility. This representation allows for deformation modeling of arbitrary topologies with a relatively small number of parameters, which is suitable for representing the motion of the multi-chamber structure of the heart. The

two methods have similar performance. For the first study, the average volume agreement between the models and the manual segmentation had an average false positive rate of 3%, false negative rate of 3% and true positive rate of 92%. The average distance between the models and manually determined intersections of perpendicular tag planes was 1.6 mm (1.1 pixel). The methods were applied to the second set acquired four months later and the recovered deformations were very similar to the ones obtained from the first set. For the second study, the myocardium wall deformations recovered for the three normals agreed well and the recovered strains were similar to those reported by other researchers for normal subjects. Strains and displacements of the three patients were clearly smaller than those of the three normals indicating reduced cardiac function. The deformations recovered for the three normals and the three patients were validated against manual segmentation and corresponding tag cine MRI scans and the agreement was similar to that of the first validation study.

A method to obtain a smooth and accurate surface of the myocardium wall is needed to illustrate the cardiac deformation recovery. Thus, I present a novel method for the generation of endocardial and epicardial surface meshes. The method has been tested on 3D short-axis cardiac magnetic resonance images with strongly anisotropic voxels in the long-axis direction. The same algorithm is independently used to generate the surface meshes of the epicardium and endocardium of the four cardiac chambers. It provides smooth meshes of the heart chambers despite the strong voxel anisotropy, which is not the case for the marching cubes algorithm. While the proposed method generates more regular mesh triangles than the marching cubes and allows for a complete control of the number of triangles, the generated surface meshes are still close to the ones obtained by the marching cubes. For the five tested cases, the average distance between the surfaces generated by our method and by the marching cubes algorithm was 0.4 mm.

Phase velocity MRI is an acquisition technique that contains more information about the myocardial motion than cine MRI. Thus, I present a method to interpolate the velocity vector field in a phase velocity MRI sequence that can be used for cardiac deformation

recovery. The method uses the divergence free interpolation model presented in the biventricular deformation recovery. The divergence free interpolation provides a continuous velocity vector field that is divergence free, which means that the corresponding deformation is incompressible, a desirable property since the myocardium has been shown to be close to incompressible. The method has been tested on three simulated cases and three real cases. The interpolation obtained is close to the original vector field in terms of difference in magnitude and angle. Furthermore, it is more accurate than the interpolation given by thin-plate spline because of its divergence free property.

CHAPTER 1
INTRODUCTION

1.1 Motivation

Cardiovascular diseases remain the leading cause of mortality in the United States [1]. The cost of the associated health care and lost productivity is more than 3% of the gross domestic product [2]. The study of myocardial motion, both left ventricle (LV) and right ventricle (RV), is essential for understanding the normal heart function and developing new treatments for cardiovascular diseases. While several cardiac imaging techniques have been developed (see Sec. 1.2), this thesis deals with cardiac motion recovery from cine magnetic resonance images (MRI). Cine MRI is widely used for analysis of the cardiac function because of its high soft tissue contrast as compared to other acquisition techniques and relatively short acquisition time as compared to other cardiac MRI acquisition techniques. Acquisition techniques like tagged and phase velocity MRI contain more information about the myocardial motion than cine MRI, but they are not widely used and typically they were not acquired when existing databases of cardiac MR images were acquired, in which case cine MRI remains the only option for the analysis of the myocardial motion. For this reason, the proposed methods are suitable for both prospective and retrospective cardiac deformation analysis.

1.2 Image Acquisition for Cardiac Deformation Recovery

Several methods for imaging the myocardial motion have been developed. They span all standard medical imaging modalities: ultrasound, nuclear-based techniques, computed tomography and magnetic resonance imaging.

Echocardiography is an application of ultrasound to the heart. It is fast and fairly inexpensive. However, the method has a low soft tissue contrast and low signal-to-noise ratio in the far field. Since ultrasound is severely attenuated in air and bone, only limited views of the heart can be obtained. If tissue Doppler imaging is done in conjunction with echocardiography, quantitative values for wall velocity can be obtained, but only in one direction (toward the transducer) and only in selected locations within the myocardial

wall. Despite the limitations, echocardiography is the second most frequently performed diagnostic procedure after electrocardiography [2].

Gated single photon emission computed tomography can be used to quantify the biventricular myocardial wall motion and thickening but it suffers from very poor spatial resolution that causes it to have only fair accuracy and reproducibility [2].

Cardiac computed tomography allows for multi-slice imaging of the heart at multiple time points over the cardiac cycle, which can be used for motion analysis. The drawbacks to the technique are that iodinated contrast agent must be used to generate good contrast between the blood and myocardium and the patient must be exposed to a relatively large dose of ionizing radiation [2].

There are five MRI-based acquisition techniques that can be used to analyze cardiac motion: cine, tagged, phase velocity, displacement-encoded (DENSE), and strain-encoded (SENC) MRI. Cine MRI can cover the entire cardiac anatomy and can generate high temporal resolution images over the entire cardiac cycle. It is by far the most frequently used cardiac MRI technique because of its high reproducibility, high soft-tissue contrast, and good spatial and temporal resolution [2]. Myocardial tagging can be used to lay down a set of grid lines on the myocardium by modulating the magnetization, and cine images showing the deformation of the tag lines can then be acquired [3, 4]. Phase velocity MRI can be used to acquire velocity of the myocardial tissue [5, 6]. Displacement-encoded MRI allows for imaging of the myocardial displacement [7]. Strain-encoded MRI can be used to acquire through-plane myocardial strain [8]. Tagged, phase velocity, displacement-encoded, and strain-encoded MRI are not widely used and are always acquired in addition to cine MRI.

1.3 Relevant Image Analysis Methods for Cardiac Deformation Recovery

Recovery of cardiac deformation from images has received considerable attention. Researchers have worked on cardiac deformation recovery methods that use tagged MRI [9, 10, 11, 12, 13], phase velocity MRI [14], and echocardiography [15, 16, 17].

Cine MRI has also been used for automated computation of cardiac function. Some of these methods provide only the segmentation of the myocardium without recovering the

displacement field [18, 19, 20, 21]. This prevents one from computing myocardial strain fields, which are critical for analysis of the cardiac function. In addition, there are methods that track only the endocardial and epicardial surfaces [22, 23] without computing the displacements within the heart wall. These methods also can not be used to compute myocardial strains.

In [24], we presented an automated 3D myocardial deformation recovery from cine MRI. In this paper, we presented a deformable model that is incompressible. The method uses a curvilinear coordinate system based on the midsurface of the LV wall. For this reason, the method can not be directly applied to the biventricular wall. In [25] we used a composition of two such incompressible transformations to recover the biventricular wall deformation. However, the composing of transformations led to complicated computations and the exact incompressibility made the optimization sensitive to the optimization parameters.

In Medical Image Computing and Computer-Assisted Intervention (MICCAI) conference in 2002, Lorenzo-Valdes et al. [26] presented an automated method for segmentation and tracking of cardiac deformation from cine MRI. They modeled the frame-to-frame 3D heart deformation using cubic B-splines (as proposed by the same group for the registration of breast MR images [27]) and obtained the model parameters by maximizing the normalized mutual information [28]. The method propagates the segmentation from the first frame to the rest of the cardiac cycle. The authors correlated the volume of the manual segmentation of the myocardium to the one obtained automatically by the method and reported the r value of .98 and .83, for the case of manual or atlas-based segmentation of the first frame, respectively.

Researchers have developed methods for 3D cardiac deformation recovery from cine MRI that require a considerable amount of user input, i.e. that cannot be considered fully automated. The method by Papademetris et al. [29] requires the user to manually segment the myocardium in all the slices and all the frames of the image sequence, the method by Remme et al. [30] requires the user to manually track a set of 3D points throughout the cardiac cycle, and the method by Shen et al. [31] uses the knowledge of the boundaries between the myocardium and blood pool and the myocardium and surrounding structures, which is equivalent to segmentation. It is desirable that the method automatically recovers

the myocardial deformation in all the frames of the cardiac cycle.

1.4 Incompressibility of the Myocardium

The myocardium is a nearly incompressible material. Its constituents are mainly composed of water, which is almost perfectly incompressible. However, the myocardium is perfused with blood, which affects the total myocardial volume over the cardiac cycle. A few independent studies [32, 33, 34, 35, 36] have been carried out to quantify the change of the myocardial volume over the cardiac cycle. The common conclusion of these efforts is that the total myocardial volume changes no more than 4% during a cardiac cycle. This means that the myocardium is not perfectly incompressible. However, this volume change is relatively small and it is distributed in all three directions. Even in the regions with predominant orientation of the blood vessels, the myocardial tissue does not expand or contract by more than 2% in any direction. For this reason, one can conclude that "incompressibility" is not simply another approach to cardiac deformation recovery; near incompressibility is a physical property of the myocardium that should not be ignored. Thus, any method that recovers myocardial deformation that deviates from incompressibility by more than a few percents cannot be correct. It should be noted that near incompressibility itself is not enough to guarantee correct cardiac deformation recovery, i.e. near incompressibility is a necessary but not a sufficient constraint. The proposed methods are directly based on this property.

CHAPTER 2

LEFT VENTRICULAR DEFORMATION RECOVERY FROM CINE MRI USING AN INCOMPRESSIBLE MODEL

2.1 Methods

2.1.1 Notation

Scalars are denoted with regular face (e.g. x, y), vectors with bold face (e.g. $\mathbf{r}, \mathbf{p}$) and unit vectors are distinguished with a hat (e.g. $\hat{\mathbf{u}}, \hat{\mathbf{n}}$). All the quantities in the reference configuration are denoted with lower case letters (e.g. γ, $\mathbf{r}$) and all the quantities in the current configuration are denoted with upper case letters (e.g. Γ, $\mathbf{R}$). The reference configuration is by convention the configuration of the LV wall at end-diastole (ED) and the current configuration is the configuration of the LV wall at any other time point in the cardiac cycle.

2.1.2 Midsurface Curvilinear Coordinate System

The proposed method uses a curvilinear coordinate system that is based on the midsurface of the LV wall. To construct the midsurface, one needs to segment the LV wall in the first frame of the sequence. An example of the LV wall segmentation is shown in Fig. 1. Once the LV wall is segmented, the midsurface is generated by interpolating the nodes placed in the middle of the segmented LV wall. For each slice, except for the slice going through the apex, a 2D skeleton[1] of the LV wall is constructed and then nodes uniformly spaced around the circular skeleton (Figs. 2b and 2c). For the slice going through the apex we place one node in the center of the segmented region (Fig. 2a). To interpolate the midsurface nodes, we use the pseudo thin plate splines (see Appendix A). We first compute the center of the LV as the barycenter of the segmented LV wall. Let there be M midsurface nodes with position vectors $\mathbf{m}_i,\ i = 1, \ldots, M$ and let $\mathbf{p}$ denote the LV center. The unit vectors and distances of the nodes are

$$\hat{\mathbf{u}}_i = \frac{\mathbf{m}_i - \mathbf{p}}{||\mathbf{m}_i - \mathbf{p}||}, \tag{2.1}$$

$$l_i = ||\mathbf{m}_i - \mathbf{p}||, \tag{2.2}$$

[1]For this purpose we computed the morphological skeleton for binary images using Matlab command bwmorph.

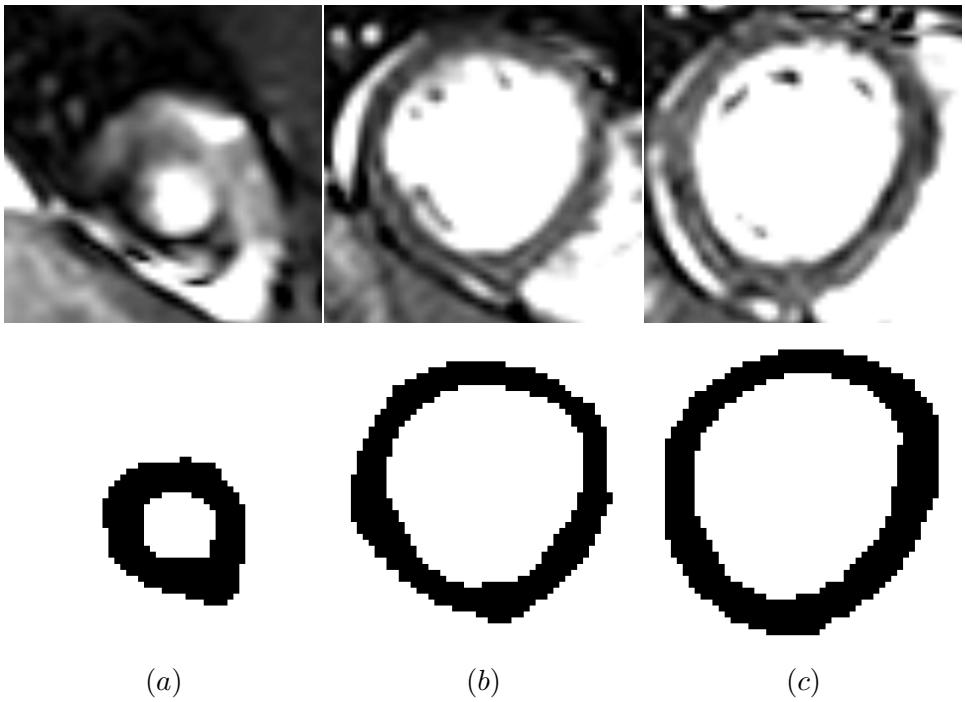

Figure 1. The LV wall is segmented in the first frame. The top row shows three image slices in the first frame and the bottom row shows the corresponding segmentations. Column (a) shows a slice in the apical region, column (b) shows a slice in the midventricular region, and column (c) shows a slice in the basal region.

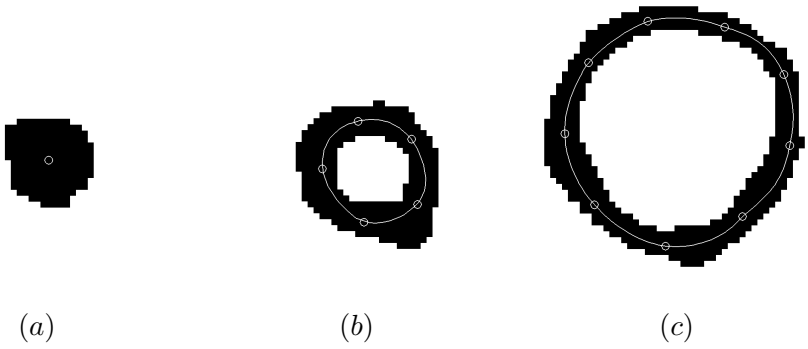

Figure 2. Midsurface nodes (white circles) were placed in each slice containing the LV wall. In the slice going through the apex (a) one node was placed in the center of the myocardial tissue. In the remaining slices the nodes were uniformly spaced around the circular skeleton, as shown in (b) and (c). Note that the LV wall cross-section in (b) is smaller than the LV wall cross-section in (c) and consequently it has fewer nodes. Once all the nodes were placed, the midsurface was obtained by the pseudo thin plate spline interpolation of the nodes. The white contours in (b) and (c) represent midsurface cross-sections.

respectively. We interpolate the data points $(\hat{\mathbf{u}}_i, l_i)$ using the pseudo thin plate splines on the sphere to obtain the distance function $l(\hat{\mathbf{u}})$. Then, the point on the midsurface in the direction $\hat{\mathbf{u}}$ is

$$\mathbf{m}(\hat{\mathbf{u}}) = \mathbf{p} + l(\hat{\mathbf{u}})\hat{\mathbf{u}}. \tag{2.3}$$

A midsurface obtained this way is shown in Fig. 4b together with the midsurface nodes. The representation given by Eq. 2.3 is limited to surfaces that have at most one intersection point with any given direction $\hat{\mathbf{u}}$, which is the case with the LV wall midsurface. It should be noted that this surface representation is coordinate system independent since it is given in terms of vectors and it does not have special points (e.g. the two poles in the spherical coordinate system surface representation require special treatment). This allows for equal treatment of any part of the midsurface from the apex to the base. One can compute the surface normal, principal, mean and Gaussian curvatures and any other local surface property as functions of $\hat{\mathbf{u}}$ from the surface representation given by Eq. 2.3.

Any point within the LV wall, i.e. between the endocardial surface and epicardial surface can be represented as

$$\mathbf{r}(\hat{\mathbf{u}}, \gamma) = \mathbf{m}(\hat{\mathbf{u}}) + \gamma\hat{\mathbf{n}}(\hat{\mathbf{u}}), \tag{2.4}$$

where γ is the signed distance of the point from the surface and $\hat{\mathbf{n}}(\hat{\mathbf{u}})$ is the surface normal at the point $\mathbf{m}(\hat{\mathbf{u}})$. We use the outward normal convention, which means that γ is positive for points outside the midsurface and negative for points inside the midsurface. For points at the midsurface $\gamma = 0$. Eq. 2.4 defines a curvilinear coordinate system that is based on the LV wall midsurface. The independent variables of this representation are $\hat{\mathbf{u}}$ and γ. Since $\hat{\mathbf{u}}$ is a unit vector it has two degrees of freedom and γ, being a scalar, has one degree of freedom. Thus, the independent variables have three degrees of freedom, the same as the Cartesian coordinates. The midsurface curvilinear coordinate system is illustrated in Fig. 3. Eq. 2.4 is a mapping from the curvilinear coordinates $\hat{\mathbf{u}}$ and γ to $\mathbf{r}(\hat{\mathbf{u}}, \gamma)$, which we represent with three Cartesian coordinates x, y and z. The inverse mapping (from the Cartesian to the curvilinear coordinates) cannot be obtained analytically and it can be computed numerically. However, for the cardiac deformation recovery we need to use only the forward mapping given by Eq. 2.4. It should be noted that the mapping between the

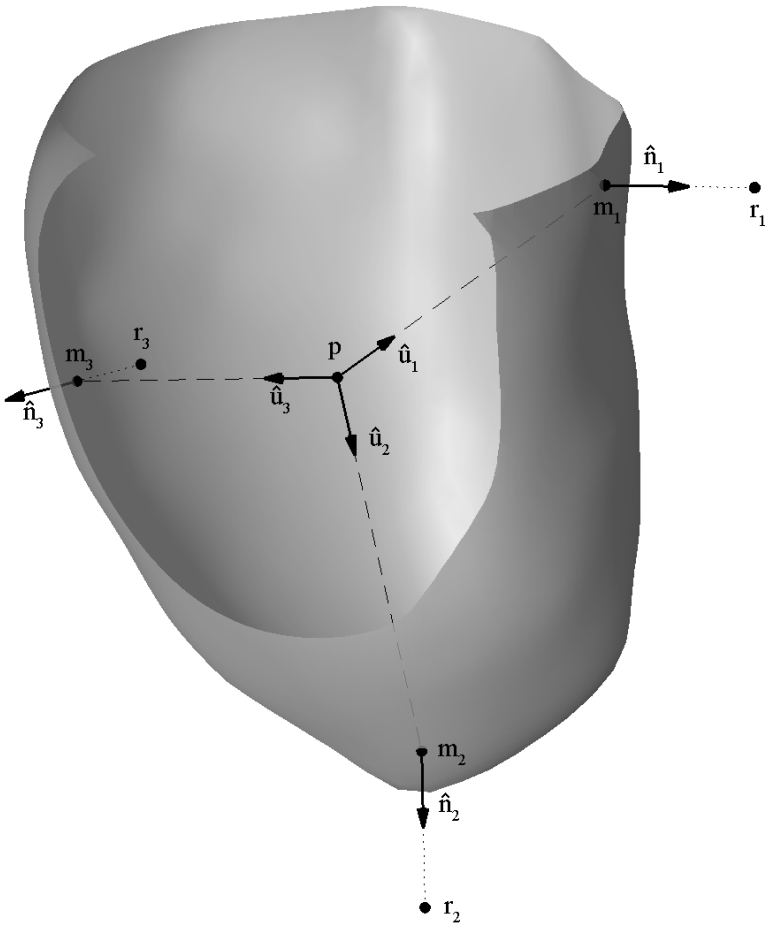

Figure 3. Three points $\mathbf{r}_1$, $\mathbf{r}_2$, and $\mathbf{r}_3$ in the midsurface curvilinear coordinate system are shown together with the partly cut midsurface. The LV center p and the three unit vectors $\hat{\mathbf{u}}_1$, $\hat{\mathbf{u}}_2$, and $\hat{\mathbf{u}}_3$ can be seen through the surface opening. The points on the midsurface corresponding to the three unit vectors are $\mathbf{m}_1$, $\mathbf{m}_2$, and $\mathbf{m}_3$, respectively. Their positions are given by Eq. 2.3. The first point is in the basal region, the second point is in the apical region, and the third point is in the midventricular region. The respective surface normals are $\hat{\mathbf{n}}_1$, $\hat{\mathbf{n}}_2$, and $\hat{\mathbf{n}}_3$. The coordinates γ_1, γ_2, and γ_3 define the signed distance from the midsurface of points $\mathbf{r}_1$, $\mathbf{r}_2$, and $\mathbf{r}_3$, respectively. Their positions are given by Eq. 2.4. Note that points $\mathbf{r}_1$ and $\mathbf{r}_2$ are outside the midsurface and point $\mathbf{r}_3$ is inside the midsurface, which means that $\gamma_1 > 0$, $\gamma_2 > 0$, and $\gamma_3 < 0$. Points within the LV wall are closer to the midsurface than the three shown points.

curvilinear and the Cartesian coordinates in general is not one-to-one. This happens for points far away from the midsurface or in vicinity of highly curved parts of the midsurface. Since the midsurface is not very curved and the LV wall is not very thick, the mapping between the two coordinate systems over the LV wall is one-to-one.

2.1.3 Incompressible Transformation

2.1.3.1 Midsurface Mapping

To obtain the transformation from the domain in the reference configuration (the segmented LV wall) to the current configuration, we first establish the mapping of the midsurface. Let the midsurface nodes $\mathbf{m}_i$ in the reference configuration be displaced by displacements $\mathbf{d}_i$ to the corresponding locations $\mathbf{M}_i$ in the current configuration, i.e.

$$\mathbf{M}_i = \mathbf{m}_i + \mathbf{d}_i,\ i = 1, \ldots, M. \tag{2.5}$$

We interpolate displacements $\mathbf{d}_i$ component-wise[2] using the pseudo thin plate spline interpolation on the sphere to obtain the midsurface displacement function $\mathbf{d}(\hat{\mathbf{u}})$. The midsurface in the current configuration is given by

$$\mathbf{M}(\hat{\mathbf{u}}) = \mathbf{m}(\hat{\mathbf{u}}) + \mathbf{d}(\hat{\mathbf{u}}), \tag{2.6}$$

where $\mathbf{m}(\hat{\mathbf{u}})$ is given by Eq. 2.3. Note that the same unit vector $\hat{\mathbf{u}}$ figures/TMI in $\mathbf{m}(\hat{\mathbf{u}})$ and in $\mathbf{M}(\hat{\mathbf{u}})$, which means that they are corresponding midsurface points in the reference and current configuration, respectively. The mapping of the midsurface is illustrated in Fig. 4.

2.1.3.2 Assumptions

To uniquely define a transformation from the domain in the reference configuration to the current configuration that maps the midsurface $\mathbf{m}(\hat{\mathbf{u}})$ in the current configuration to the corresponding midsurface $\mathbf{M}(\hat{\mathbf{u}})$ in the current configuration we make the following two assumptions:

- *Incompressibility:* this is a physical property of the myocardium (see Section 1.4).
- *No transmural bending:* any point in the domain remains at the normal direction to the same point on the midsurface as the midsurface deforms. It should be noted that

[2]Component-wise interpolation of vectors is interpolation of their x, y, and z components independently.

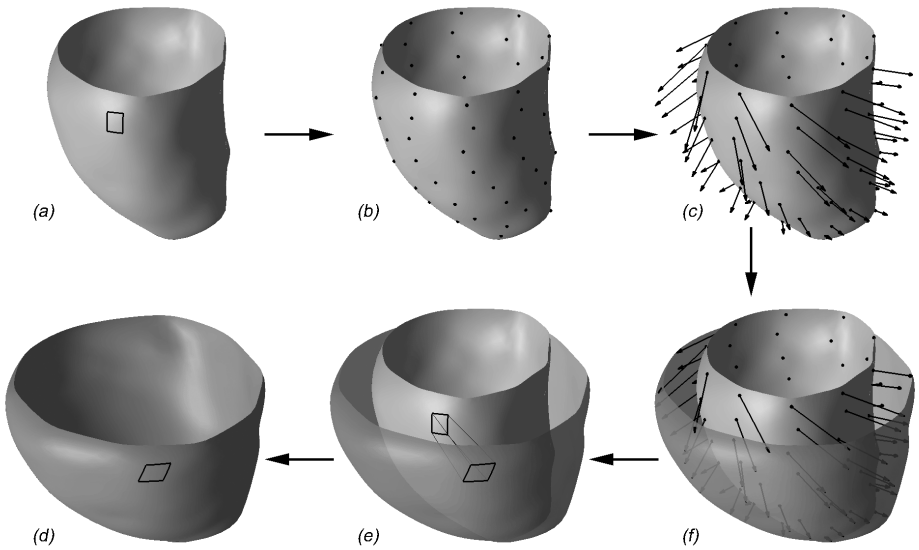

Figure 4. Mapping of the midsurface: (a) the LV wall midsurface of a normal subject in the reference configuration with an embedded curvilinear rectangle; (b) the midsurface in the reference configuration is obtained by interpolating nodes $\mathbf{m}_i$ shown as black dots; (c) each node is assigned a displacement $\mathbf{d}_i$; (f) the node displacements are interpolated to obtain displacement function $\mathbf{d}(\hat{\mathbf{u}})$, which is then applied to the entire midsurface; (e) $\mathbf{d}(\hat{\mathbf{u}})$ is applied to the curvilinear rectangle; (d) the resulting midsurface in the current configuration with the curvilinear rectangle. The parameters of the midsurface mapping are the node displacements $\mathbf{d}_i$, which can be arbitrarily specified. For illustration purposes, the applied transformation in this figure is artificial and larger than real. It contains radial expansion, longitudinal shortening and a circumferential twist. It can be seen in (e) that the curvilinear rectangle moved outward (radial expansion), downward (longitudinal shortening), rotated to the right and slanted (circumferential twist). The midsurface in the reference configuration is rendered light gray and in the current configuration it is rendered transparent dark gray.

points in the domain can change their distance from the midsurface as the midsurface deforms. This is illustrated in Fig. 5. This assumption results in small (less than 1 %) transmural shear strains for typical deformations of the LV wall. Whereas this assumption is a limitation, anatomical cine MR images do not contain enough information about the myocardial motion to reliably estimate transmural shear strain. Even estimating transmural shear strain from tagged cine MR images is challenging [37], despite the fact that these images contain more information about myocardial motion than anatomical images. Examples of anatomical and tagged MR images are shown in Fig. 6. The fact that transmural shear strain cannot be reliably estimated from anatomical images and the fact that transmural bending is relatively small (Fig. 6d, [37]) justify the "no transmural bending" assumption. An LV wall model that does not assume "no transmural bending", i.e. that allows for larger transmural shear strains, does not necessarily produce more reliable values for transmural shear strain if used with anatomical images given the little information about the transmural shear strain in these images. See Sec. 3.3.1 for additional discussion on this assumption.

Under these two assumptions, the transformation of the LV wall is completely governed by the mapping of the midsurface. This means that the midsurface node displacements define the transformation everywhere in the LV wall, i.e. for given midsurface node locations in the reference configuration, the parameters of the transformation are the midsurface node locations in the current configuration.

2.1.3.3 Domain Mapping

The position of a point in the domain in the reference configuration with curvilinear coordinates $(\hat{\mathbf{u}}, \gamma)$ is given by Eq. 2.4. Assuming "no transmural bending", the position of the corresponding point in the current configuration is

$$\mathbf{R}(\hat{\mathbf{u}}, \gamma) = \mathbf{M}(\hat{\mathbf{u}}) + \Gamma(\hat{\mathbf{u}}, \gamma)\hat{\mathbf{N}}(\hat{\mathbf{u}}), \tag{2.7}$$

where $\hat{\mathbf{N}}(\hat{\mathbf{u}})$ is the normal to the midsurface in the current configuration at point $\mathbf{M}(\hat{\mathbf{u}})$, and $\Gamma(\hat{\mathbf{u}}, \gamma)$ is the distance of point $\mathbf{R}(\hat{\mathbf{u}}, \gamma)$ from the midsurface in the current configuration.

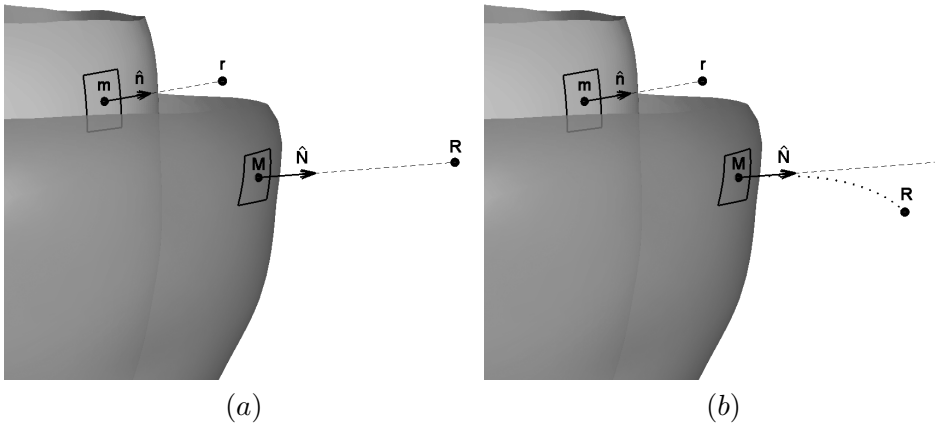

(a) (b)

Figure 5. The midsurface from Fig. 4 in the reference (light gray) and current (transparent dark gray) configuration with the curvilinear rectangle zoomed in are shown in (a) and (b), respectively. They illustrate the mapping of a point r from the domain in the reference configuration to the corresponding point R in the current configuration. Point m is in the center of the curvilinear rectangle in the reference midsurface and the corresponding point in the current configuration is M. Point r is at a certain distance from the midsurface point m in the direction of the surface normal n̂. "No transmural bending" assumption is illustrated in (a): the point in the current configuration corresponding to r is denoted as R and it is at a certain distance from the midsurface point M in the direction of the surface normal N̂. In general, the distance from r to m is different from the distance from R to M. "No transmural bending" assumption does not allow the situation illustrated in (b), where R is no longer at the normal direction from point M. For illustration purposes, the distances of r and R from the midsurface in (a) and (b) are larger than real, i.e. as shown, these points would be outside the LV wall.

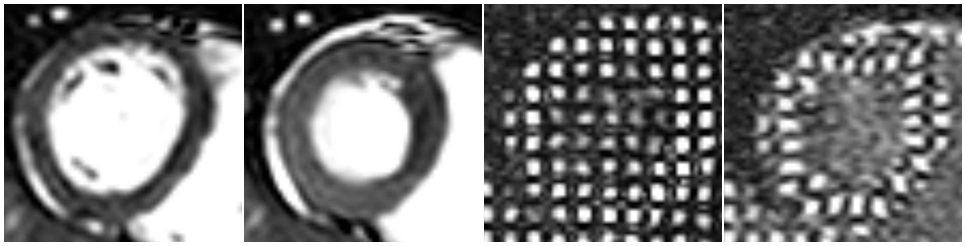

(a) (b) (c) (d)

Figure 6. A basal short axis slice of a healthy volunteer is shown at (a) ED and (b) ES for an anatomical image and at (c) ED and (d) ES for a tagged image. The anatomical image does not contain enough information about the myocardial motion to reliably infer transmural shear strain. Transmural shear strain measures the amount of myocardial bending in the transmural direction. Although the tagged image contains more information about the myocardial motion than the anatomical image, it is still difficult to reliably estimate transmural shear from this image. The position of tag lines at ES relative to their positions at ED allows one to compute the myocardial displacements and relatively reliably determine normal strains. However, to compute transmural shear, one would need to determine how the tag lines bend transmurally, which is challenging given that the bending is relatively small and that the tag lines are thick, sparse, and noisy.

The incompressibility assumption leads to

$$\gamma - h(\hat{\mathbf{u}})\gamma^2 + \frac{1}{3}k(\hat{\mathbf{u}})\gamma^3 = S(\hat{\mathbf{u}})\left[\Gamma - H(\hat{\mathbf{u}})\Gamma^2 + \frac{1}{3}K(\hat{\mathbf{u}})\Gamma^3\right], \tag{2.8}$$

where $h(\hat{\mathbf{u}})$ and $k(\hat{\mathbf{u}})$ are the mean and Gaussian curvatures, respectively, of the midsurface in the reference frame, $H(\hat{\mathbf{u}})$ and $K(\hat{\mathbf{u}})$ are the mean and Gaussian curvatures, respectively, of the midsurface in the current frame, and $S(\hat{\mathbf{u}})$ is the surface Jacobian. The expression for $S(\hat{\mathbf{u}})$ as well as the derivation of Eq. 2.8 are given in Appendix B. Note that h, k, H, K, and S are local properties of the midsurface, i.e. they depend on $\hat{\mathbf{u}}$ only (i.e. on the position on the midsurface) and not on γ. Since the terms in Eq. 2.8 depend on $\hat{\mathbf{u}}$ and γ it follows that the solution of the equation, Γ, is a function of both $\hat{\mathbf{u}}$ and γ. Eq. 2.8 is a cubic equation in Γ and it has three solutions. There are two cases: the three solutions are real or one solution is real and the other two are complex. In the case of three real solutions, two have large values, which leaves the third one as the only one physically possible. In the case of one real and two complex solutions, only the real solution is physically possible. Thus, in either case, only one of the three solutions is physically possible.

In summary, the mapping of the entire domain in the reference configuration to the current configuration is completely defined by the midsurface node positions, which are the parameters of the transformation. To map a point $\mathbf{r}$ in the reference configuration with curvilinear coordinates $(\hat{\mathbf{u}}, \gamma)$ to point $\mathbf{R}$ in the current configuration, one needs to:

- compute $h(\hat{\mathbf{u}})$, $k(\hat{\mathbf{u}})$, $H(\hat{\mathbf{u}})$, $K(\hat{\mathbf{u}})$, and $S(\hat{\mathbf{u}})$,
- solve Eq. 2.8 for Γ,
- compute $\mathbf{M}(\hat{\mathbf{u}})$ and $\hat{\mathbf{N}}(\hat{\mathbf{u}})$, and
- evaluate Eq. 2.7 to obtain $\mathbf{R}$.

The entire transformation can be shortly written as

$$\mathbf{R} = \mathbf{T}(\mathbf{r}). \tag{2.9}$$

By specifying the node positions in the current configuration one can generate various LV wall deformation patterns, some of which are shown in Fig. 25.

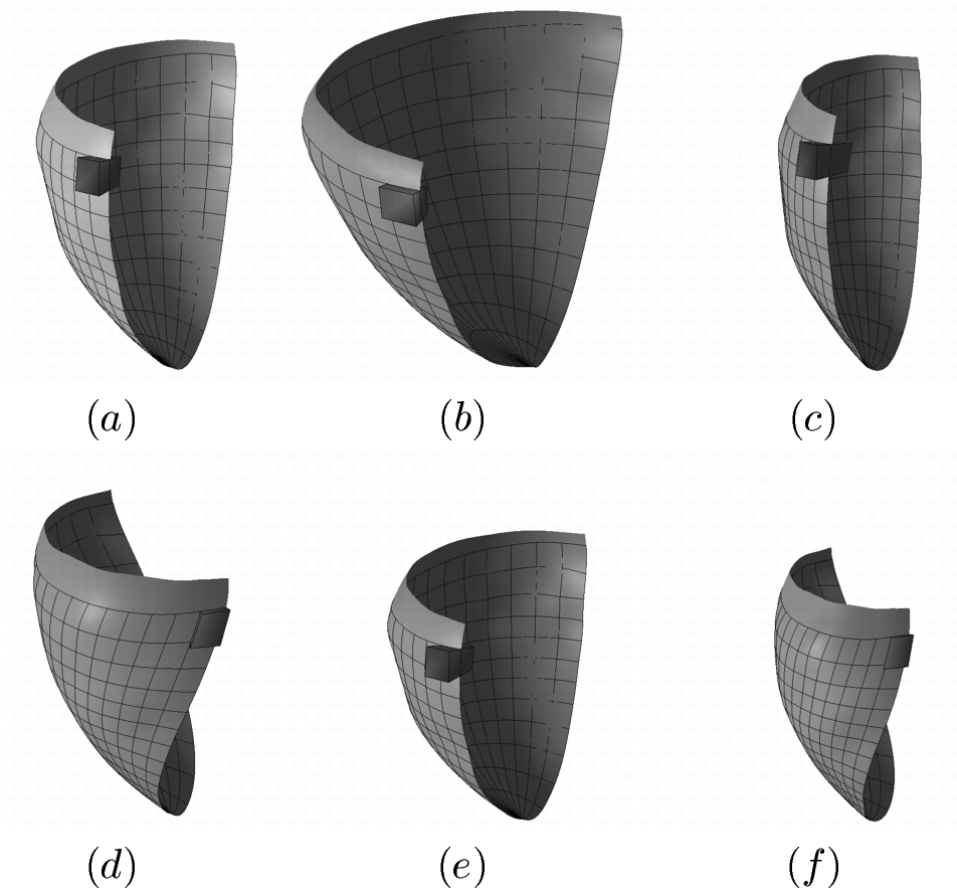

Figure 7. A half of the LV wall midsurface at ED of a healthy volunteer is shown in (a). The dark block represents a chunk of the LV wall. Artificial transformations are applied to the model to illustrate (b) radial expansion, (c) radial contraction, (d) circumferential twisting, (e) longitudinal shortening, and (f) combined radial contraction, circumferential twisting, and longitudinal shortening, which is a deformation pattern typical for ES. Note that the wall (dark block) thins in (b) and thickens in (c) and (e). Although it cannot be seen due to the angle of viewing, the wall undergoes almost no change of the thickness in (d) and it thickens in (f). The thinning and thickening of the wall is a consequence of the model incompressibility. Also note the slanting of the dark block in (d) and (f), which is a consequence of the circumferential twisting. The curvilinear grid is shown to better visualize the deformation patterns.

2.1.4 Left Ventricular Deformation Recovery

The goal of the method is to recover the 3D LV wall deformation from anatomical cine MRI. We model the deformation with the transformation described in Section 2.1.3. The LV wall needs to be segmented in one frame of the sequence, which is called the reference frame. The ED frame of the heart cycle is used as the reference frame by convention.

The cardiac deformation is recovered for each frame j other than the reference frame by searching for the locations of the nodes that define transformation $\mathbf{T}_j$ for which the similarity between the reference frame and the current frame (frame j) is maximized. We use normalized mutual information (NMI) [28] as the similarity measure, which was already used for cardiac deformation recovery [26]. NMI of images I and J is

$$NMI(I, J) = \frac{H(I) + H(J)}{H(I, J)}, \tag{2.10}$$

where $H(I)$ and $H(J)$ are the marginal entropies of I and J, respectively, and $H(I, J)$ is their joint entropy.

Transformation $\mathbf{T}_j$ maps the domain from the reference frame to frame j. For all the frames other than the reference frame one needs to find the node locations that maximize the following objective function:

$$O = NMI(I_1, I_j(\mathbf{T}_j)), \tag{2.11}$$

where I_1 is the image of the reference frame, I_j is the image of frame j, and $I_j(\mathbf{T}_j)$ is the image of frame j transformed by $\mathbf{T}_j$ to the coordinate system of the reference frame. We evaluate NMI over the segmented domain (LV wall at ED) dilated by one pixel layer in each short axis slice. The additional layer of pixels helps recover the twisting of the myocardium.

Let L denote the number of frames (i.e. $j = 1, \ldots, L$). We start the optimization process from the reference frame ($j = 1$) where the locations of the nodes are known. Then, we advance in the forward direction of the cardiac cycle. To determine the locations of the nodes in frame j (for $2 \leq j \leq L$), we use the node locations of the previous frame $j - 1$ as their initial locations and maximize Eq. 2.11 by using a multi-resolution version of the Powell's method [38]. Briefly, one node at a time is test-moved in six directions (positive

and negative x, y, and z directions) with a step size δ, the objective function is evaluated for the seven positions (no movement and the six test-movements), and the node is placed at that of the seven positions that has the highest value of the objective function. This is cyclically applied to all the nodes until no node is moved. Then δ is reduced by a factor of 2 and the entire procedure is repeated. We use four resolutions, i.e. δ values of 2 mm, 1 mm, 0.5 mm, and 0.25 mm. This way we obtain the node locations in each frame j of the cardiac cycle with respect to the forward direction. Let $\mathbf{m}_f(i,j)$ represent the location of the i-th node ($1 \leq i \leq M$, M is the number of nodes) in the j-th frame with respect to the forward direction. We perform the same optimization process in the backward direction, which means that we start from the reference frame where the node locations are known, and we advance in the backward direction of the cardiac cycle. This way we obtain the node locations in each frame j for the backward direction: $\mathbf{m}_b(i,j)$. The backward and forward optimization processes are performed independently of each other.

In the forward propagation errors accumulate in the forward direction, i.e. it is more likely that the nodes in frames 2 and 3 are more accurately positioned than in frames $L-1$ and L. In the backward propagation errors accumulate in the backward direction, i.e. it is more likely that the nodes in frames L and $L-1$ are more accurately positioned than in frames 2 and 1. Note that the reference frame ($j = 1$) has identical node locations for the forward and backward direction. For this reason it makes sense to compute a weighted average of the forward and backward control points such that the forward control points have more weight at the beginning of the cardiac cycle (i.e. for smaller values of j) and the backward control points have more weight at the end of the cardiac cycle (i.e. for larger values of j). A simple way to achieve this is to have the weights linearly depend on the frame number, i.e. the final node locations are given by:

$$\mathbf{m}(i,j) = [1 - w(j)]\, \mathbf{m}_f(i,j) + w(j)\mathbf{m}_b(i,j), \tag{2.12}$$

where $w(j) = \frac{1}{L}(j-1)$. The transformation constructed this way is still incompressible. The accumulated error for this strategy is maximal for the frame in the middle of the sequence. Experiments showed (data not presented) that its value was smaller than the maximal accumulated errors for the forward-only and backward-only strategies.

2.1.5 Computation of Strains

Myocardial normal strain characterizes the amount of deformation of the myocardium in a given direction and it is of particular interest in the study of the heart viability. Typically, the following three types of the myocardial normal strain are used, which correspond to the geometry of the heart:

- circumferential strain, corresponding to the circumferential direction,
- radial strain, corresponding to the transmural direction, and
- longitudinal strain, corresponding to the longitudinal direction.

Lagrangian strain is derived from the Lagrangian tensor,

$$\mathbf{E} = \frac{1}{2}(\mathbf{F}^T\mathbf{F} - \mathbf{I}), \tag{2.13}$$

where $\mathbf{I}$ is the identity tensor and $\mathbf{F}$ is the deformation gradient tensor. The deformation gradient tensor corresponding to the transformation given by Eq. 2.9 is

$$\mathbf{F} = \frac{\partial \mathbf{T}}{\partial \mathbf{r}}. \tag{2.14}$$

As the analytical expression of the transformation $\mathbf{T}$ from the reference frame to each frame (denoted as $\mathbf{T}_j$) is known, one can derive the analytical expressions of the spatial derivatives and compute $\mathbf{F}$. Then, the normal Lagrangian strain is obtained by projecting the Lagrangian tensor on the desired directions, i.e. the normal Lagrangian strain in the direction $\mathbf{v}$ is $\mathbf{v}^T\mathbf{E}\mathbf{v}$.

2.1.6 Validation

We perform two quantitative procedures to assess the accuracy of the method.

The first quantitative procedure compares the myocardial wall provided by the method with the one obtained by manual segmentation for the frames other than the reference frame. To evaluate the cardiac deformation recovery results, we compute the true positive (TP) rate, the false negative (FN) rate and the false positive (FP) rate for each frame. Let R_m represent the domain mapped by the method to the current frame and R_s the manually segmented LV wall in the current frame. Let V_s represent the volume of R_s, V_{ms} the volume

of the overlap of R_m and R_s, $\overline{V_{ms}}$ the volume of the part of R_m that is not in R_s, and $\widetilde{V_{ms}}$ the volume of the part of R_s that is not in R_m. Then, $TP\ rate = \frac{V_{ms}}{V_s}$, $FP\ rate = \frac{\overline{V_{ms}}}{V_s}$, and $FN\ rate = \frac{\widetilde{V_{ms}}}{V_s}$.

The second quantitative evaluation procedure compares the cardiac deformation recovery from the anatomical cine MRI obtained by the proposed method against the corresponding information from the tagged cine MRI. We developed a tool for interactive positioning of virtual tag planes in tagged MRI scans. The tag planes are modeled as splines that the user can position and deform by moving control points. This allows the user to fit the virtual tag planes to the tagged image as well as to compute tag plane intersections. Once the cardiac deformation is recovered from the anatomical cine MRI using the proposed method, it is applied to the virtual tag planes at ED and then compared to the interactively positioned tag planes in other frames. In each image slice we compute the distances between the corresponding intersections of orthogonal virtual tag lines (in-slice cross-sections of the virtual tag planes) generated interactively and by the model. This allows for in-plane (short-axis) deformation recovery validation. The out-of-plane (long-axis) deformation is not evaluated with this procedure since the tag planes, being perpendicular to the short-axis image slices, do not contain information about the out-of-plane motion.

2.2 Results

2.2.1 MR Protocols and Subjects

We carried out two studies to test the proposed method. In the first study, we acquired a 3D anatomical cine MRI scan together with a 3D tagged cine MRI scan of a healthy volunteer and then repeated the acquisitions four months later. The volunteer was a 27 year old male subject with no history of heart disease. The purpose of this study was twofold: to do a 4D validation of the deformation of the LV wall myocardium recovered from the anatomical scan against the corresponding information in the tagged scan, and to test the repeatability of the method. In the second study, we tested the method on 3D anatomical cine MRI scans of six human subjects: three patients with ventricular dyssynchrony and three healthy volunteers. The purpose of this study was to test if the method can distinguish normals from patients. The patients were recruited from the Cardiology Service at Emory

University Hospital (Atlanta, Georgia). The mean age of the patients was 54 years (one female and two males). They were compared to three age-matched normal subjects (one female and two males) with no history of cardiovascular disease. For the second study only one midventricular short axis tagged cine MRI slice was available for each of the six subjects.

For both studies, the anatomical MRI scans using steady-state free-precession (SSFP) short axis cine imaging covering the entire heart were acquired with a 1.5 T clinical MRI scanner (Intera, Philips Medical Systems, Best, The Netherlands). The scans had 12-17 contiguous short axis slices with 8-10 mm slice thickness (for the in-plane resolution see Tables 6 and 7) and a 20 cm field of view (FOV). A flip angle of 65°, TR of 3.4 ms and TE of 1.7 ms were used. Twenty phases for each slice were obtained during the cardiac cycle.

For the first study, the tagged scan had the same number of slices as the anatomical scan, which allowed for full 3D validation over time of the recovered deformation.

For the second study, one short axis tagged MR image slice was acquired for each of the six subjects. The tagging data was taken at a short axis slice positioned at 70% of the length of the LV from the apex (total LV length was measured from the apex to the mitral valve plane on the four-chamber long axis image). The tagging slice was not located at exactly the same position as one of the anatomical slices.

For all the subjects, the FOV for the tagged scan was the same as that of the cine scan. The tags were applied immediately after the detection of the R-wave from the EKG signal, and the first frame was acquired at a delay of 15 ms after the R-wave. Two orthogonal sets of parallel planar tags with about 9 mm plane separation were oriented orthogonal to the image planes. The temporal resolution for the tagged scan was 30 ms, whereas it ranged from 35-42 ms for the anatomical scan. The in-plane resolution for the tagged scan was 1.24 mm for all the subjects.

For all the subjects, for each acquired slice the scanner recorded the rigid body transformation from the scanner coordinate system to the slice. This allowed us to map all the slices to a common coordinate system, i.e. to spatially align the anatomical and tagged scans. Similarly, the scanner recorded the start time for each phase (frame) relative to the peak of the R wave, which allowed us to temporally align the anatomical and tagged scans. Since

the heart rate, i.e. the duration of the cardiac cycle, was not the same for the two scans, we used relative time (as a percentage of the cardiac cycle) for the temporal alignment.

2.2.2 Study: Repeatability

2.2.2.1 Surface Models, Displacement and Strain Fields

The deformation recovered from the first and the second (taken 4 months later) anatomical cine MRI scan of the healthy volunteer was very similar. For this reason we show the deformation recovery results for the second scan only and quantitatively compare the strains recovered from the two scans. In Section 3.2.2.2 we show validation results of the deformation recovered from both scans.

To display the model boundaries over time, we first constructed a 3D model of the LV endocardial surface, midsurface, and epicardial surface in the ED frame. Then, for all other frames, we deformed the three surface models by applying the recovered transformation to the model. Fig. 28 shows the contours of the three surface models for a midventricular and basal short axis slice over the cardiac cycle. Fig. 9 shows the contours of the three surface models for two orthogonal long axis slices over the cardiac cycle.

The motion of the LV wall is fully described by its displacement field over the cardiac cycle. Fig. 10 shows two short axis slices over the cardiac cycle with sampled displacement field projected to the slice.

Fig. 29 shows the Lagrangian radial, circumferential, and longitudinal strain fields over the cardiac cycle for a midventricular short axis slice. To further evaluate the strains, we sectored the domain in the reference configuration into the standard sectors, as defined in [39]. Then for each sector, for each strain type, we computed the average strain for that sector as a function of time over the cardiac cycle. We did this for both the first and the second anatomical cine MRI scan of the healthy volunteer. The time curves for the radial, circumferential, and longitudinal strains for all the sectors are shown in Figs. 30, 31, and 14, respectively. The peak values of the radial, circumferential, and longitudinal strains over the cardiac cycle for the two scans of the healthy volunteer are given in Table 6.

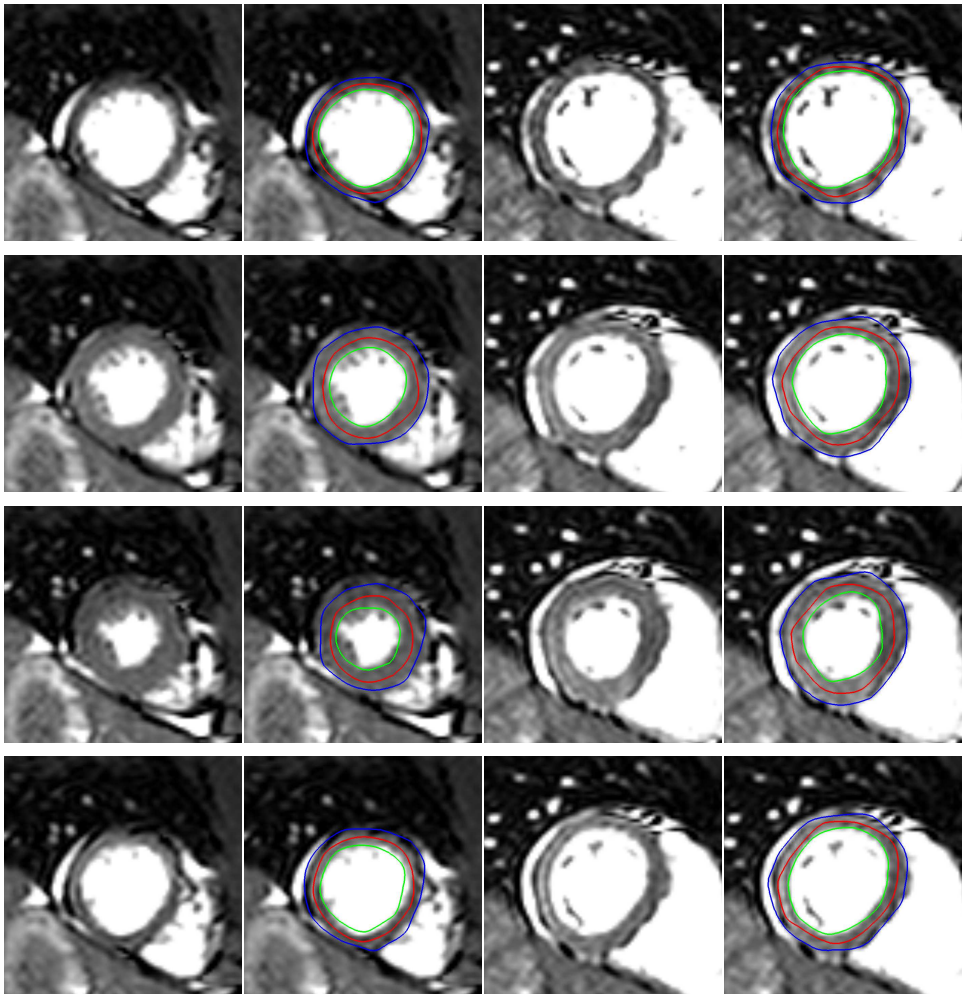

Figure 8. The recovered LV wall deformation for a normal subject over the cardiac cycle (first row: ED, third row: ES) is shown by means of the endocardial surface (green), midsurface (red), and epicardial surface (blue) contours: (a) a midventricular slice, (b) the same slice overlaid with the contours, (c) a basal slice, (d) the same slice overlaid with the contours. The synchronous thickening of the myocardium indicates normal cardiac function.

Table 1. In-plane resolution (IPR), number of model nodes (M), Peak radial strain (PRS), Peak circumferential strain (PCS) and Peak longitudinal strain (PLS) are given for the two scans of the healthy volunteer. PRS, PCS, and PLS were computed over the cardiac cycle.

Subject	IPR	M	PRS	PCS	PLS
	$[mm]$				
Scan 1	1.41	72	.38	-.14	-.11
Scan 2	1.44	79	.36	-.16	-.12

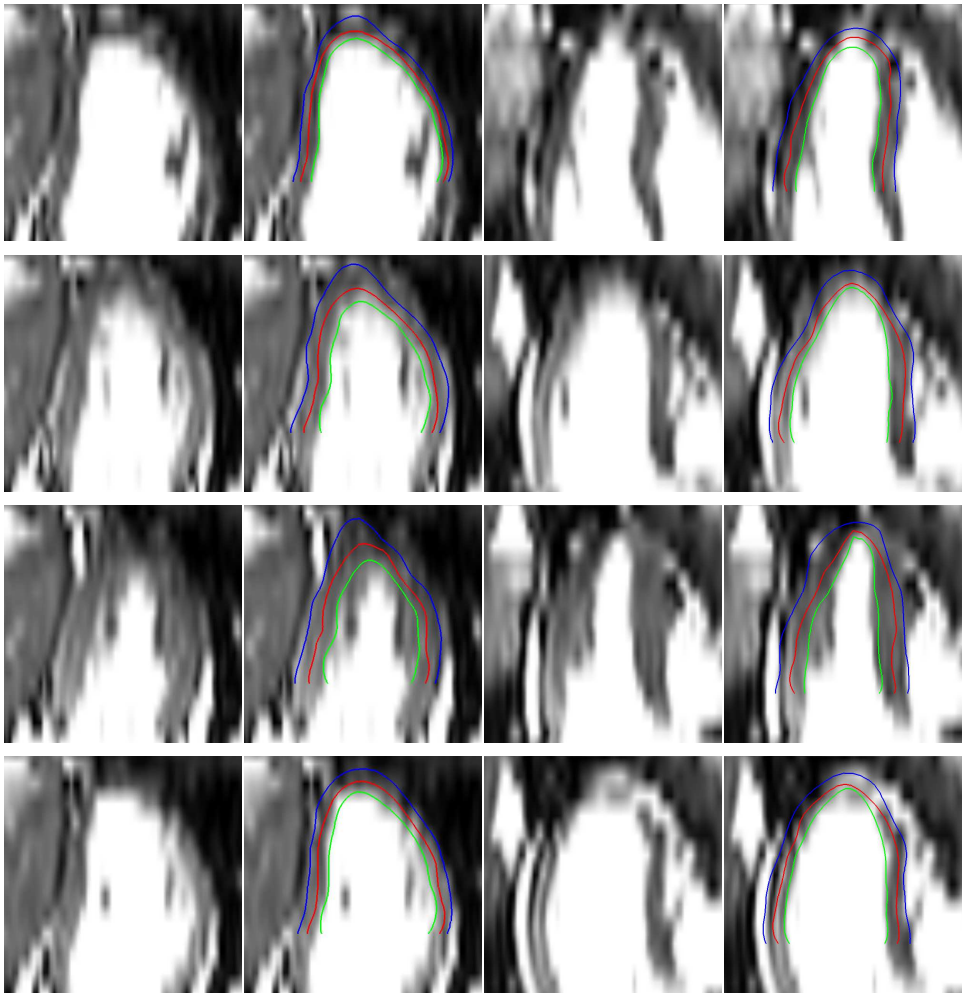

Figure 9. The recovered LV wall deformation for a normal subject over the cardiac cycle (first row: ED, third row: ES) is shown by means of the endocardial surface (green), midsurface (red), and epicardial surface (blue) contours for two orthogonal long axis slices: (a) the first long axis slice, (b) the same slice overlaid with the contours, (c) the second long axis slice, (d) the same slice overlaid with the contours. Note that the model thickened at ES, which is a consequence of the incompressibility.

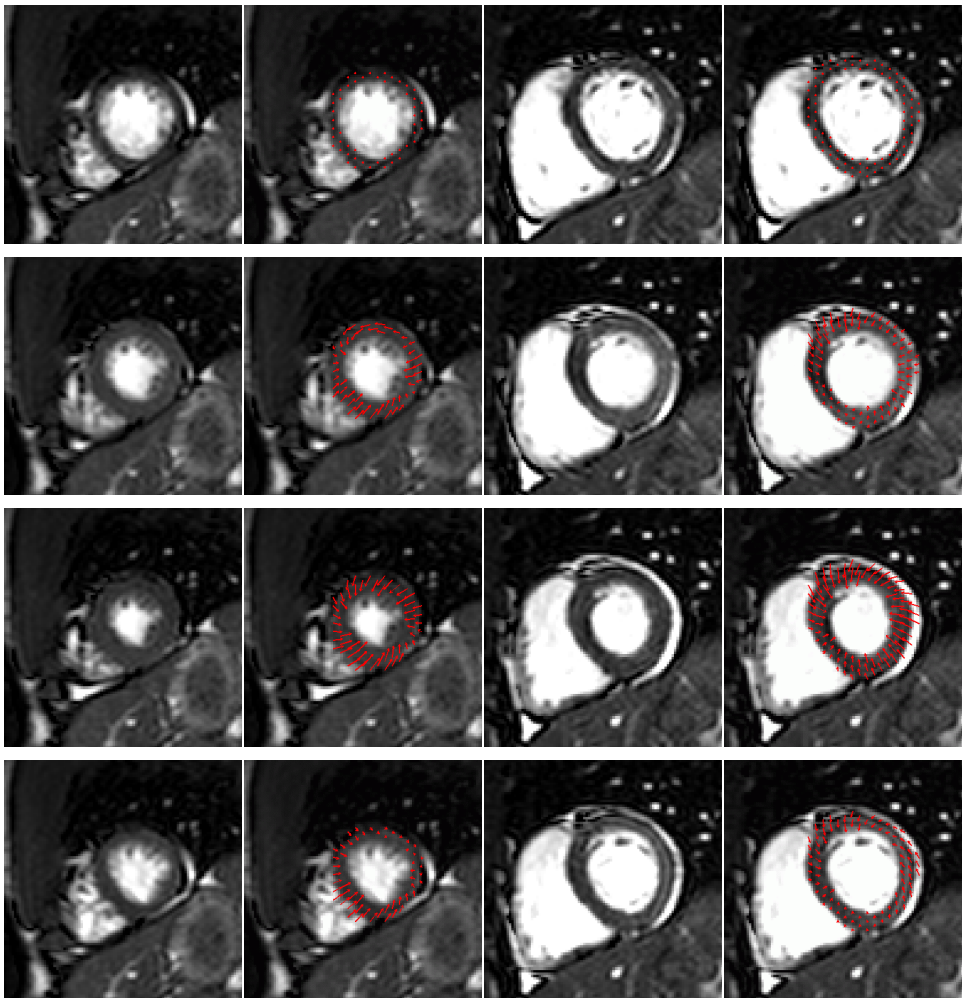

Figure 10. The recovered LV wall deformation for a normal subject over the cardiac cycle (first row: ED, third row: ES) is shown by means of the Lagrangian displacement field projected to the slice: (a) a midventricular slice, (b) the same slice overlaid with the projected displacements, (c) a basal slice, (d) the same slice overlaid with the projected displacements. Given that these are Lagrangian displacement vectors with ED being the reference frame, they originate at myocardial points at ED and they point to the corresponding locations in the current frame. This is why in the ED frame they are marked as dots (zero vectors). The displacements at ES show that the LV wall both contracted and twisted.

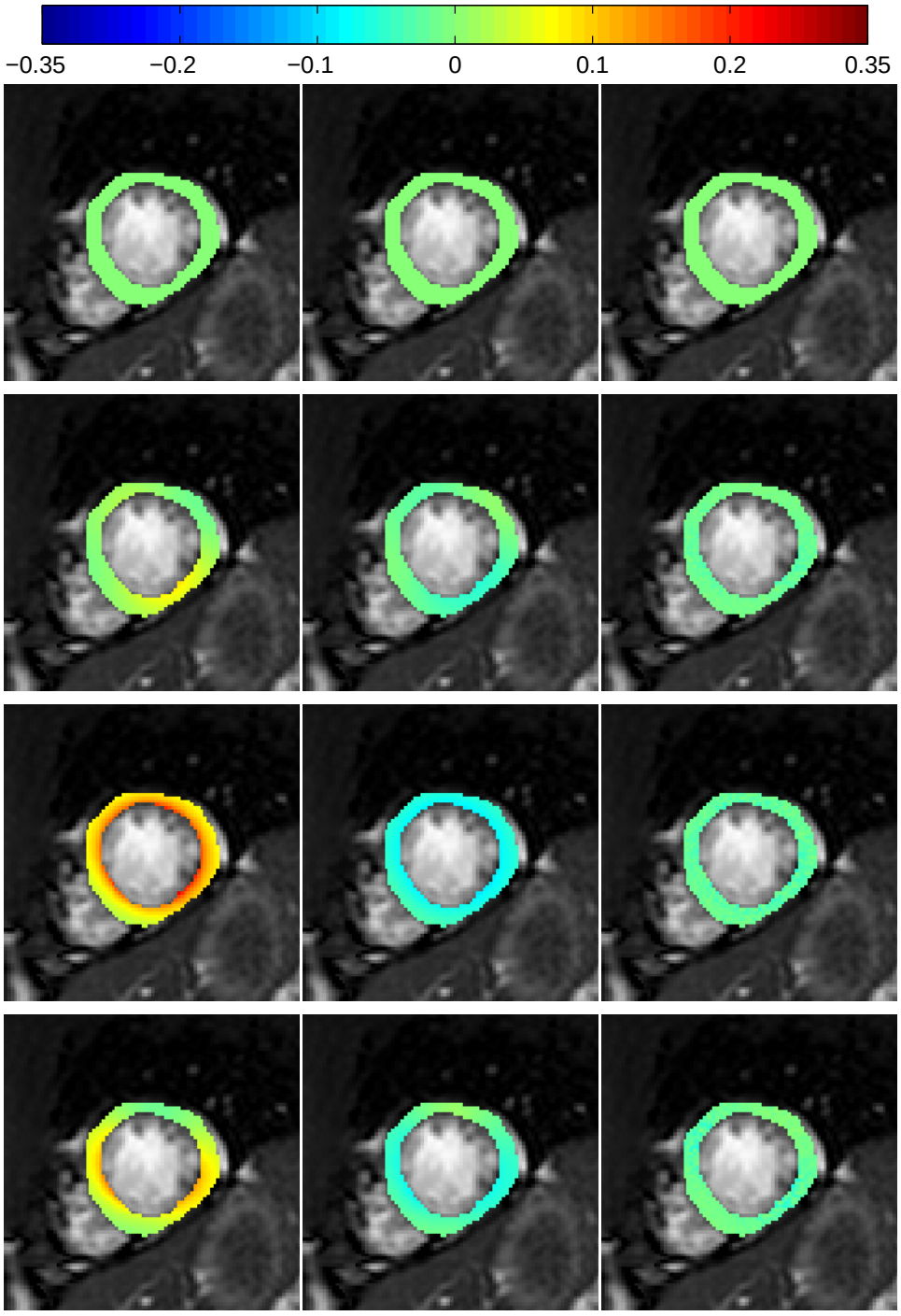

Figure 11. Color-coded (a) radial, (b) circumferential, and (c) longitudinal Lagrangian strains for a normal subject are shown in a midventricular slice over the cardiac cycle (first row: ED, third row: ES). Since the deformation is measured relative to ED, the strains in the ED frame are zero. The strains are shown over the ED frame image.

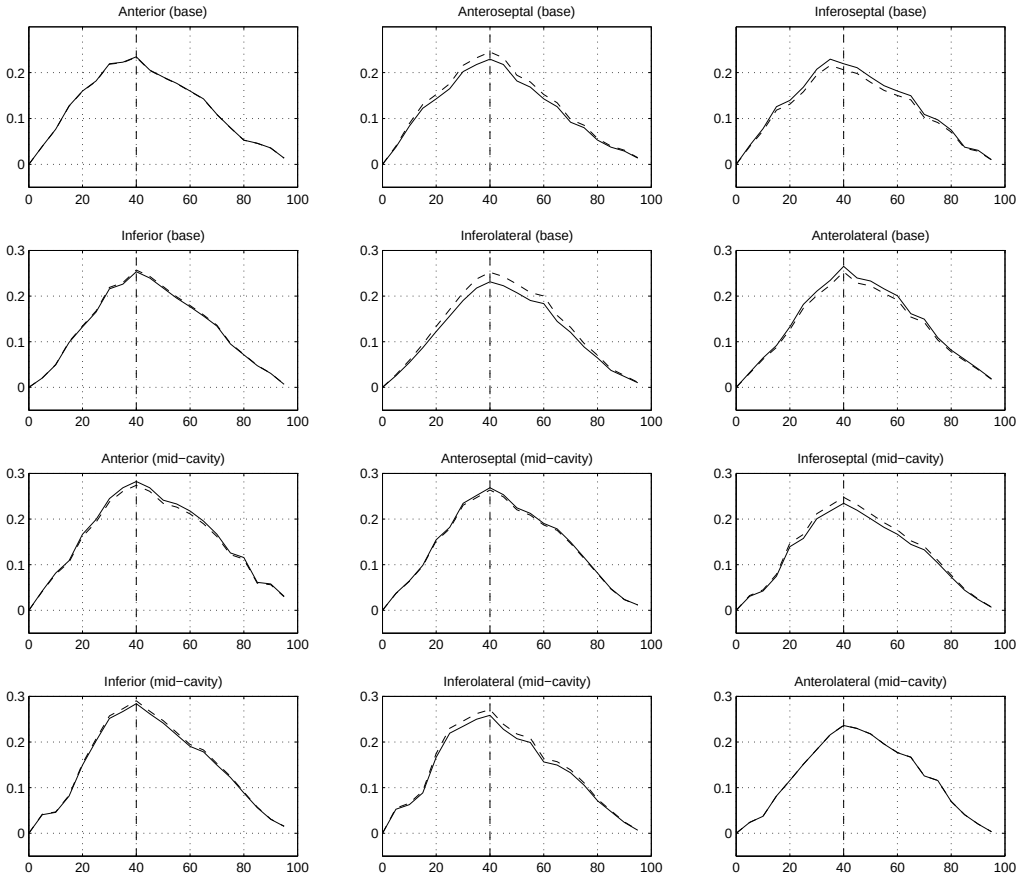

Figure 12. The radial strain for 12 standard midventricular and basal sectors as functions of time over the cardiac cycle for the first (solid curve) and the second (dashed curve) anatomical cine MRI scan of a healthy volunteer. The horizontal axis represents the time as a percentage of the cardiac cycle starting from ED. The vertical dashed line marks ES. Note the good agreement of the two curves for each sector.

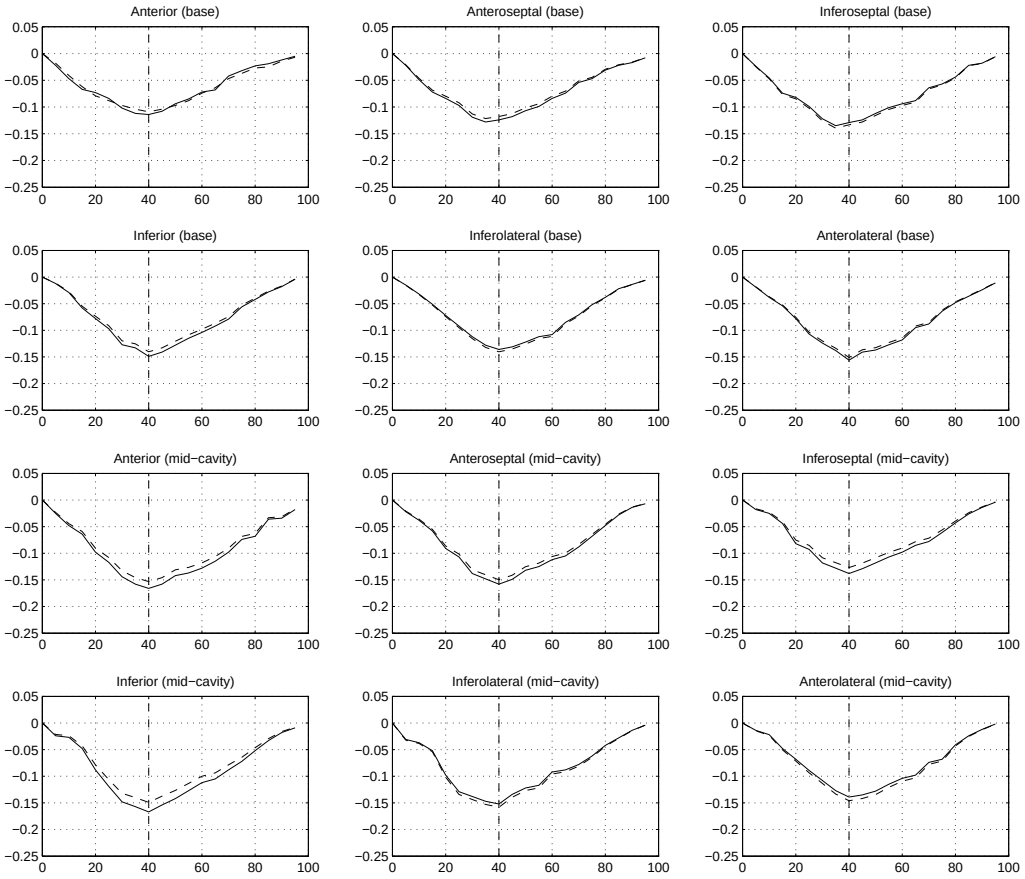

Figure 13. The circumferential strain for 12 standard midventricular and basal sectors as functions of time over the cardiac cycle for the first (solid curve) and the second (dashed curve) anatomical cine MRI scan of a healthy volunteer. The horizontal axis represents the time as a percentage of the cardiac cycle starting from ED. The vertical dashed line marks ES. Note the good agreement of the two curves for each sector.

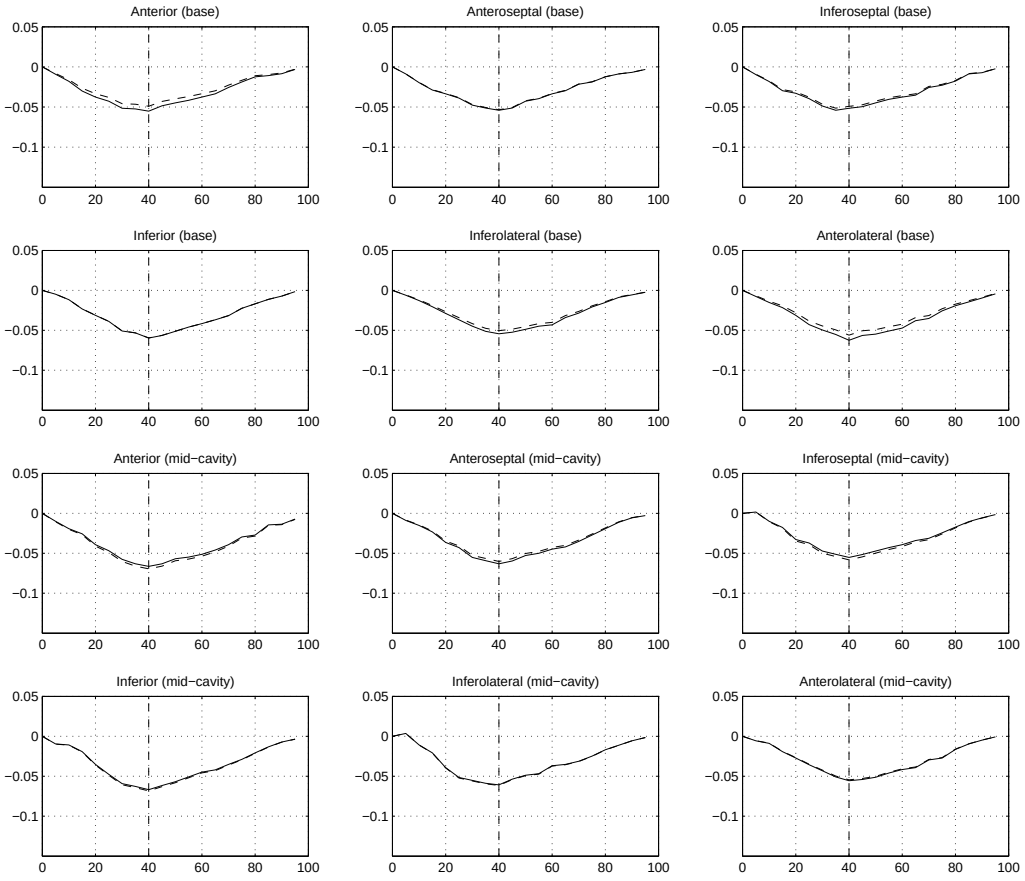

Figure 14. The longitudinal strain for 12 standard midventricular and basal sectors as functions of time over the cardiac cycle for the first (solid curve) and the second (dashed curve) anatomical cine MRI scan of a healthy volunteer. The horizontal axis represents the time as a percentage of the cardiac cycle starting from ED. The vertical dashed line marks ES. Note the good agreement of the two curves for each sector.

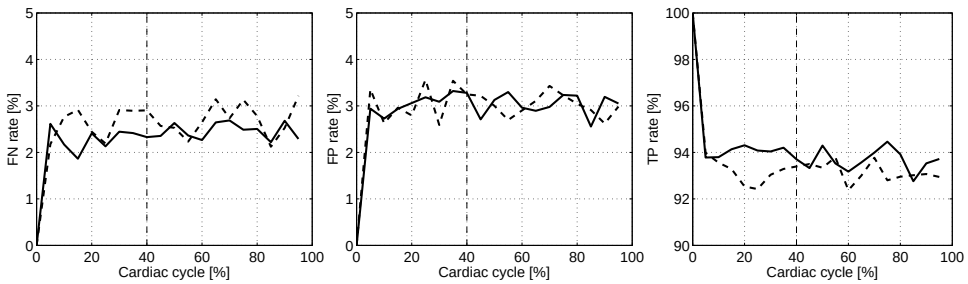

Figure 15. The false negative (FN), false positive (FP), and true positive (TP) rates for the volume agreement over the cardiac cycle between the manually segmented and model generated LV wall for the first (solid curves) and second (dashed curves) scan of the healthy volunteer. The horizontal axis represents the time as a percentage of the cardiac cycle starting from ED. The vertical dashed line marks ES. Since the deformation is measured relative to ED, the FN and FP rates are 0% and TP rate is 100% at ED.

2.2.2.2 Validation

To quantitatively evaluate the LV wall deformation recovered from the anatomical cine MRI scan we validated it against the manually segmented LV wall and against the manually positioned tag lines in the corresponding tagged cine MRI scans, both over the entire cardiac cycle.

For the first validation procedure, we manually segmented the LV wall in all the frames of the 3D anatomical cine MRI. Then we applied the recovered deformation to the LV wall segmented in the ED frame and mapped it to all other frames (Fig. 18). Finally, we quantified the agreement between the manual and model generated LV wall segmentation by means of true positive, false negative and false positive rates. Fig. 32 shows the three rates over the cardiac cycle for the first and second scan of the healthy volunteer.

For the second validation procedure, we manually positioned tag planes in the ED frame of the 3D tagged cine MRI. Then we applied the deformation recovered from the anatomical scan to the tag planes positioned in the ED frame of the tagged scan and mapped them to all other frames of the tagged scan. Fig. 34 shows the virtual tag lines for a midventricular slice for the second scan of the healthy volunteer. Finally, we measured the distances between the intersections of real tag lines and the corresponding intersections of virtual tag lines for all the frames for both the first and the second scan of the healthy volunteer. The results are given in Fig. 33.

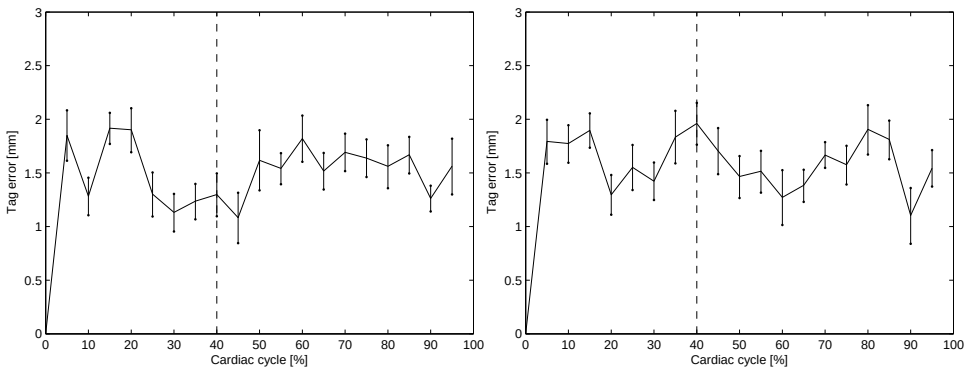

(a) (b)

Figure 16. The mean and standard deviation of the manually measured distances between the intersections of real tag lines and the corresponding intersections of virtual tag lines over the cardiac cycle for (a) the first and (b) the second scan of the healthy volunteer. The horizontal axis represents the time as a percentage of the cardiac cycle starting from ED. The vertical dashed line marks ES. Since the deformation is measured relative to ED, the distances are zero in the ED frame.

2.2.3 Study: Comparison of Normals and Patients

2.2.3.1 Displacement and Strain Fields

We recovered the LV wall deformation for three normal subjects and three patients. Fig. 19 shows displacements over the cardiac cycle projected to a short axis slice for a normal subject and a patient. Fig. 23 shows Lagrangian radial and circumferential strains in a short axis slice over the cardiac cycle for a normal subject and a patient. To further compare the strains of the normal subjects and patients, we sectored the domain in the reference configuration into the standard sectors, as defined in [39]. Then for each sector, for each strain type, we computed the average strain for that sector as a function of time over the cardiac cycle. We did this for the three normal subjects and three patients. The time curves for the radial, circumferential, and longitudinal strains for all the sectors are shown in Figs. 35, 36, and 22, respectively.

2.2.3.2 Validation

To quantitatively evaluate the LV wall deformation recovered from the anatomical cine MRI scan for the three normal subjects and three patients we validated it against the manually segmented LV wall and against the manually positioned tag lines in the corresponding tagged cine MRI scan.

For the first validation procedure, we manually segmented the LV wall in the ED and

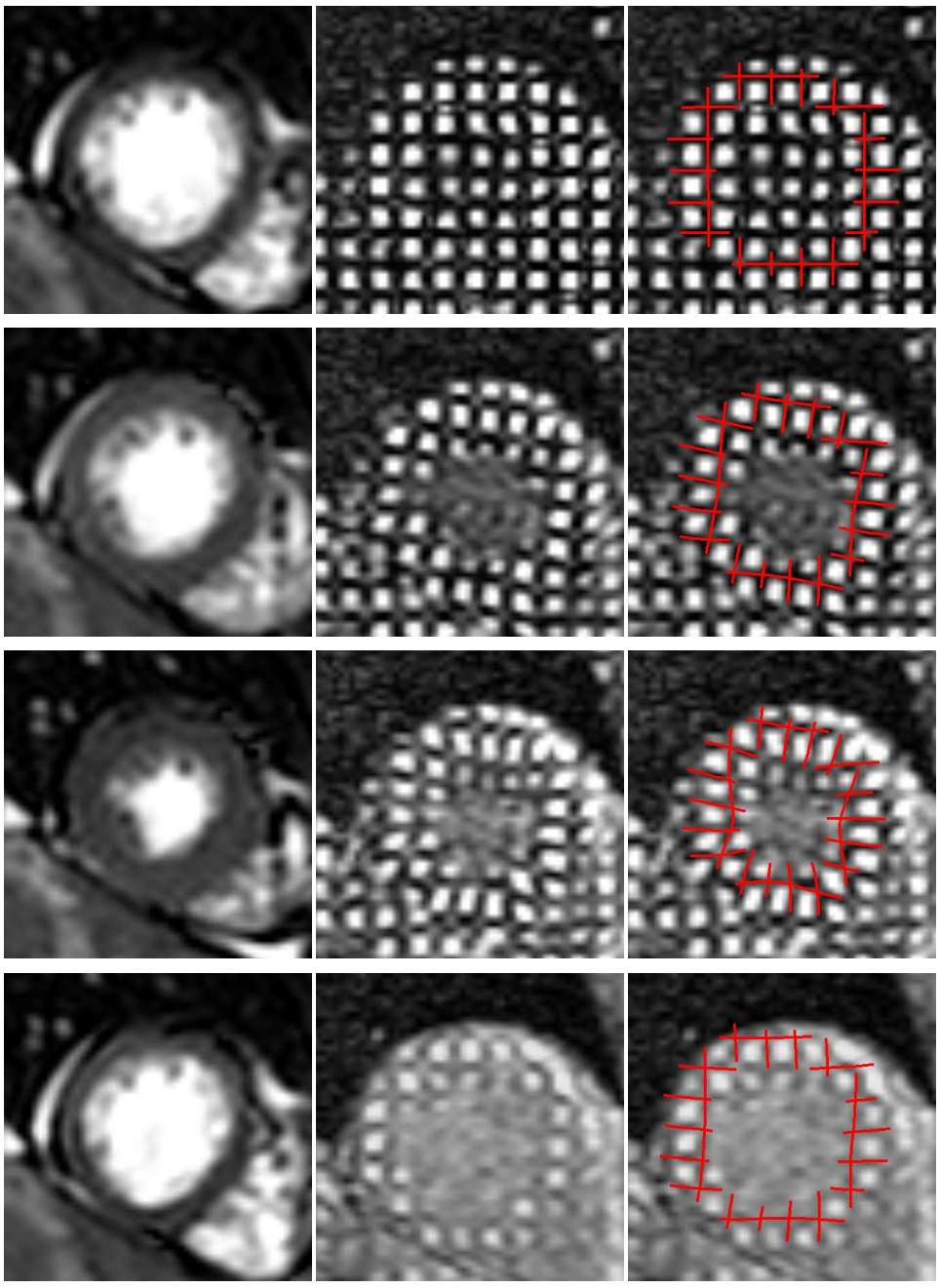

(a) (b) (c)

Figure 17. A midventricular short axis slice from the anatomical cine MRI scan is shown in (a) over the cardiac cycle (first row: ED, third row: ES). The corresponding slice in the tagged cine MRI scan is shown in (b). The slice from (b) is overlaid with virtual tag lines in (c). The virtual tag lines were generated by applying the deformation recovered from the anatomical scan to the manually positioned tag planes at ED. The images are from the second scan of the healthy volunteer.

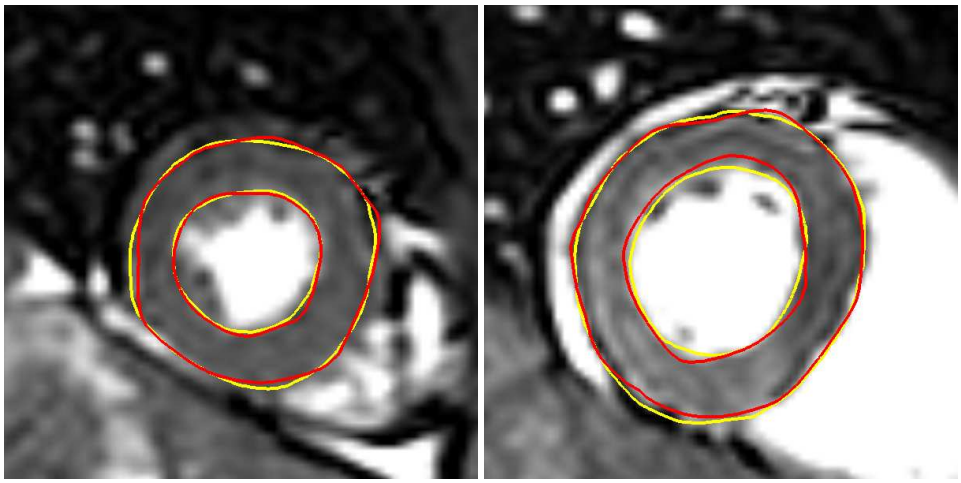

(a) (b)

Figure 18. LV wall boundaries corresponding to the manual segmentation (yellow) and the deformable model (red) at ES for a healthy volunteer in (a) midventricular and (b) basal short axis slice.

ES frames of the 3D anatomical cine MRI. Then we applied the recovered deformation to the LV wall segmented in the ED frame and mapped it the ES frame. Finally, we quantified the agreement between the manual and model generated LV wall segmentation in the ES frame by means of true positive, false negative and false positive rates. Table 7 shows the three rates for the three normal subjects and three patients.

For the second validation procedure, we manually positioned tag planes in the ED frame of the 3D tagged cine MRI. Then we applied the recovered deformation to the tag planes positioned in the ED frame and mapped them to all other frames. Fig. 24 shows the virtual tag lines for a short axis slice for a normal subject and a patient. Finally, we measured the distances between the intersections of real tag lines and the corresponding intersections of virtual tag lines for the ES frame for the three normal subjects and three patients. The results are given in Table 7.

2.3 Discussion

2.3.1 Deformable Model

The proposed deformable model has the following properties: it is volumetric, its representation is compatible with the anatomy of the left ventricle, it behaves uniformly in all the

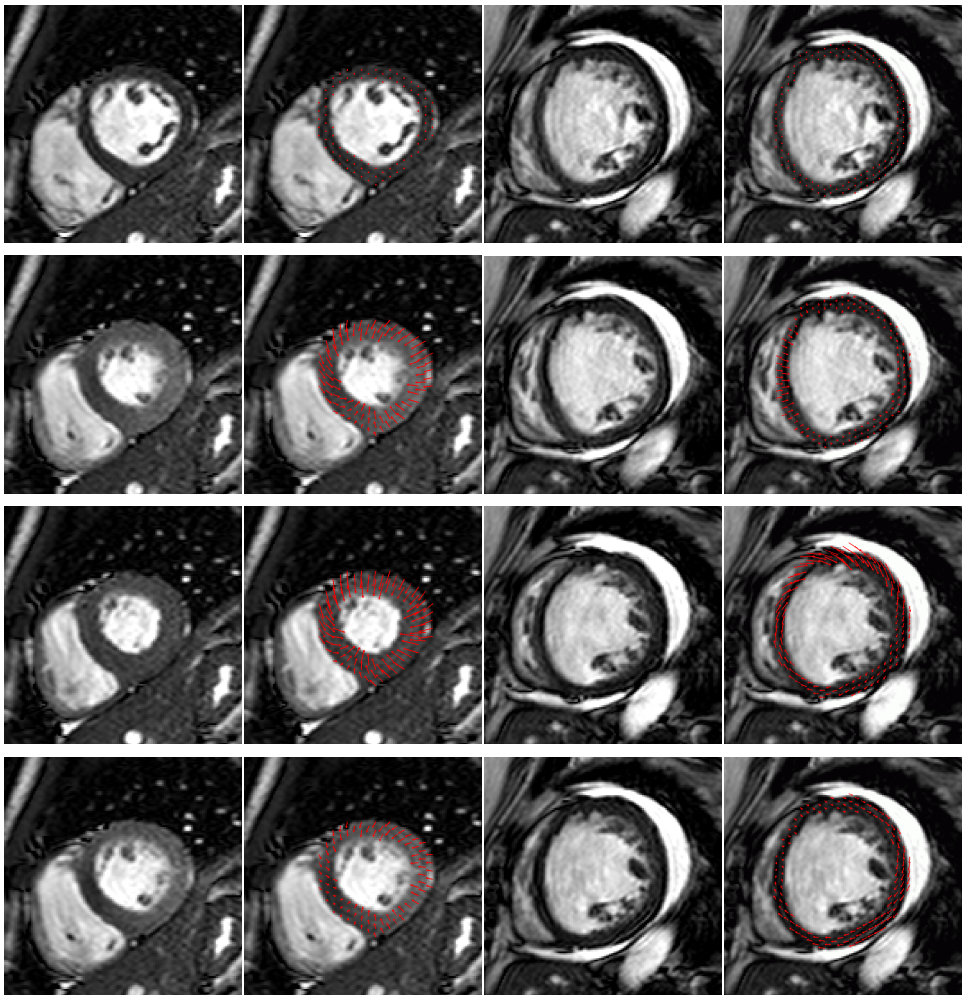

(a) (b) (c) (d)

Figure 19. A short axis slice for (a) a normal subject and (c) a patient are shown over the cardiac cycle (first row: ED, third row: ES). The same slices overlaid with Lagrangian displacements projected to the slice are shown in (b) and (d), respectively. Since the LV wall deformation was recovered relative to ED, the displacement vectors are zero (marked as dots) at ED. The displacements of the normal subject at ES show that the LV wall both contracted radially and twisted circumferentially. The displacements of the patient at ES showed reduced radial contraction. The reduced displacement is an indication of reduced cardiac function and low ejection fraction. The presence of asynchronous motion of the LV wall for the patient can be seen at mid-systole (second row), end-systole (third row) and mid-diastole (fourth row): each of these frames has regions of the LV wall with almost zero displacements while the other regions were moving. In the normal subject all the regions of the wall were moving synchronously in each frame.

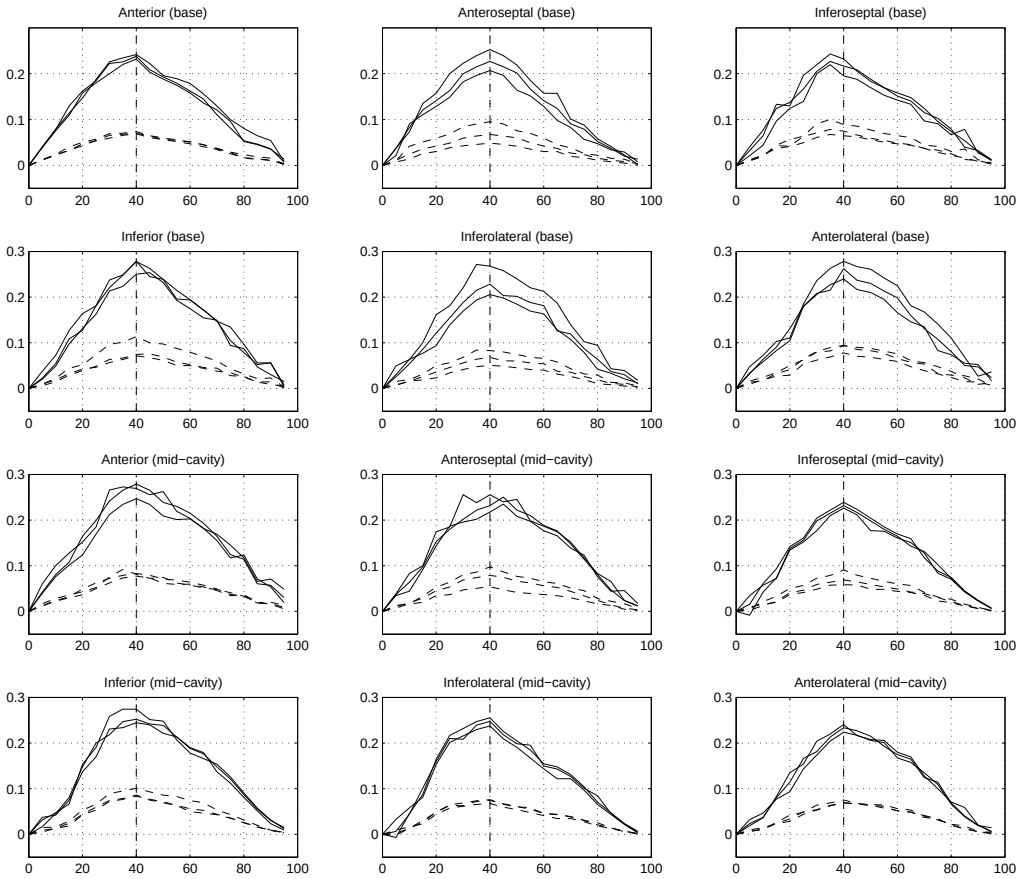

Figure 20. The radial strain for 12 standard midventricular and basal sectors as functions of time over the cardiac cycle for the three normal subjects (solid curves) and the three patients (dashed curves). The horizontal axis represents the time as a percentage of the cardiac cycle starting from ED. The vertical dashed line marks ES. Note the similarity of the time curves for the normals, the similarity of the time curves for the patients, and a clear difference between time curves of the normals and of the patients.

,

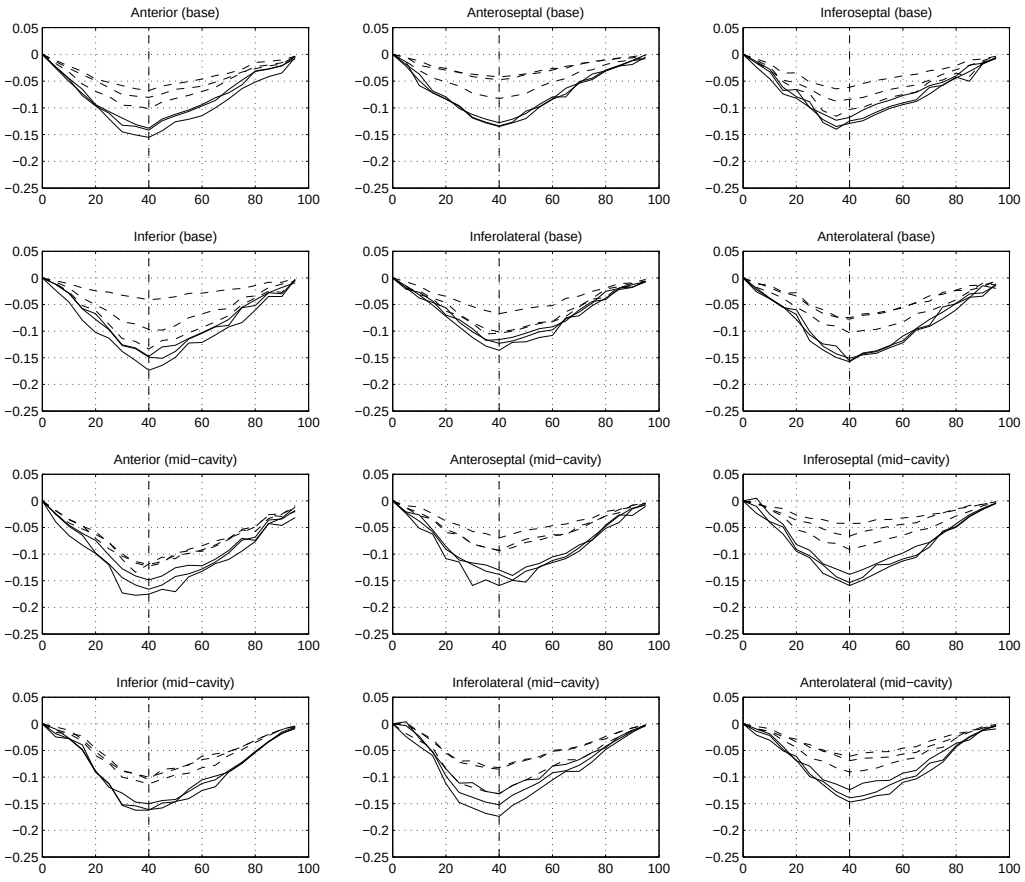

Figure 21. The circumferential strain for 12 standard midventricular and basal sectors as functions of time over the cardiac cycle for the three normal subjects (solid curves) and the three patients (dashed curves). The horizontal axis represents the time as a percentage of the cardiac cycle starting from ED. The vertical dashed line marks ES. Note the similarity of the time curves for the normals. For most of the sectors the patients had a weaker circumferential strain than the normals.

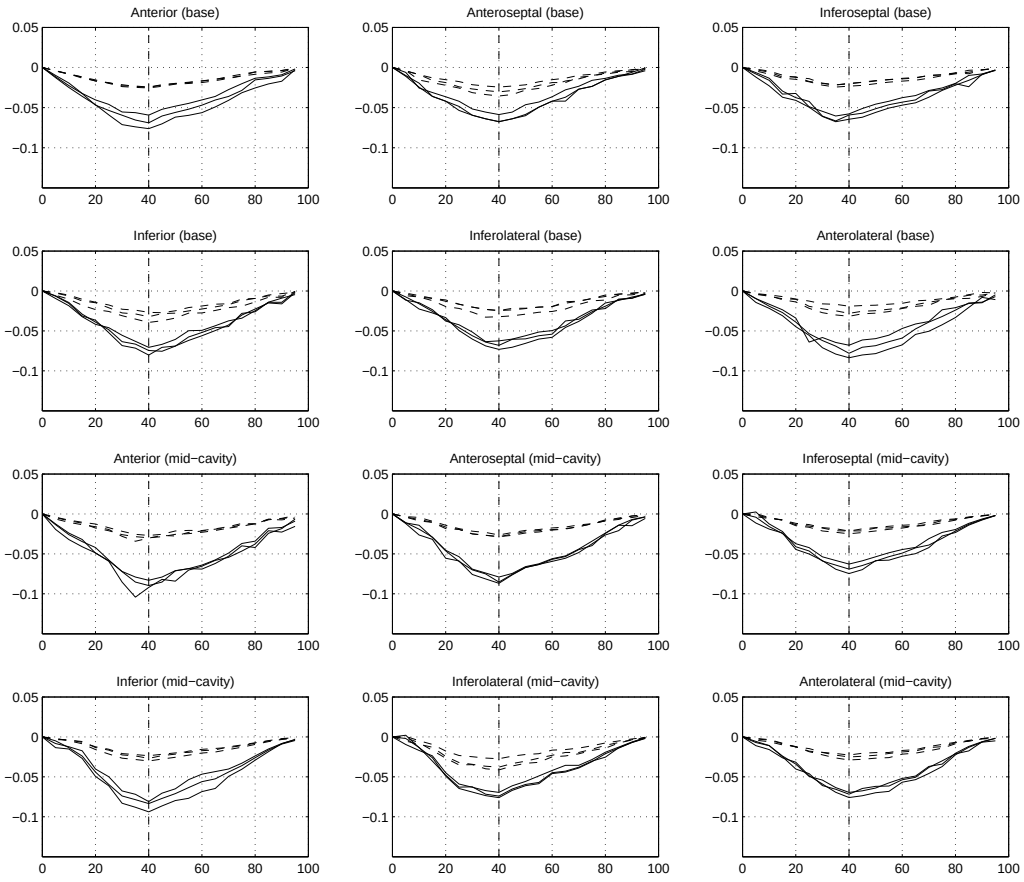

Figure 22. The longitudinal strain for 12 standard midventricular and basal sectors as functions of time over the cardiac cycle for the three normal subjects (solid curves) and the three patients (dashed curves). The horizontal axis represents the time as a percentage of the cardiac cycle starting from ED. The vertical dashed line marks ES. Note the similarity of the time curves for the normals, the similarity of the time curves for the patients, and a clear difference between time curves of the normals and of the patients.

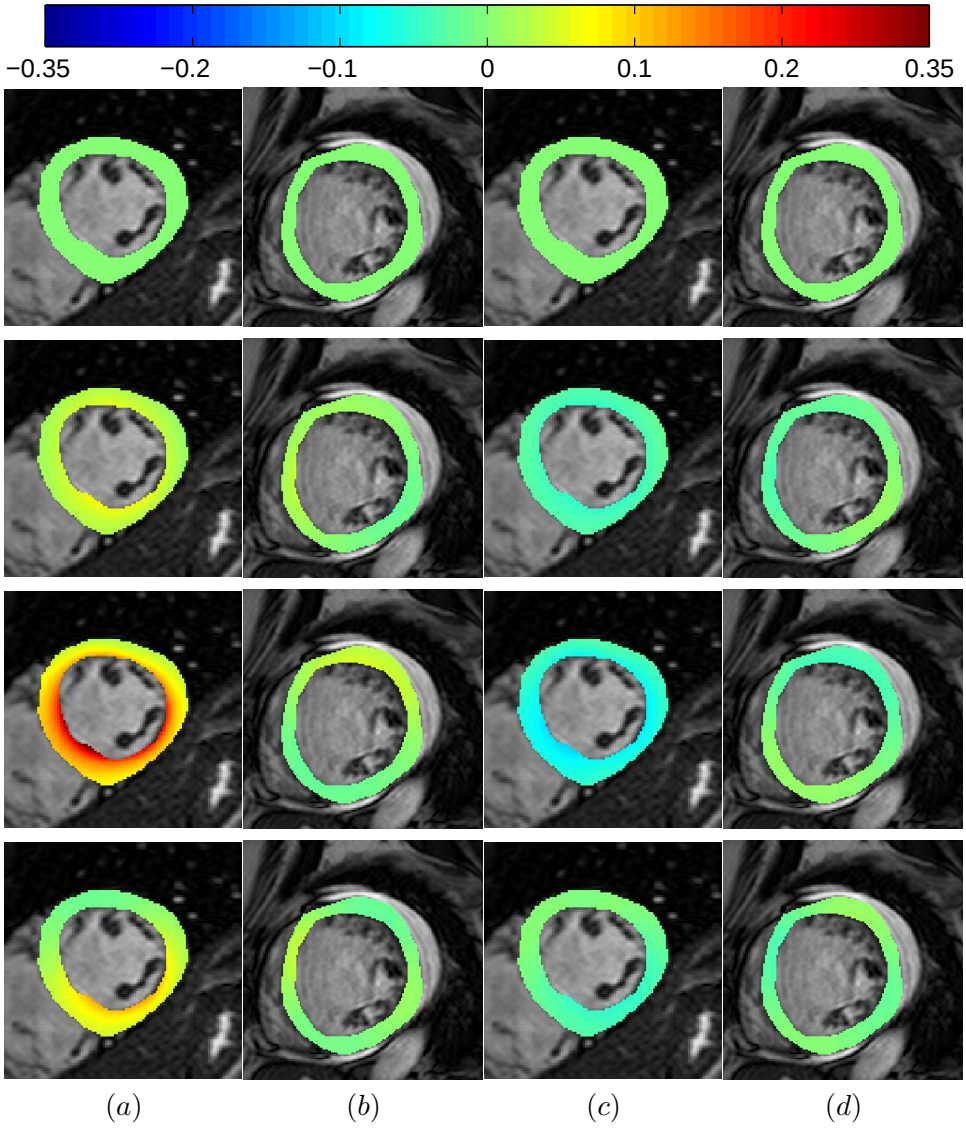

Figure 23. Color-coded Lagrangian strains for a normal subject and a patient are shown in a short axis slice over the cardiac cycle (first row: ED, third row: ES): (a) radial strain for the normal subject, (b) radial strain for the patient, (c) circumferential strain for the normal subject, (d) circumferential strain for the patient. Since the deformation is measured relative to ED, the strains in the ED frame are zero. The strains are shown over the ED frame image. The lower strain values in the patient indicate reduced cardiac contractility. In addition, the regional heterogeneity strain distribution in the patient images indicates either dyssynchrony or ischemic myocardium.

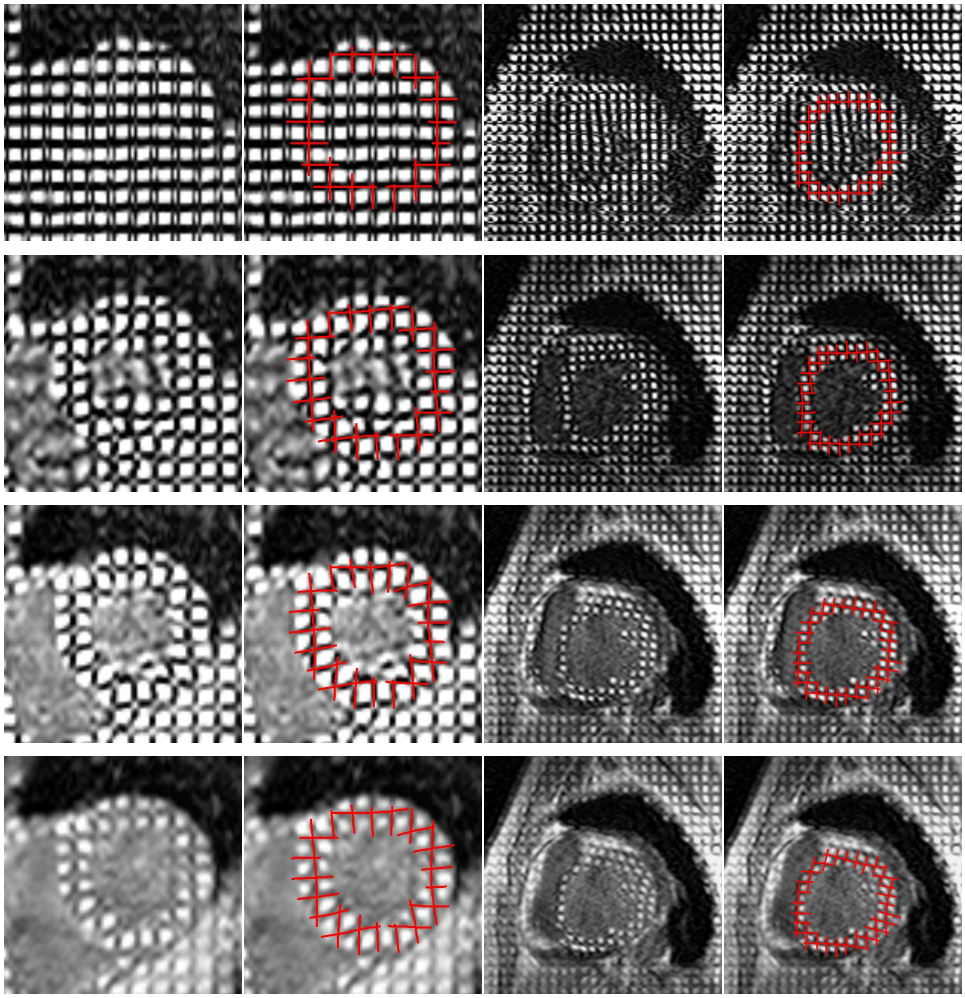

Figure 24. A short axis slice from the tagged cine MRI scan is shown over the cardiac cycle (first row: ED, third row: ES) for (a) a normal subject and for (c) a patient. The same slices overlaid with virtual tag lines are shown in (b) and (d), respectively. The virtual tag lines were generated by applying the deformation recovered from the anatomical scan to the manually positioned tag planes at ED.

Table 2. In-plane resolution (IPR), number of model nodes (M), True positive rate (TPr), False positive rate (FPr), False Negative rate (FNr), the average (± std) distance between manually and automatically obtained intersections of perpendicular tag planes (Tag error), Peak radial strain (PRS), Peak circumferential strain (PCS) and Peak longitudinal strain (PLS) are given for the three normal subjects and thee patients. TP rate, FP rate, FN rate, and Tag error were computed for the ES frame whereas PRS, PCS, and PLS were computed over the entire cardiac cycle.

Subject	IPR	M	TPr	FPr	FNr	Tag error		PRS	PCS	PLS
	$[mm]$		[%]	[%]	[%]	$[mm]$	$[pixel]$			
Normal 1	1.24	55	92.4	3.2	2.8	1.5±.2	1.1±.1	.34	-.18	-.13
Normal 2	1.36	62	91.8	2.7	3.1	1.6±.3	1.2±.2	.32	-.17	-.12
Normal 3	1.41	72	93.3	3.4	2.9	1.7±.3	1.1±.1	.38	-.14	-.11
Patient 1	1.52	58	91.7	2.8	2.6	1.6±.3	1.1±.2	.14	-.07	-.06
Patient 2	1.35	56	92.7	3.3	3.5	1.7±.3	1.0±.1	.12	-.06	-.08
Patient 3	1.56	52	93.2	3.7	3.4	1.8±.2	1.1±.2	.12	-.07	-.07

regions, its displacement field is C_1 continuous, it is incompressible, it allows for no transmural bending, and with the exception of no transmural bending, it is capable of generating realistic cardiac deformation patterns and normal strains.

This is a volumetric model (as opposed to a surface model), since it maps a 3D domain (as opposed to a surface) in the reference configuration to the current configuration. The domain is defined by segmenting the LV wall at ED (Fig. 1).

The model uses a midsurface curvilinear coordinate system. The model midsurface is obtained by interpolating the nodes approximately uniformly placed over the LV wall midsurface (Fig. 2). In the midsurface curvilinear coordinate system, the position of a point in the domain is defined by the closest point on the midsurface and the distance from the midsurface (Fig. 3). This representation provides a realistic geometry of the model (Fig. 4a), natural definition of the transmural direction (γ direction, i.e. the direction perpendicular to the midsurface) and uniform behavior of the model. All the regions, apical, midventricular, and basal, are treated equally by the model, unlike models based on the cylindrical, spherical and prolate spheroidal coordinate systems that have points ("poles") that require special treatment. At the poles some of the displacement derivatives are not defined, which in turn causes the strain tensor not to be defined. As a consequence, the deformation recovered at and in vicinity of the poles is not correct. When such coordinate systems are used, typically one pole is at the apex, which prevents one to model the apical

region [9]. The proposed model does not have this limitation since it has no poles or other special points or directions.

The midsurface is obtained by interpolating the nodes using pseudo thin plate splines (Appendix A). Although other interpolation schemes could be used, this one provides a smooth interpolation of the midsurface nodes and it does not have poles. The continuity order of the midsurface representation depends on function ψ. For the one given by Eq. A.3 and shown in Fig. 54, the midsurface is C_3 continuous at the nodes and C_∞ continuous in between. As a consequence, the transformation (Eq. 2.9) and the corresponding displacement field are C_1 continuous at the nodes and C_∞ continuous inbetween, since their computation involves the midsurface curvatures (present in Eq. 2.8), which depend on second derivatives of the midsurface. It should be noted that C_1 is the minimal order of continuity of the displacement field for the strain tensor to exist.

Given that incompressibility is a physical property of the myocardium (Section 1.4), deformable models that are used for cardiac deformation recovery should either be exactly incompressible, as the proposed model, or their Jacobian should be monitored not to deviate from 1 by more than a few percents. The Jacobian of a deformable model, if not monitored, can easily significantly deviate from 1, causing physically incorrect deformations. The importance of Jacobian follows from the fact that it is the determinant of the deformation gradient tensor (Eq. 2.14), which is used to compute strain (Eq. 2.13). This means that an incorrect Jacobian implies an incorrect deformation gradient tensor, which in turn implies incorrect strain.

In general, one can estimate normal strain more accurately than shear strain. The reason for this is that to estimate normal strain one needs to know the deformation in one direction, whereas to estimate shear strain one needs to know the deformation in two directions. For this reason it is not surprising that researchers analyzing cardiac motion from images have almost exclusively reported normal strains and not shear strains [7, 14, 9, 40, 13, 11, 30, 29, 41]. This is in line with the findings of Ubbink *et al.* [37] who used tagged cine MRI to obtain reliable estimates of normal strain and concluded that shear strain cannot be reliably estimated. Given this, given that shear strain is relatively small compared to normal strain [37], given that it takes both positive and negative values [37, 42], and given that we used

anatomical cine MRI that contains less information about cardiac motion than tagged cine MRI, we assumed a deformable model with no transmural bending. While no transmural bending results in small (less than 1 %) transmural shear strain for typical deformations of the LV wall, it does not impose restrictions on the normal (radial, circumferential, and longitudinal) strains. Using a deformable model that allows for transmural bending, e.g. a model based on B-Splines [10, 11, 43], to recover cardiac deformation from anatomical or even tagged cine MRI does not mean that the computed shear strain is reliable since the images contain little information about it. In order for a deformable model to reliably recover shear strain, it would need to have additional prior knowledge built in, e.g. the orientation of myofibers.

As a consequence of the incompressibility and no transmural bending, the deformation of the model is completely defined by the deformation of the model midsurface, which results in a fewer degrees of freedom. The model is a compromise between complexity and the information available in the anatomical cine MR images, i.e. it is a simple model that can extract most of the information about cardiac motion present in the images. A more complex model is not likely to provide more information about the cardiac motion unless additional prior knowledge was used. Despite its simplicity and the limitation of the no transmural bending assumption, the model is capable of generating realistic deformation patterns and normal strains. Fig. 25f shows a deformation pattern typical for ES, which is a combination of radial contraction, circumferential twisting, and longitudinal shortening. Normals strains are shown in Sec. 3.2 and discussed in Sec. 3.3.2.

2.3.2 Deformation Recovery

For each subject, we manually segmented the LV wall at ED, after which the rest of the method was fully automated: the LV center was computed as the barycenter of the segmented LV wall, the midsurface nodes were initialized at ED (Sec. 2.1.2), their positions determined in the rest of the frames (Sec. 2.1.4), and displacements (Sec. 2.1.3) and strains (Sec. 2.1.5) computed everywhere within the LV wall over the cardiac cycle. The manual segmentation of the LV wall at ED typically took 40-60 minutes. This step could be

automated, making the entire method completely automated. In either case, the segmentation needs to be careful to avoid interstices and trabeculation of the endocardial surface of the myocardium. These structures have many small pools of blood, and as the blood comes in and out of the pools, their volume changes over the cardiac cycle, which violates the incompressibility assumption. For this reason, inclusion of endocardial interstices and trabeculation in the segmented domain increases the deformation recovery error.

To recover the LV wall deformation, we searched for the model node locations that maximized normalized mutual information. One could possibly use some other image similarity measure and augment the method by using spatial and/or temporal smoothing. We implemented the method in Matlab, and on average it took about 5 hours to recover the 3D LV wall deformation over the entire cardiac cycle. This included both forward and backward recoveries that were done independently. The run time can be reduced by implementing the method in a faster language, e.g. C/C++ and by parallelizing the code. The slowest step is to interpolate I_j in order to compute $I_j(\mathbf{T}_j)$ in Eq. 2.11. This step is highly parallelizable, which would lead to a significant execution speed up.

2.3.3 Results

The method accurately tracked the endocardial and epicardial boundaries in the short axis views (Fig. 28) whereas the long axis views (Fig. 9) reveal that a part of the longitudinal motion was not recovered. This is a consequence of the strong voxel anisotropy: the in-plane (short-axis) resolution (1.44 mm) was more than 5 times smaller than the out-of-plane (long-axis) resolution (8 mm). All the subjects in both studies had a similar voxel anisotropy. The recovered short axis wall thickening in conjunction with incompressibility help with the deformation recovery in the long axis direction. However, even small errors in short axis wall thickening can lead to large errors in longitudinal shortening. For this reason, the long-axis behavior is dominated by the strong voxel anisotropy, i.e. the thickening/incompressibility mechanism, although helpful, is not strong enough (due to the high sensitivity to thickening error) to overcome the problem of the 5 times smaller resolution in the long axis direction. The recovered displacement field of the same subject (Fig. 10) shows

that the myocardium both synchronously contracted and twisted, which is a typical deformation pattern for normal subjects. The radial, circumferential, and longitudinal strain maps (Fig. 29) and time curves (Figs. 30, 31, 14) show strain patterns typical for normal subjects: radial strain increases from ED to ES and then comes back to zero at the end of the cycle, while circumferential and longitudinal strains decrease from ED to ES and come back to zero at the end of the cycle. Strain curves of normal subjects with similar shapes and peak values were reported by researchers using tagged MRI [37, 9, 13], DENSE MRI [7, 40] and echocardiography [41]. The longitudinal strain has somewhat lower peak values as compared to those reported in the literature. This is due to the underestimated longitudinal displacements, which is a consequence of the voxel anisotropy in the longitudinal direction. To validate the method, we applied the recovered deformation to the segmented LV wall at ED, mapped it to all other frames, and compared it to the corresponding manual segmentation. Fig. 18 shows the boundaries of the model and the manual segmentation in two short axis slices whereas Fig. 32 shows the false negative, false positive, and true positive rates of the agreement between the model and manual segmentation over the cardiac cycle for the two scans of the first study. One can see that the false positive and negative rates were about 3 % and the true positive rate was about 93 % everywhere in the cycle. These numbers reflect both the deformation recovery error and the inaccuracy of the manual segmentation. To further validate the method, we applied the recovered deformation to the virtual tag planes manually positioned in ED and compared them to the tag planes in all other frames. This is illustrated in Fig. 34 for a midventricular short axis slice over the cardiac cycle. The errors (distances) between the corresponding intersections of real and virtual tag lines over the cardiac cycle for the two scans are shown in Fig. 33. One can see that the errors are mainly between 1 and 2 mm. Given that the in-plane resolution of the two scans is over 1.4 mm, it follows that the method was able recover the deformation from anatomical MRI scans with an error of up to 1.5 pixels in short axis planes relative to the corresponding tagged MRI scans. Figs. 28, 9, 10, 29, 18 and 34 show deformation recovery results for the second scan of the first study. The corresponding results obtained for the first scan of the first study are not shown since they are very similar. A quantitative comparison of the deformation recovery from the two scans is shown in Figs. 30, 31, and

14 for strains, in Fig. 32 for the volume rates and in Fig. 33 for the tag errors, all over the entire cardiac cycle. All the measures (strain values, volume rates, and tag errors) are very similar between the two scans and the difference is within the accuracy of the method. This suggests that the method has the quality of repeatability, i.e. when applied to repeated scans of the same subject it produces similar deformation recovery results.

The displacements of a normal subject and a patient in Fig. 19 show clearly different deformation patterns: the patient lacked radial contraction and synchronous motion, which are characteristics of a normal cardiac motion and which were present in the deformation of the normal subject. This implied a low ejection fraction for the patient. The reduced cardiac function of patients can also be seen in the strain maps (Fig. 23) and in the strain time curves (Figs. 35, 36, 22). The strains of the patients had consistently lower peak values than the corresponding strains of the normal subjects (Table 7). This was especially pronounced for the radial and longitudinal strains, which means that the patients did not have radial contraction and longitudinal shortening as much as the normals. The circumferential motion, although generally smaller in the patients than in the normals, was in some regions (Fig. 36) and for some of the patients close to that of the normals. On the other hand, the three normal subjects had similar strains at any point of the cardiac cycle. Fig. 24 illustrates that the method was able to recover the deformation in a short axis slice relatively accurately for a normal subject and for a patient. The in-plane distance from the virtual to real tag lines was on average about one pixel (Table 7) for the three normal subjects and three patients.

The anatomical and tagged MRI scans were acquired slice by slice using breath-holding, which introduced some misalignment between slices of the same scan and between slices of the anatomical and tagged scans. This acquisition artifact degraded the quality of the recovered deformation and negatively affected the validation measures (false negative rate, false positive rate, true positive rate, and tag intersection distance). However, we did not quantify the amount of this misalignment and consequently we were not able to determine how much it affected the quality of the deformation recovery and validation measures.

Section 3.2 shows examples of the recovered deformation for midventricular and basal regions for representative cases from both studies. The deformation recovery for the apical

region is not shown since it is less reliable. The small cross-sectional area and the oblique angle of the endocardial and epicardial surfaces to the image plane coupled with the thick (8-10 mm) short axis slices result in a pronounced partial volume effect, which makes the apical region poorly defined and consequently more difficult to track than the midventricular and basal regions. The top row of Fig. 1 illustrates that the LV wall is better defined in mid-ventricular and basal regions than in the apical region.

CHAPTER 3

MYOCARDIAL DEFORMATION RECOVERY FROM CINE MRI USING A NEARLY INCOMPRESSIBLE BIVENTRICULAR MODEL

3.1 Methods

3.1.1 3D Nearly Incompressible Transformation Model

Here we present a nearly incompressible model that can model the motion of structures with arbitrary topologies. This allows for modeling of the two cardiac ventricles without composing transformations. One can use the same model to represent the motion of the four cardiac chambers or any other topology. The near incompressibility of the model makes the optimization less sensitive to the optimization parameters.

The model is comprised of a domain of an arbitrary topology and a displacement field defined over the domain. To represent the displacement field we interpolate the displacements specified at a finite number of locations. These locations are referred to as nodes. We use a divergence-free matrix-valued radial basis function scheme [44] to interpolate the displacements at nodes. A consequence of using radial basis functions is that the nodes can be irregularly arranged. This is an advantage over interpolation schemes that require the nodes to be regularly spaced, usually in a form of a grid.

Let $\mathbf{D} \subset \mathbb{R}^3$ denote the domain of the model and let $\mathbf{r} \in \mathbf{D}$ be a point in the domain. The transformation $\mathbf{T} : \mathbf{D} \mapsto \mathbb{R}^3$ is given by

$$\mathbf{T}(\mathbf{r}) = \mathbf{r} + \mathbf{U}(\mathbf{r}), \tag{3.1}$$

where $\mathbf{U}$ represents the corresponding displacement field. The vector interpolation scheme has the following form:

$$\mathbf{U}(\mathbf{r}) = \sum_{j=1}^{M} \mathbf{\Phi}(\mathbf{r} - \mathbf{n}_j)\mathbf{c}_j, \tag{3.2}$$

where $\mathbf{n}_j$ are the node locations, $\mathbf{c}_j$ the corresponding vector coefficients, and $\mathbf{\Phi}$ is a matrix-valued radial basis function. The number of nodes is M. If

$$\mathbf{\Phi}(\mathbf{r}) = \left[\left(1 - \frac{\|\mathbf{r}\|^2}{2\alpha^2} \right) \mathbf{I} + \frac{1}{2\alpha^2} \mathbf{r}\mathbf{r}^T \right] e^{-\frac{\|\mathbf{r}\|^2}{2\alpha^2}}, \tag{3.3}$$

where $\mathbf{I}$ is the identity matrix and α is a positive real number, then it can be shown [44]

that

$$\text{div}\mathbf{U} = 0 \tag{3.4}$$

holds everywhere in the domain, i.e. that the interpolation yields a divergence-free displacement field. The determinant of the Jacobian matrix of the transformation (referred to as Jacobian, J) represents the relative change of local volume. At locations where $J < 1$ the local volume reduces, at locations where $J > 1$ the local volume increases, and at locations where $J = 1$ the local volume remains the same. If $J = 1$ over the entire domain, the transformation is said to be volume-preserving or incompressible. The Jacobian can be expanded in the following way:

$$J = \det \frac{\partial \mathbf{T}}{\partial \mathbf{r}} \tag{3.5}$$

$$= \det \left(\mathbf{I} + \frac{\partial \mathbf{U}}{\partial \mathbf{r}} \right) \tag{3.6}$$

$$= 1 + \text{tr}\frac{\partial \mathbf{U}}{\partial \mathbf{r}} + \text{detr}_2 \frac{\partial \mathbf{U}}{\partial \mathbf{r}} + \det \frac{\partial \mathbf{U}}{\partial \mathbf{r}}, \tag{3.7}$$

where $detr_2$ represents the sum of the principal minors. The third and fourth term of the expansion are small compared to the first two terms for spatially smooth displacement fields, i.e. for displacement fields without sudden spatial changes, which is the case with the myocardial displacements. Thus,

$$J \approx 1 + \text{tr}\frac{\partial \mathbf{U}}{\partial \mathbf{r}}. \tag{3.8}$$

However, $\text{tr}\frac{\partial \mathbf{U}}{\partial \mathbf{r}} = \text{div}\mathbf{U}$, and given Eq. 3.4, it follows that

$$J \approx 1, \tag{3.9}$$

i.e. the proposed transformation is nearly incompressible.

We use the transformation defined by Eqs. 3.1, 3.2, and 3.3 to represent the myocardial deformation from the reference frame to each of the other frames of the cardiac cycle. The end diastole (ED) frame of the cardiac cycle is used as the reference frame by convention. The model domain is defined by segmenting the myocardium in the reference frame. This is the only user interaction needed after which the deformation recovery is done fully automatically. While even this step can be automated, we currently manually segment the

myocardium in the ED frame. Given that there are no restrictions on the number and position of nodes, various node configurations including multi-resolution strategies are possible. We position the nodes in the ED frame automatically using in-house software such that they are approximately uniformly spaced over the LV and RV wall midsurface. Parameter α in Eq. 3.3 is set equal to the average distance between neighboring nodes. Both experimental and theoretical analysis suggest that this is its optimal value. This will be discussed in sections 3.2.1 and 3.3.

Let there be N frames ($i = 1, \ldots, N$) and let the first frame ($i = 1$) be the reference frame. Once the nodes are set in the ED frame, to fully specify the proposed transformation, one needs to provide the values of $\mathbf{c}_j$ coefficients for each frame $2 \leq i \leq N$ (let them be denoted as $\mathbf{c}_{i,j}$). The displacement field from the reference frame to frame i is

$$\mathbf{U}_i(\mathbf{r}) = \sum_{j=1}^{M} \mathbf{\Phi}(\mathbf{r} - \mathbf{n}_j)\mathbf{c}_{i,j}. \tag{3.10}$$

Thus, the displacement field is parameterized with the coefficients $\mathbf{c}_{i,j}$. The transformation from the reference frame to frame i is

$$\mathbf{T}_i(\mathbf{r}) = \mathbf{r} + \mathbf{U}_i(\mathbf{r}). \tag{3.11}$$

One can apply transformation $\mathbf{T}_i$ to any point from the domain, including the nodes. The location of node k in frame i is

$$\mathbf{n}_{i,k} = \mathbf{n}_k + \mathbf{U}_i(\mathbf{n}_k), \tag{3.12}$$

and in the expanded form

$$\mathbf{n}_{i,k} = \mathbf{n}_k + \sum_{j=1}^{M} \mathbf{\Phi}(\mathbf{n}_k - \mathbf{n}_j)\mathbf{c}_{i,j}. \tag{3.13}$$

If the coefficients $\mathbf{c}_{i,j}$ are known, one can compute the node locations in all the frames $\mathbf{n}_{i,k}$ using Eq. 3.13. Conversely, if the node locations in all the frames $\mathbf{n}_{i,k}$ are known, one can compute the coefficients $\mathbf{c}_{i,j}$. Eq. 3.13 can be written for all combinations of i ($1 \leq i \leq N$) and k ($1 \leq k \leq M$), which results in a system of MN linear vector equations that can be solved for $\mathbf{c}_{i,j}$. In either case n_j (the node locations in the reference frame; note that $\mathbf{n}_{1,j} = \mathbf{n}_j$) are assumed to be known. Thus, since the set of coefficients $\mathbf{c}_{i,j}$

and the set of nodes in all the frames $\mathbf{n}_{i,k}$ are equivalent (one can be computed from the other), either one can be used to parameterize the displacement field. We use the node locations in all the frames to parameterize the displacement field since it is more convenient for the optimization, which is discussed in Sec. 3.1.2. By specifying the node positions in the current configuration one can generate various biventricular wall deformation patterns, some of which are shown in Fig. 25.

3.1.2 Biventricular Deformation Recovery

The cardiac deformation is recovered for each frame i other than the reference frame by searching for the locations of the nodes that define transformation $\mathbf{T}_i$ for which the similarity between the reference frame and the transformed frame i is maximized. We use normalized mutual information (NMI) [28] as the similarity measure, which was already used for cardiac deformation recovery [26]. NMI of two images can be written as:

$$NMI(I_1, I_2) = \frac{H(I_1) + H(I_2)}{H(I_1, I_2)}, \tag{3.14}$$

where $H(I_1)$ and $H(I_2)$ are the marginal entropies of I_1 and I_2, respectively, and $H(I_1, I_2)$ is the joint entropy of the two images. NMI takes values between 1 and 2 [45].

While the transformation from the reference frame to any other frame is approximately incompressible (Eq. 3.9), the deviation from incompressibility can be more than 4%, which was experimentally determined as the maximal myocardial volume change (Sec. 1.4). To prevent this from happening, we use a hard constraint in the objective function that prevents deviations from incompressibility larger than 4%. Thus, for each frame $i > 1$ we search for the node locations $\mathbf{n}_{i,k}$ that define transformation $\mathbf{T}_i$ for which the following objective function is maximized:

$$O_i = \begin{cases} 0 \quad if \ \ |1 - J_{\mathbf{T}_i}| > 4\% \\ NMI(\ I_1, I_i(\mathbf{T}_i)\ ) \quad otherwise. \end{cases} \tag{3.15}$$

Here $J_{\mathbf{T}_i}$ is the Jacobian of the transformation $\mathbf{T}_i$, I_1 is the image of the reference frame, I_i is the image of frame i, $I_i(\mathbf{T}_i)$ is the image of frame i transformed by $\mathbf{T}_i$ to the coordinate system of the reference frame. This objective function behaves as NMI as long as the deviation from incompressibility is equal or smaller than 4%. Note that both expansions

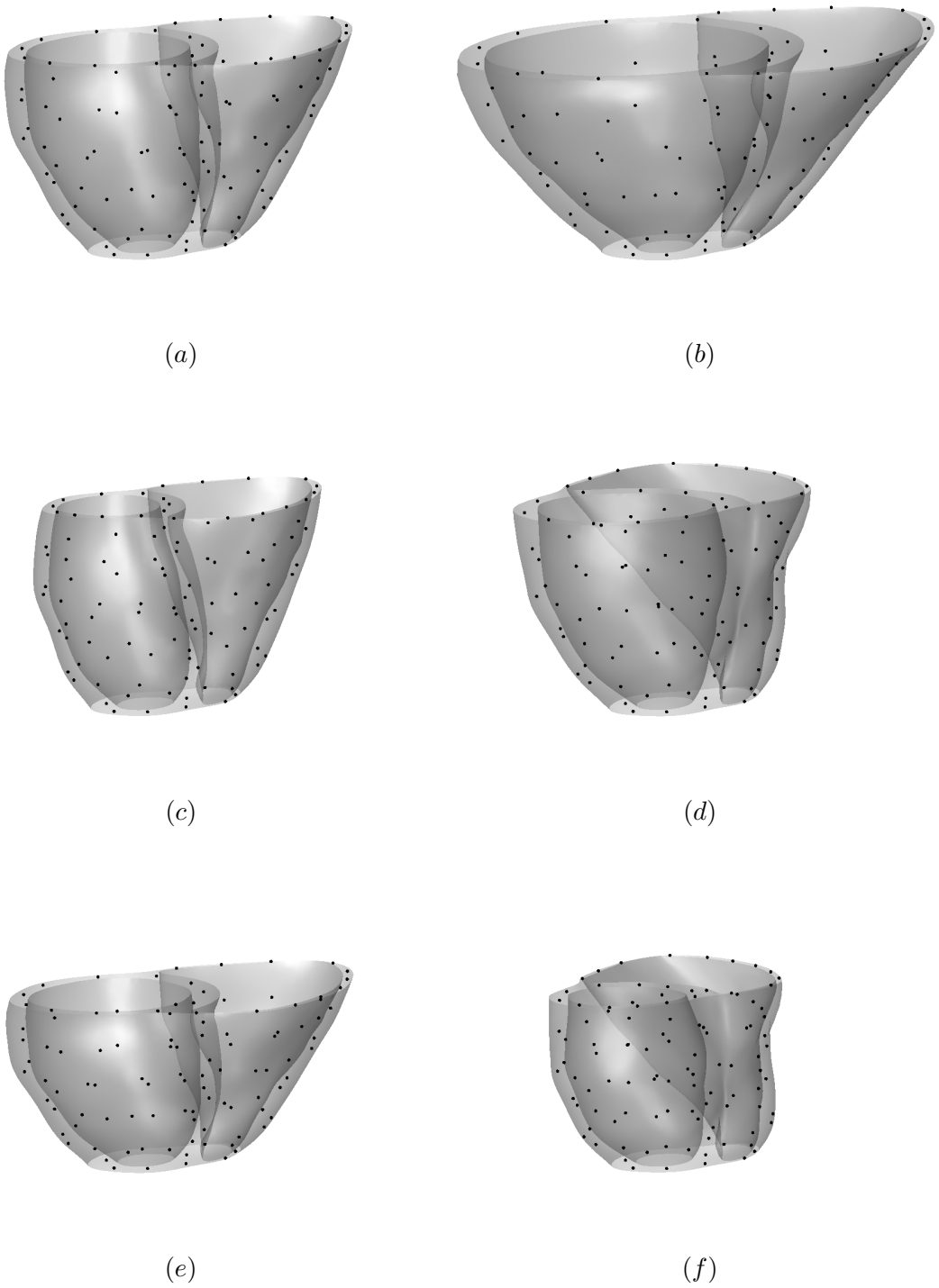

Figure 25. The biventriuclar wall at ED of a healthy volunteer is shown in (a). Artificial transformations are applied to the model to illustrate (b) radial expansion, (c) radial contraction, (d) circumferential twisting, (e) longitudinal shortening, and (f) combined radial contraction, circumferential twisting, and longitudinal shortening, which is a deformation pattern typical for ES. The nodes are the black dots.

and compressions are treated in the same way. If the deviation from incompressibility is more than 4%, the value of the objective function is 0, which is smaller than the values that NMI can take. Since the goal is to maximize O_i, the hard constraint will keep the transformation close to incompressible.

We start the optimization process from the reference frame ($i = 1$) where the locations of the nodes are known. Then, we advance in the forward direction of the cardiac cycle. To determine the node locations in frame i (for $2 \leq i \leq N$), we use the nodes of the previous frame $i - 1$ as their initial locations and maximize Eq. 3.15 by using the gradient descent method. In this way, we obtain the locations of the nodes in each frame i of the cardiac cycle with respect to the forward direction. Let $\mathbf{n}_{i,j}^f$ represent the location of the j-th node in the i-th frame with respect to the forward direction. We perform the same optimization process in the backward direction, which means that we start from the reference frame where the locations of the nodes are known, and we advance in the backward direction of the cardiac cycle. In this way, we obtain the locations of the nodes in each frame i for the backward direction: $\mathbf{n}_{i,j}^b$. The backward and forward optimization processes are performed independently of each other. In the forward propagation errors accumulate in the forward direction, i.e. it is more likely that the nodes in frames 2 and 3 are more accurately positioned than in frames $N - 1$ and N. In the backward propagation errors accumulate in the backward direction, i.e. it is more likely that the nodes in frames N and $N - 1$ are more accurately positioned than in frames 2 and 1. Note that the reference frame ($i = 1$) has identical positions of the nodes for the forward and backward directions. For this reason it makes sense to compute a weighted average of the forward and backward nodes such that the forward nodes get more weight at the beginning of the cardiac cycle (i.e. for smaller values of i) and the backward nodes get more weight at the end of the cardiac cycle (i.e. for larger values of i). A simple way to achieve this is to have the weights linearly depend on the frame number, i.e. the final node locations are given by:

$$\mathbf{n}_{i,j} = [1 - w(i)]\mathbf{n}_{i,j}^f + w(i)\mathbf{n}_{i,j}^b, \tag{3.16}$$

where $w(i) = \frac{1}{N}(i - 1)$. Experiments show that the recovered deformation is better when using the nodes given by Eq. 3.16 than when using only $\mathbf{n}_{i,j}^f$ or only $\mathbf{n}_{i,j}^b$.

3.2 Results

To study the performance of the nearly incompressible biventricular model, we used the same MR protocols and subjects as the ones introduced in section 2.2.1 as well as the same validation procedures as the ones introduced in section 2.1.6.

3.2.1 Method Design Studies

3.2.1.1 Model parameter α

The 3D nearly incompressible transformation model presented in section 3.1.1 has one parameter to be set: α. We performed the following experimental tests that suggest that the optimal value for α is the average distance between neighboring nodes. For different values of α, we measured the distances between the intersections of real tag lines and the corresponding intersections of virtual tag lines as explained in section 2.1.6. We performed this experiment for the two sets of scans of the first study. Fig . 26 shows the average tag errors measured in one midventricular slice for the ES frame as a function of α.

3.2.1.2 Comparison to thin-plate spline

In this paper we use a divergence free matrix-valued radial basis function to interpolate the displacement fields. We showed in section 3.1.1 that this interpolation scheme corresponds to a first order approximation of incompressibility, which is a desirable property since the myocardium has been shown to be nearly incompressible. However other interpolation techniques can be used to model the displacement fields. The most common ones are cubic B-splines and thin-plate splines (TPS) [46]. The divergence free interpolation scheme presented in this paper can be directly compared to TPS since they both do not require the nodes to be regularly spaced, which is not the case for Cubic B splines. We replaced the divergence free interpolation by TPS and applied exactly the same cardiac deformation recovery as presented in section 3.1. To compare the influence of these two interpolation schemes, we measured the distances between the intersections of real tag lines and the corresponding intersections of virtual tag lines for the two sets of scans of the first study. Table 3 gives the average tag errors measured in one midventricular slice for the ES frame.

To further compare the difference in the performance between the methods using the divergence free interpolation and TPS, we measured the percentage of firing nodes over all

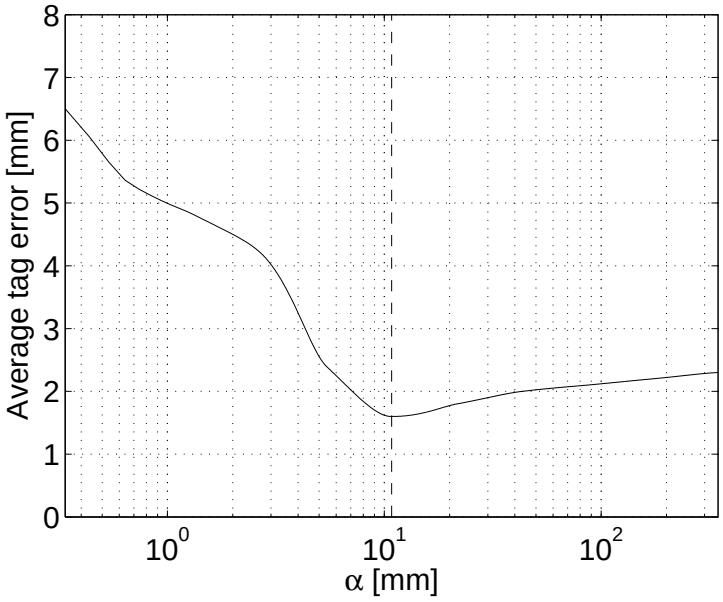

(a)

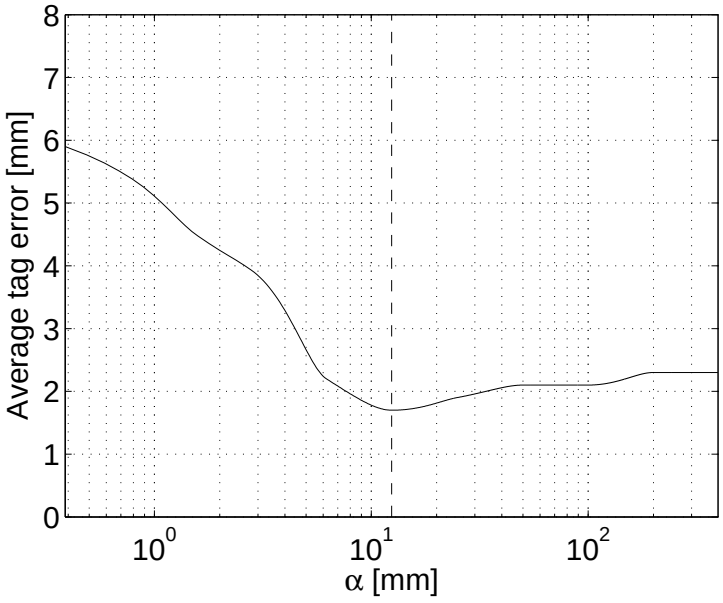

(b)

Figure 26. Average distances between the intersections of real tag lines and the corresponding intersections of virtual tag lines for the ES frame in one midventricular slice as a function of α for (a) the first set and (b) the second set of the repeatability study. The vertical dashed line marks the value of α equal to the average distance between neighboring nodes.

Table 3. Four recovery methods are tested on the scans of the repeatability study: model using divergence free interpolation, TPS, divergence free interpolation without the near-incompressibility constraint, and TPS without the nearly incompressibility. The average distances between the intersections of real tag lines and the corresponding intersections of virtual tag lines for the ES frame in one midventricular are provided for the all the methods. The percentages of firing nodes during the optimization process of the objective function are given for the method including the near-incompressible constraint.

Method	Measure	Scan 1	Scan2
Divergence free	Tag error [mm]	1.6	1.7
	Firing nodes [%]	7.6	9.2
TPS	Tag error [mm]	1.9	1.9
	Firing nodes [%]	20.8	25.3
Divergence free without the nearly incompressibility constraint	Tag error [mm]	2.2	2.1
TPS without the nearly incompressibility constraint	Tag error [mm]	2.4	2.6

the nodes during the optimization process of the objective function for the two sets of scans of the first study. A node fires when the Jacobian of the transformation becomes larger than 4% during the optimization of the objective function, which means that the value of the ejective function becomes 0. The results are presented in Table 3. We also computed for the ES frame the corresponding Jacobian histogram of the transformation. They are displayed in Fig. 27.

3.2.1.3 Near-incompressibility constraint

We explained in section 1.4 that incompressibility is a physical property of the myocardium that should not be ignored. In this paper, the concept of near incompressibility is included in both the design of the transformation model (divergence free interpolation) and the objective function. We removed the near-incompressibility constraint in the objective function, i.e. the objective function is just equal to NMI, and performed the same tests as in section 3.2.1.2. The average distances between the intersections of real tag lines and the corresponding intersections of virtual tag lines for the ES frame are given in Table 3 and the corresponding Jacobian distribution is displayed in Fig. 27.

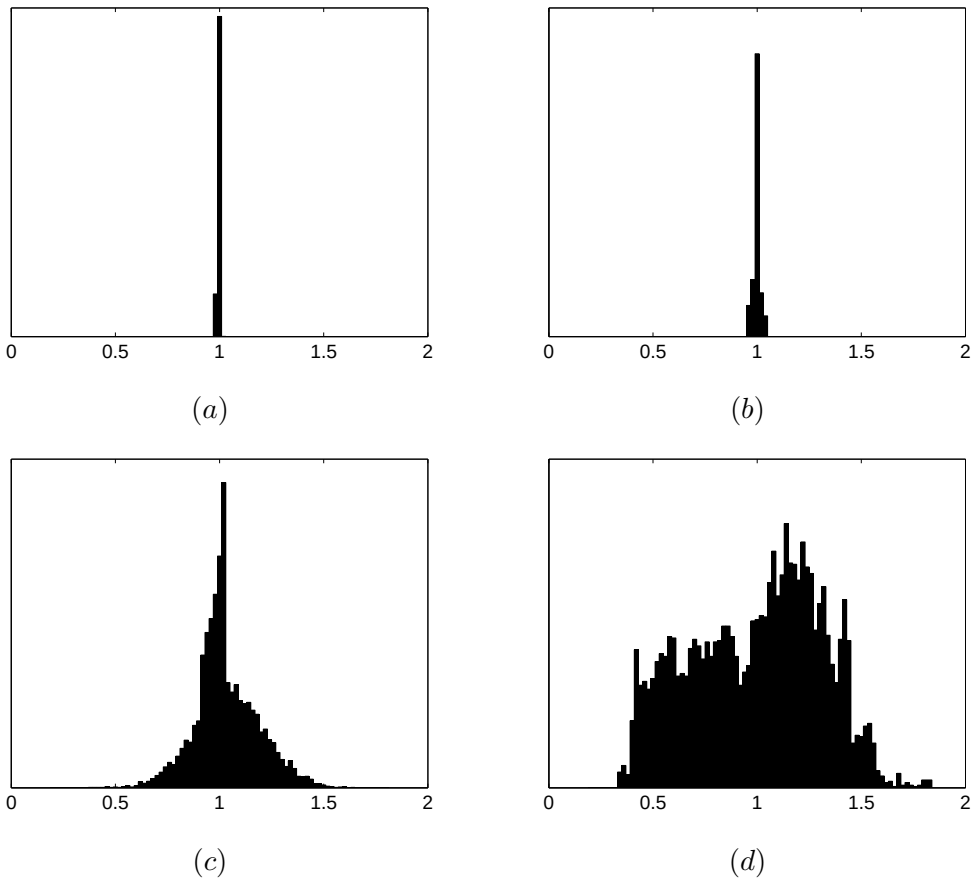

Figure 27. Jacobian distribution for the ES frame of the first scan of the repeatability study for four methods:model using (a) divergence free interpolation, (b) TPS, (c) divergence free interpolation without the near-incompressibility constraint, and (d) TPS without the nearly incompressibility.

Table 4. Three image similarity measures are compared on the scans of the repeatability study: model using NMI, NCC, and MSD. The performance of the biventricular deformation recovery is assessed by comparing the average distances between the intersections of real tag lines and the corresponding intersections of virtual tag lines for the ES frame in one midventricular.

Image similarity measure	Tag error [mm] Scan 1	Tag error [mm] Scan 2
NMI	1.6	1.7
NCC	1.6	1.7
MSD	1.6	1.8

Table 5. The cardiac deformation recovery can be either performed using the reference frame only, or each consecutive frame. The two methods are compared according to the average distances between the intersections of real tag lines and the corresponding intersections of virtual tag lines for the ES frame in one midventricular.

Method	Tag error [mm] Scan 1	Tag error [mm] Scan 2
Reference frame	1.6	1.7
Consecutive frames	1.8	1.6

3.2.1.4 Similarity measure

We use in the proposed method NMI as the image similarity measure. We compared the cardiac deformation recoveries when two other image similarity measures are used: normalized cross correlation (NCC) and mean square difference (MSD). The results are displayed in Table 4.

3.2.1.5 Reference frame mapping

In this paper, the myocardial deformation is represented from the reference frame to each of the other frames of the cardiac cycle (Eqs. 3.1, 3.2, and 3.3). However, the cardiac deformation recovery can also be performed between each consecutive frame of the sequence. Table 5 presents the results when this method is used.

3.2.2 Study: Repeatability

3.2.2.1 Surface Models, Displacement and Strain Fields

The biventricular deformation recovered from the first and the second (taken four months later) anatomical cine MRI scan of the healthy volunteer was very similar.

To display the model boundaries over time, we first constructed a 3D model of the

Table 6. In-plane resolution (IPR), number of model nodes (M), Peak radial strain (PRS) and Peak circumferential strain (PCS) are given for the two scans of the healthy volunteer. PRS and PCS were computed over the cardiac cycle.

Subject	IPR [mm]	M	PRS	PCS
Scan 1	1.41	106	.32	-.14
Scan 2	1.44	99	.34	-.13

biventricular surface in the ED frame. Then, for all other frames, we deformed the surface model by applying the recovered transformation to the model. Fig. 28 shows the contours of the biventricular surface model as well as the corresponding displacement field for a midventricular short axis slice over the cardiac cycle for the first scan of the study.

Fig. 29 shows the Lagrangian radial and circumferential strain fields (section 2.1.5) over the cardiac cycle for a midventricular short axis slice for the first scan of the study.

To further evaluate the strains, we sectored the domain in the reference configuration into the standard sectors, as defined in [39]. Then for each sector, for each strain type, we computed the average strain for that sector as a function of time over the cardiac cycle. We did this for both the first and the second anatomical cine MRI scan of the healthy volunteer. The time curves for the radial, and circumferential strains for all the sectors are shown in Figs. 30 and 31, respectively. The peak values of the radial and circumferential strains over the cardiac cycle for the two scans of the healthy volunteer are given in Table 6.

3.2.2.2 Validation

To quantitatively evaluate the biventricular wall deformation recovered from the anatomical cine MRI scan we validated it against the manually segmented myocardial wall and against the manually positioned tag lines in the corresponding tagged cine MRI scans, both over the entire cardiac cycle.

For the first validation procedure, we manually segmented the biventricular wall in all the frames of the 3D anatomical cine MRI. Then we applied the recovered deformation to the biventricular wall segmented in the ED frame and mapped it to all other frames. Finally, we quantified the agreement between the manual and model generated biventricular wall segmentation by means of true positive, false negative and false positive rates. Fig.

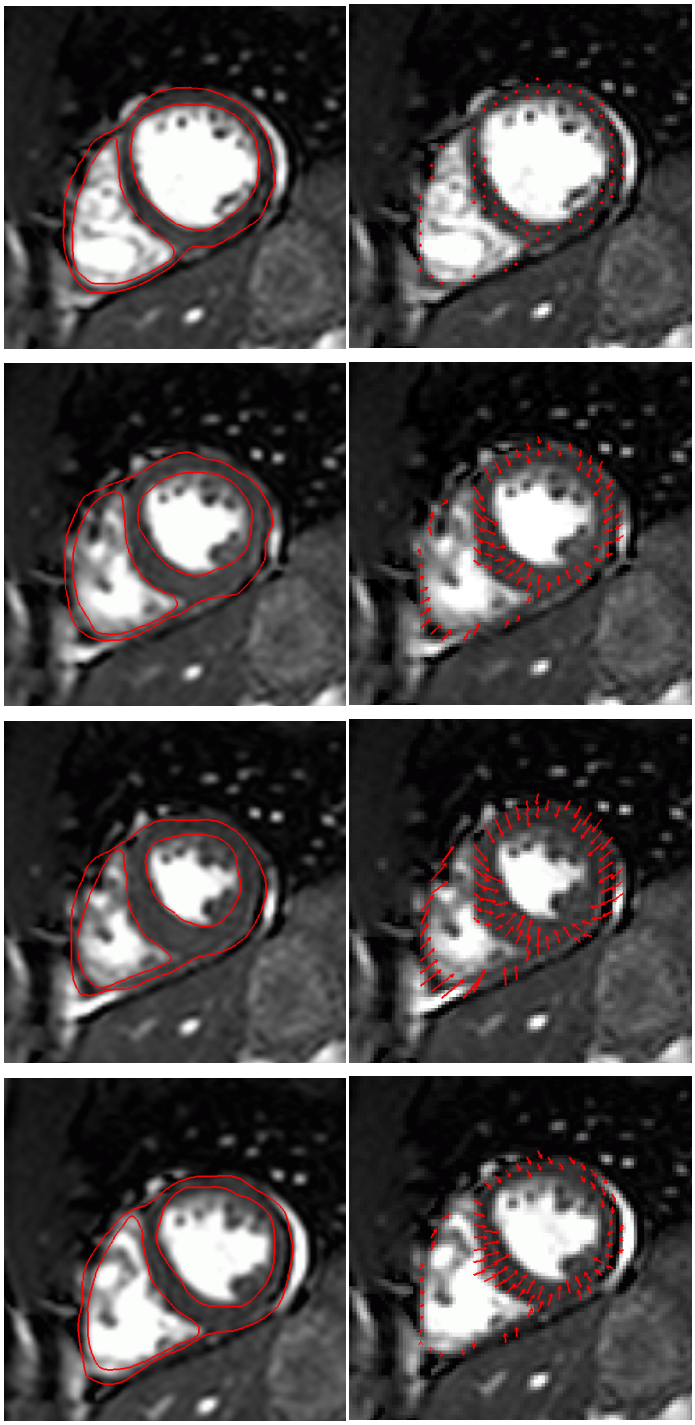

(a) (b)

Figure 28. The recovered biventricular wall deformation for a normal subject over the cardiac cycle (first row: ED, third row: ES): a midventricular slice overlaid with (a) the contours, (b) the projected displacements.

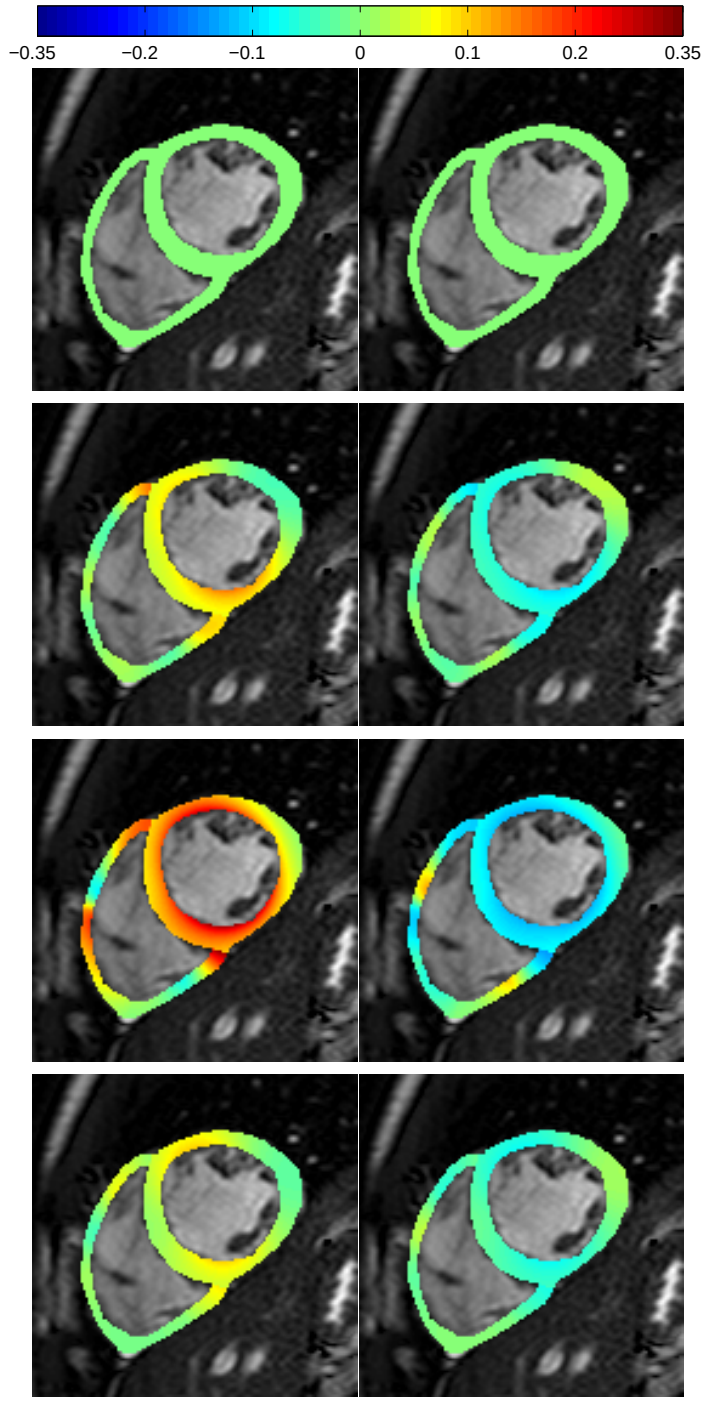

Figure 29. Color-coded (a) radial and (b) circumferential Lagrangian strains for a normal subject are shown in a midventricular slice over the cardiac cycle (first row: ED, third row: ES). Since the deformation is measured relative to ED, the strains in the ED frame are zero. The strains are shown over the ED frame image.

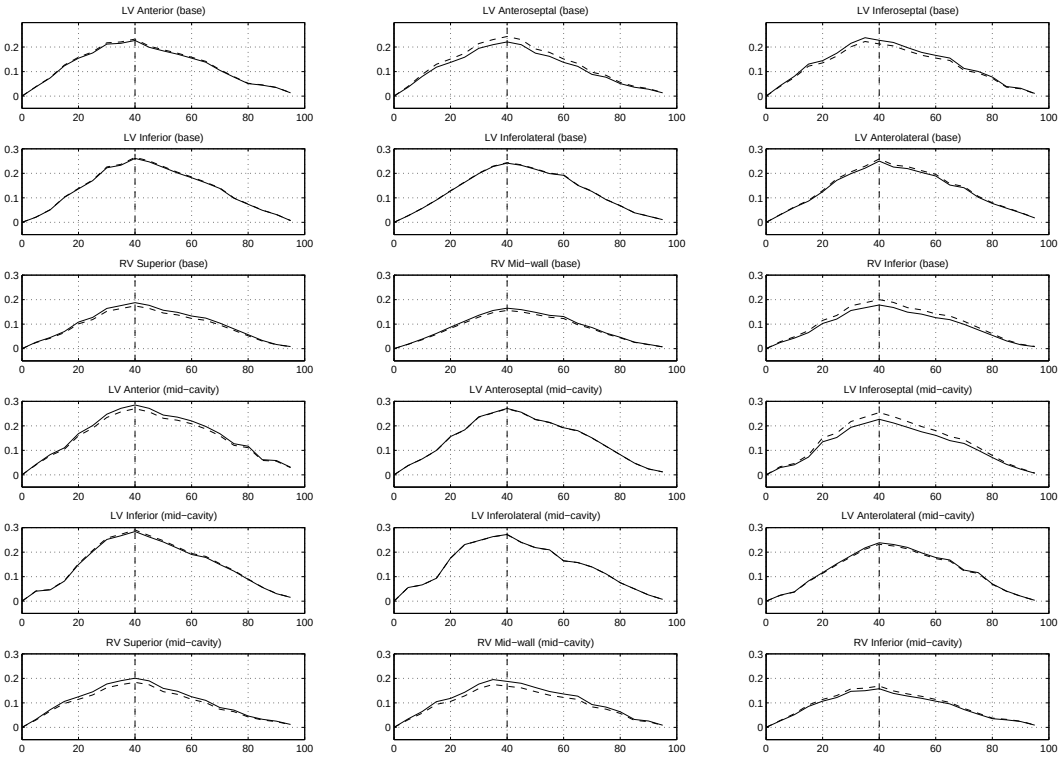

Figure 30. The radial strain for 18 standard midventricular and basal sectors of LV and RV as functions of time over the cardiac cycle for the first (solid curve) and the second (dashed curve) anatomical cine MRI scan of a healthy volunteer. The horizontal axis represents the time as a percentage of the cardiac cycle starting from ED. The vertical dashed line marks ES. Note the good agreement of the two curves for each sector.

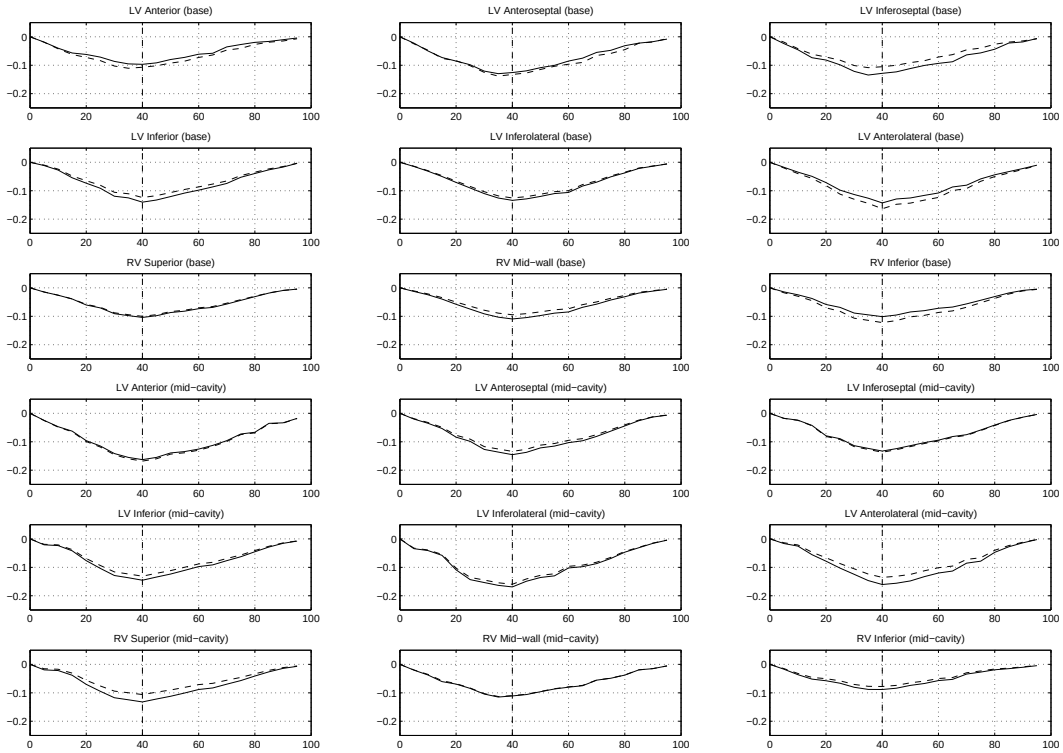

Figure 31. The circumferential strain for 18 standard midventricular and basal sectors of LV and RV as functions of time over the cardiac cycle for the first (solid curve) and the second (dashed curve) anatomical cine MRI scan of a healthy volunteer. The horizontal axis represents the time as a percentage of the cardiac cycle starting from ED. The vertical dashed line marks ES. Note the good agreement of the two curves for each sector.

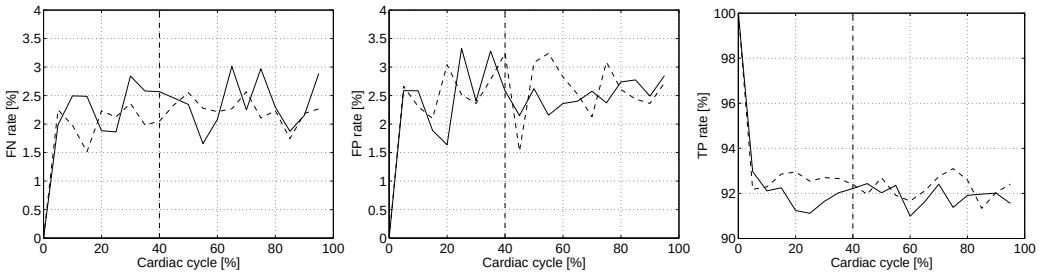

Figure 32. The false negative (FN), false positive (FP), and true positive (TP) rates for the volume agreement over the cardiac cycle between the manually segmented and model generated biventricular wall for the first (solid curves) and second (dashed curves) scan of the healthy volunteer. The horizontal axis represents the time as a percentage of the cardiac cycle starting from ED. The vertical dashed line marks ES. Since the deformation is measured relative to ED, the FN and FP rates are 0% and TP rate is 100% at ED.

32 shows the three rates over the cardiac cycle for the first and second scan of the healthy volunteer.

For the second validation procedure, we manually positioned tag planes in the ED frame of the 3D tagged cine MRI. Then we applied the deformation recovered from the anatomical scan to the tag planes positioned in the ED frame of the tagged scan and mapped them to all other frames of the tagged scan. Fig. 34 shows the virtual tag lines for a midventricular slice for the second scan of the healthy volunteer. Finally, we measured the distances between the intersections of real tag lines and the corresponding intersections of virtual tag lines for all the frames for both the first and the second scan of the healthy volunteer. The results are displayed in Fig. 33.

3.2.3 Study: Comparison of Normals and Patients

3.2.3.1 Strain Fields

We sectored the domain in the reference configuration into the standard sectors, as defined in [39]. Then for each sector, for each strain type, we computed the average strain for that sector as a function of time over the cardiac cycle. We did this for both the first and the second anatomical cine MRI scan of the healthy volunteer. The time curves for the radial, and circumferential strains for all the sectors are shown in Figs. 35 and 36, respectively.

3.2.3.2 Validation

To quantitatively evaluate the biventricular wall deformation recovered from the anatomical cine MRI scan for the three normal subjects and three patients we validated it against the

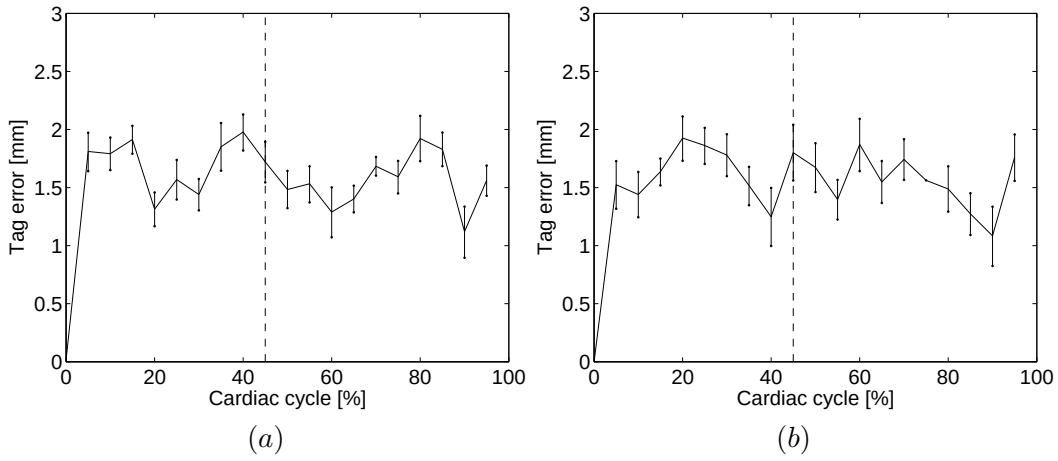

Figure 33. The mean and standard deviation of the manually measured distances between the intersections of real tag lines and the corresponding intersections of virtual tag lines over the cardiac cycle for (a) the first and (b) the second scan of the healthy volunteer. The horizontal axis represents the time as a percentage of the cardiac cycle starting from ED. The vertical dashed line marks ES. Since the deformation is measured relative to ED, the distances are zero in the ED frame.

manually segmented biventricular wall and against the manually positioned tag lines in the corresponding tagged cine MRI scan.

For the first validation procedure, we manually segmented the biventriuclar wall in the ED and ES frames of the 3D anatomical cine MRI. Then we applied the recovered deformation to the LV wall segmented in the ED frame and mapped it the ES frame. Finally, we quantified the agreement between the manual and model generated myocardial wall segmentation in the ES frame by means of true positive, false negative and false positive rates. Table 7 shows the three rates for the three normal subjects and three patients.

For the second validation procedure, we manually positioned tag planes in the ED frame of the 3D tagged cine MRI. Then we applied the recovered deformation to the tag planes positioned in the ED frame and mapped them to all other frames. Fig. 37 shows the virtual tag lines for a short axis slice for a normal subject and a patient. Finally, we measured the distances between the intersections of real tag lines and the corresponding intersections of virtual tag lines for the ES frame for the three normal subjects and three patients. The results are given in Table 7.

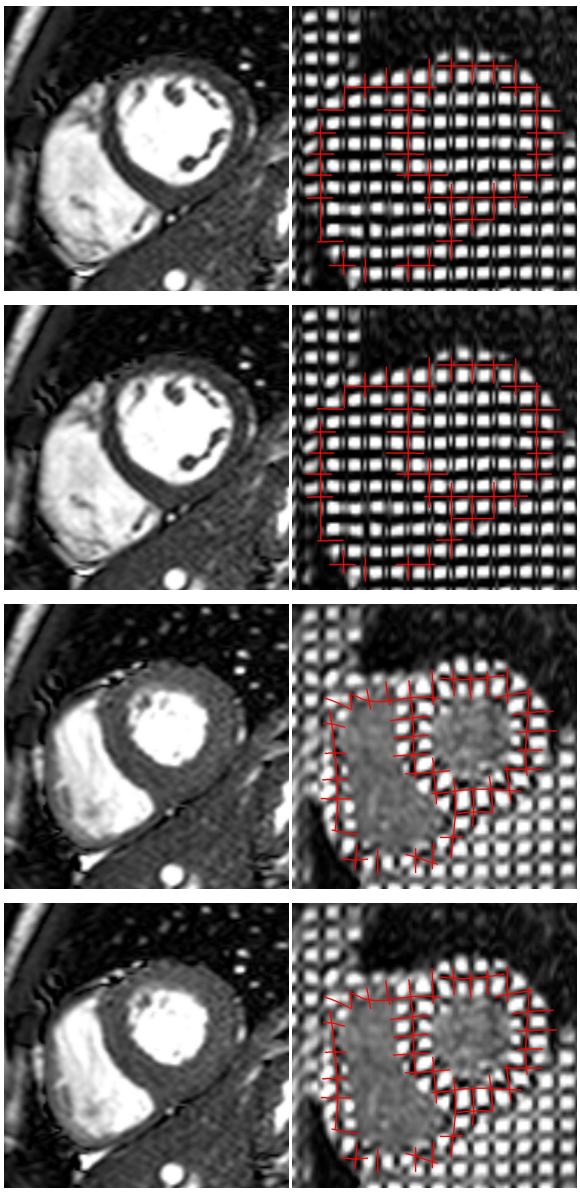

(a) (b)

Figure 34. A midventricular short axis slice from the anatomical cine MRI scan is shown in (a) over the cardiac cycle (first row: ED, third row: ES). The corresponding slice in the tagged cine MRI overlaid with virtual tag linescan is shown in (b). The virtual tag lines were generated by applying the deformation recovered from the anatomical scan to the manually positioned tag planes at ED. The images are from the second scan of the healthy volunteer.

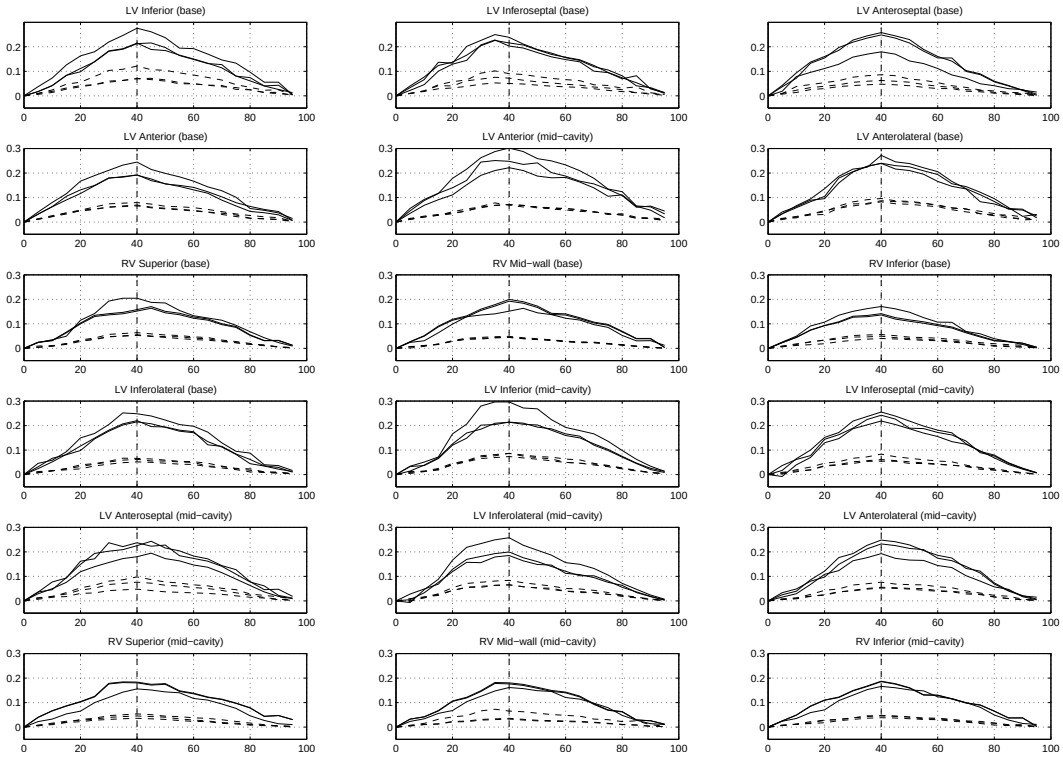

Figure 35. The radial strain for 18 standard midventricular and basal sectors of LV and RV as functions of time over the cardiac cycle for the three normal subjects (solid curves) and the three patients (dashed curves). The horizontal axis represents the time as a percentage of the cardiac cycle starting from ED. The vertical dashed line marks ES. Note the similarity of the time curves for the normals, the similarity of the time curves for the patients, and a clear difference between time curves of the normals and of the patients.

,

Table 7. In-plane resolution (IPR), number of model nodes (M), True positive rate (TPr), False positive rate (FPr), False Negative rate (FNr), the average (± std) distance between manually and automatically obtained intersections of perpendicular tag planes (Tag error), Peak radial strain (PRS) and Peak circumferential strain (PCS) are given for the three normal subjects and thee patients. TP rate, FP rate, FN rate, and Tag error were computed for the ES frame whereas PRS and PCS were computed over the entire cardiac cycle.

Subject	IPR	M	TPr	FPr	FNr	Tag error		PRS	PCS
	$[mm]$		[%]	[%]	[%]	$[mm]$	$[pixel]$		
Normal 1	1.24	124	91.2	3.1	3.2	1.7±.3	1.2±.1	.32	-.18
Normal 2	1.36	120	92.1	3.0	2.8	1.5±.2	1.1±.2	.37	-.15
Normal 3	1.41	106	91.8	2.4	3.0	1.8±.2	1.2±.1	.35	-.16
Patient 1	1.52	115	92.5	3.2	3.1	1.9±.2	1.2±.2	.11	-.09
Patient 2	1.35	128	92.6	2.8	2.5	1.7±.3	1.2±.1	.10	-.07
Patient 3	1.56	110	91.9	2.9	2.8	1.7±.3	1.1±.2	.13	-.08

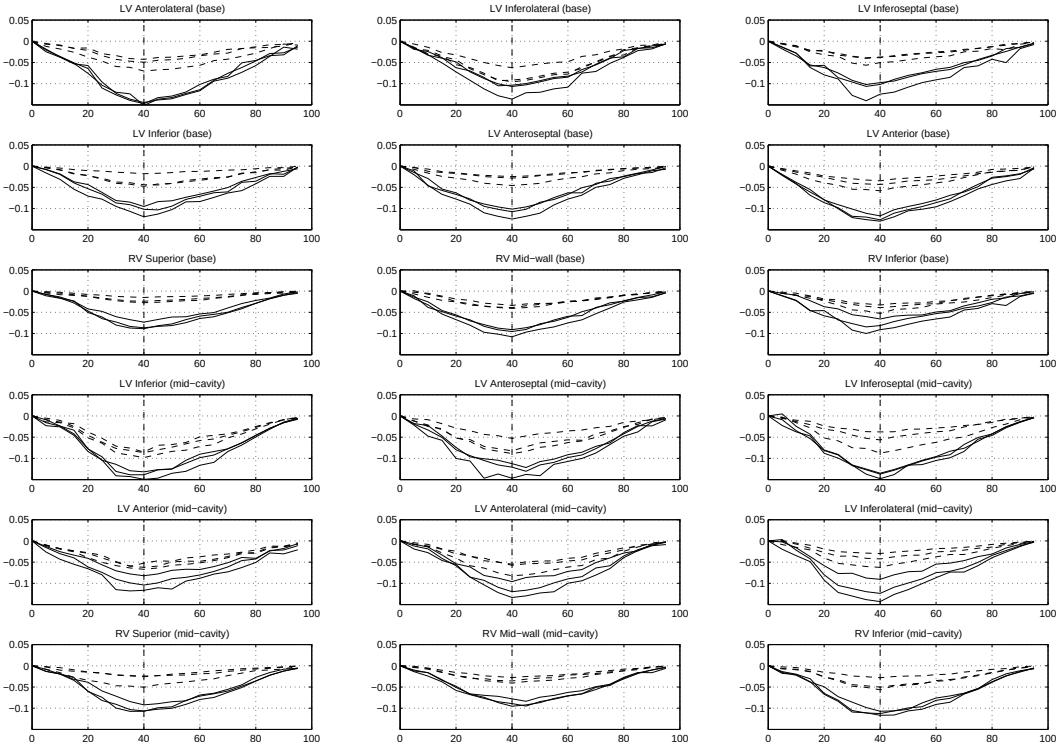

Figure 36. The circumferential strain for 18 standard midventricular and basal sectors of LV and RV as functions of time over the cardiac cycle for the three normal subjects (solid curves) and the three patients (dashed curves). The horizontal axis represents the time as a percentage of the cardiac cycle starting from ED. The vertical dashed line marks ES. Note the similarity of the time curves for the normals. For most of the sectors the patients had a weaker circumferential strain than the normals.

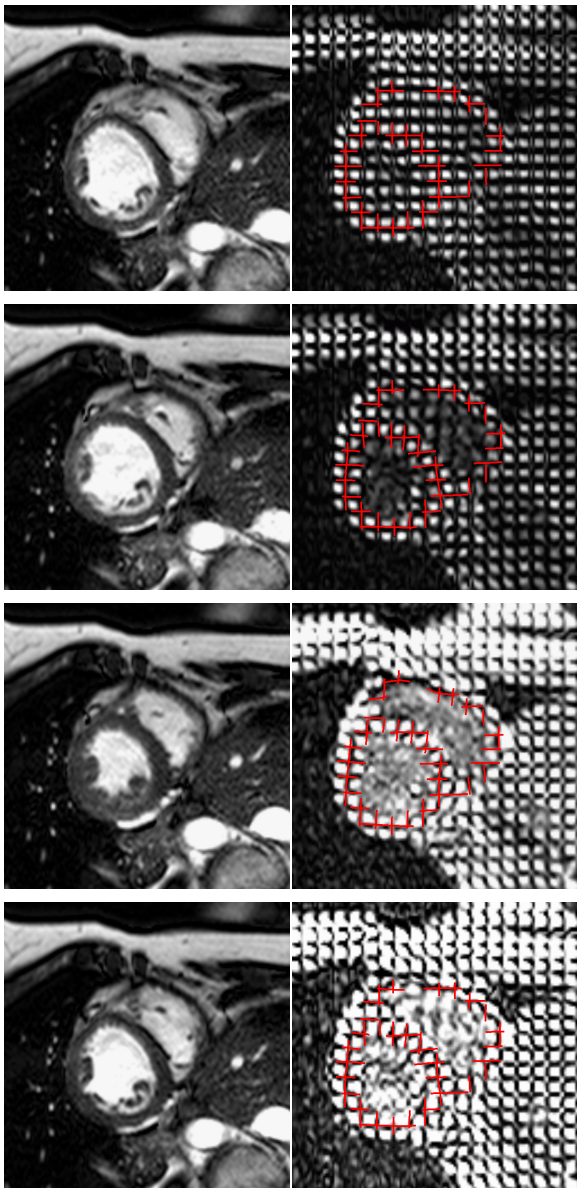

(a) (b)

Figure 37. A midventricular short axis slice from the anatomical cine MRI scan is shown in (a) over the cardiac cycle (first row: ED, third row: ES). The corresponding slice in the tagged cine MRI overlaid with virtual tag lines is shown in (b). The virtual tag lines were generated by applying the deformation recovered from the anatomical scan to the manually positioned tag planes at ED. The images are from a patient case.

3.3 Discussion

3.3.1 Deformable Model

The proposed deformable model has the following properties: it is volumetric, it behaves uniformly in all the regions, its displacement field is C_1 continuous, it is nearly incompressible, it is capable of generating realistic cardiac deformation patterns and normal strains. Fig. 25f shows a deformation pattern typical for ES, which is a combination of radial contraction, circumferential twisting, and longitudinal shortening. Normals strains are shown in Sec. 3.2 and discussed in Sec. 3.3.2.

The proposed deformable model is a volumetric model (as opposed to a surface model), since it maps a 3D domain (as opposed to a surface) in the reference configuration to the current configuration. The domain is defined by segmenting the biventricular wall at ED.

All the regions, apical, midventricular, and basal, are treated equally by the model, unlike models based on the cylindrical, spherical and prolate spheroidal coordinate systems that have points ("poles") that require special treatment. At the poles some of the displacement derivatives are not defined, which in turn causes the strain tensor not to be defined. As a consequence, the deformation recovered at and in vicinity of the poles is not correct. When such coordinate systems are used, typically one pole is at the apex, which prevents one to model the apical region [9]. The proposed model does not have this limitation since it has no poles or other special points or directions.

In our model the displacements specified at a finite number of locations referred to as nodes are interpolated to obtain divergence free displacement fields. We position the nodes in the ED frame automatically such that they are approximately uniformly spaced over the biventricular wall midsurface. We compared the proposed divergence free interpolation to TPS in the performance of the cardiac deformation recovery. Table 3 shows that the average distance between the intersections of real tag lines and the corresponding intersections of virtual tag lines is smaller when the divergence free interpolation is used. The first reason for this is that incompressibility is a physical property that has to be included in the modeling of the heart as explained in the next paragraph. While the divergence free interpolation corresponds to a first order approximation of incompressibility, TPS do not penalize any deviation from incompressibility. The second reason is that a hard constraint is used in

the objective function to prevent any deviation from incompressibility more than 4%. The optimization of the objective function is performed by moving the nodes in the ED frame according to the gradient descent algorithm. However during the optimization process, some nodes can lead to a deviation from incompressibility larger than 4%, which fires the objective function and penalize its optimization. Since the divergence free interpolation is a first order approximation of incompressibility, it will give a smaller number of firing nodes as seen in Table 3. The divergence free interpolation is thus more adapted for the optimization of the objective function than TPS.

Given that incompressibility is a physical property of the myocardium (Section 1.4), deformable models that are used for cardiac deformation recovery should keep their Jacobian from deviating from 1 by more than a 4%. The proposed model introduces a hard constraint in the objective function to impose that condition. The Jacobian of a deformable model, if not monitored, can easily significantly deviate from 1 (Fig. 27), causing physically incorrect deformations. The importance of Jacobian follows from the fact that it is the determinant of the deformation gradient tensor (Eq. 2.14), which is used to compute strain (Eq. 2.13). This means that an incorrect Jacobian implies an incorrect deformation gradient tensor, which in turn implies incorrect strain. Table 3 shows also that the average distance between the intersections of real tag lines and the corresponding intersections of virtual tag lines is smaller when the deformation recovery method keeps the Jacobian from deviating from 1 by more than a 4%. This means that the biventricular deformation recovery is more accurate is the nearly incompressibility condition is enforced.

Fig. 26 shows that the average distance between the intersections of real tag lines and the corresponding intersections of virtual tag lines is the smallest when the parameter α of our model is the average distance between neighboring nodes. The theoretical explanation of this is that the interpolation affects a smaller neighborhood around each node when α is smaller and a larger neighborhood around each node when α is larger. On one hand, if α becomes smaller than the average distance between neighboring nodes, the interpolation will provide information only to a smaller neighborhood around nodes. In this case the deformation recovery is wrong in between the neighborhood affected by the interpolation. On the other hand, if α becomes larger than the average distance between neighboring

nodes, the interpolation becomes more spread out and the Jacobian distribution becomes less concentrated around 1, which leads to a larger number of firing nodes.

In the proposed method, we used NMI as the similarity measure. Section 3.2.1.4 showed that there is not clear advantages for using other image similarity measures like MSD or NCC. We use NMI since it is more robust to changes in image intensity characteristics that may occur especially for diseased or abnormal patients. Section 3.2.1.5 shows that there is also no clear advantage for using transformation between consecutive frames in the cardiac deformation recovery. We use transformations that are based on the reference frame. In this case, there is no propagation of cardiac deformation recovery errors and the registration is symmetric and transitive.

3.3.2 Results

The method accurately tracked the endocardial and epicardial boundaries in the short axis views (Fig. 28). The recovered displacement field of the same subject (Fig. 28) shows that the myocardium both synchronously contracted and twisted, which is a typical deformation pattern for normal subjects. The radial and circumferential strain maps (Fig. 29) and time curves (Figs. 30, 31) show strain patterns typical for normal subjects: radial strain increases from ED to ES and then comes back to zero at the end of the cycle, while circumferential strains decrease from ED to ES and come back to zero at the end of the cycle. Strain curves of normal subjects with similar shapes and peak values were reported by researchers using tagged MRI [37, 9, 13], DENSE MRI [7, 40] and echocardiography [41]. To validate the method, we applied the recovered deformation to the segmented biventricular wall at ED, mapped it to all other frames, and compared it to the corresponding manual segmentation. Fig. 32 shows the false negative, false positive, and true positive rates of the agreement between the model and manual segmentation over the cardiac cycle for the two scans of the first study. One can see that the false positive and negative rates were about 2.5 % and the true positive rate was about 92 % everywhere in the cycle. These numbers reflect both the deformation recovery error and the inaccuracy of the manual segmentation. To further validate the method, we applied the recovered deformation to the virtual tag planes manually positioned in ED and compared them to the tag planes in all other frames. This is

illustrated in Fig. 34 for a midventricular short axis slice over the cardiac cycle. The errors (distances) between the corresponding intersections of real and virtual tag lines over the cardiac cycle for the two scans are shown in Fig. 33. One can see that the errors are mainly between 1 and 2 mm. Given that the in-plane resolution of the two scans is over 1.4 mm, it follows that the method was able recover the deformation from anatomical MRI scans with an error of up to 1.5 pixels in short axis planes relative to the corresponding tagged MRI scans. Figs. 28, 29, and 34 show deformation recovery results for the second scan of the first study. The corresponding results obtained for the first scan of the first study are not shown since they are very similar. A quantitative comparison of the deformation recovery from the two scans is shown in Figs. 30 and 31 for strains, in Fig. 32 for the volume rates and in Fig. 33 for the tag errors, all over the entire cardiac cycle. All the measures (strain values, volume rates, and tag errors) are very similar between the two scans and the difference is within the accuracy of the method. This suggests that the method has the quality of repeatability, i.e. when applied to repeated scans of the same subject it produces similar deformation recovery results.

The proposed method shows clearly different deformation patterns between the normal subjects and the patients: the patient lacked radial contraction and synchronous motion, which are characteristics of a normal cardiac motion and which were present in the deformation of the normal subject. This implied a low ejection fraction for the patient. The reduced cardiac function of patients can also be seen in the strain time curves (Figs. 35, 36). The strains of the patients had consistently lower peak values than the corresponding strains of the normal subjects (Table 7). This was especially pronounced for the radial strains, which means that the patients did not have radial contraction as much as the normals. The circumferential motion, although generally smaller in the patients than in the normals, was in some regions (Fig. 36) and for some of the patients close to that of the normals. On the other hand, the three normal subjects had similar strains at any point of the cardiac cycle. Fig. 37 illustrates that the method was able to recover the deformation in a short axis slice relatively accurately for a normal subject and for a patient. The in-plane distance from the virtual to real tag lines was on average about one pixel (Table 7) for the three normal subjects and three patients.

The proposed method is similar to the method of Lorenzo-Valdes et al. [26] with the main difference being that we use a nearly incompressible transformation model while they modeled the cardiac deformation using cubic B-splines. A direct consequence of this is that our method needs a smaller number of parameters to represent the cardiac deformation. The number of model nodes used for the six cases are reported in Table 7. The use of cubic B-splines would require for these cases approximatively twelve times more nodes to cover the biventricular wall in order to keep the same distance between the nodes. Thus, we can not fairly directly compare the two methods. Furthermore, the percentage of firing nodes would be larger than for the presented method, which means that the objective function in Eq. 3.15 would not be as well optimized as with the proposed method.

CHAPTER 4

GENERATION OF MYOCARDIAL WALL SURFACE MESHES FROM SEGMENTED MRI

4.1 Mesh generation in Medical Imaging

Surface models of the epicardium and endocardium of the heart chambers are used in a number of biomedical applications for visualization [47], virtual reality [48], segmentation [49, 19], motion analysis [23, 29], shape analysis [50, 51] and modeling [52, 53] purposes. A typical approach to generate subject specific models is to apply a surface construction algorithm to segmented cardiac magnetic resonance or computer tomography images. Cardiac MRI is, after echocardiography, the most frequently used modality to image the heart. However, due to the tradeoff between image quality and temporal and spatial resolution, voxels in cardiac MR images are strongly anisotropic. Typically, the in-plane resolution is a few times higher than the out-of-plane resolution for clinically used cardiac MRI. While a number of mesh generation methods exist [54, 55], to the best of our knowledge, there is no surface mesh generation method designed for images with strongly anisotropic voxels. The most widely used method for surface mesh generation from images is the marching cubes method [56]. If the marching cubes method is applied to an image with strongly anisotropic voxels without any additional processing, then the generated mesh has strongly irregular triangles, pronounced terracing artifacts and the number of triangles directly related to the number of voxels, as shown in Fig. 38. Once the marching cubes mesh is generated, one can apply a number of techniques to improve the mesh quality, including mesh smoothing [57], simplification [58], and optimization [59]. Such an approach was undertaken in [60]. An alternative way to use the marching cubes is to first construct an implicit surface from the segmented image, and then apply the marching cubes to the scalar field (the implicit surface is the zero level set of the scalar field) on a uniformly sampled image domain [61]. This way one can control the size of the mesh triangles (determined by the sampling interval) as well as make them more regular (consequence of the uniform sampling), but they can still be badly shaped and the terracing artifacts remain. To alleviate these problems, Peiró *et al.* [61] used a number of mesh optimization techniques. Instead of using the discrete

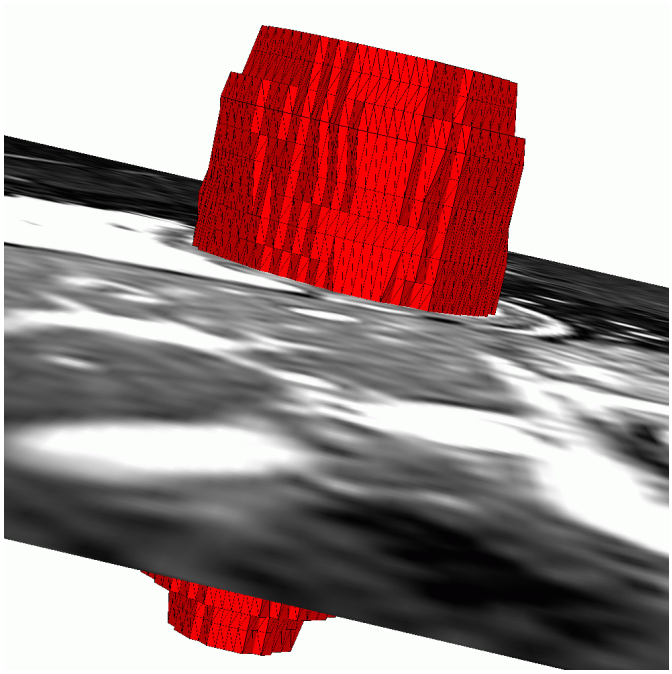

Figure 38. A left ventricular surface model generated by applying the marching cubes algorithm to a segmented cardiac MR image with 1.44 mm in-plane resolution and 8.0 mm slice thickness. The irregular triangles are a consequence of the voxel anisotropy. The surface mesh has pronounced terracing artifacts and the number of triangles is directly related to the number of voxels in the image.

image, one can interpolate image intensities, e.g. by means of trilinear interpolation, before constructing a surface mesh [62]. However, in the case of strongly anisotropic voxels, this approach would still result in terracing artifacts, although somewhat smoothed. Lötjönen *et al.* [63] also used the marching cubes as the starting point of their mesh generation method, which, if the mesh is decimated enough, generates close-to-regular triangles. The method of Gibson [64], while significantly reducing terracing artifacts, shares with the marching cubes the problem of irregular triangles in the case of anisotropic voxels. Another group of methods constructs surface meshes from 2D contours of the segmented image structures [65, 66, 67, 68]. They suffer from the same problem: if the voxels of the underlying image are anisotropic the resulting triangles are irregular.

Here we present a method for generation of myocardial wall surface meshes from segmented MRI. The meshes are smooth, have pre-specified number of triangles and close-to-regular triangles despite the highly anisotropic voxels. Since the marching cubes is the most widely used method, either as a stand-alone method or as a part of other methods, we compare the proposed method to the marching cubes.

4.2 Methods

4.2.1 Approach

The presented method is designed for surface mesh generation of the endocardium of the four cardiac chambers and of the endocardium from segmented cardiac MRI. The four endocardial surfaces are, if the valves are ignored, topologically equivalent to a sphere. We also assume that the segmentation of the entire heart does not include other structures, which makes its outer surface topologically equivalent to a sphere. The main idea is to generate a triangulated mesh on a sphere and then map it independently to the five surfaces. For each segmented object we construct its surface in implicit form and then map the mesh from the sphere to the surface using the gradient field of the solution of the Laplace equation between the surface and the sphere. Each step of the method is explained in the following sections and Fig. 39 summarizes the method.

4.2.2 Sphere Triangulation

It can be shown that a sphere cannot be triangulated with an arbitrary number of equilateral triangles. In fact, there are only three configurations of a triangulated sphere with equilateral triangles: regular tetrahedron (4 equilateral triangles), regular octahedron (8 equilateral triangles) and regular icosahedron (20 equilateral triangles) [69]. A triangulation of a sphere with any other number of triangles cannot have all the triangles equilateral. There are a number of ways to approximately uniformly sample a sphere and construct the corresponding triangulation [70, 71]. Here we use the method of minimizing the electrostatic energy of equally charged particles on a sphere [72, 73]. Once the points are approximately uniformly distributed on a sphere, we construct a triangular mesh by using the Delaunay triangulation [74]. This method allows for the construction of a close-to-regular triangular mesh on a sphere with an arbitrary number of vertices V, which is related to the number of triangles T as $2V - T = 4$. This relationship follows from the Euler's formula for polyhedra [69].

4.2.3 Solution of the Laplace Equation

In order to construct the surface mesh, we define a homeomorphic mapping from the sphere to the surface and apply it to the mesh on the sphere. There are infinitely many ways to construct such a mapping, and here we define a scalar field u between the sphere and the surface (we make the sphere larger than the object and center it at the barycenter of the object), and then any point from the sphere is mapped to the surface by following ∇u, the gradient of u. In order for the mapping to be homeomorphic, the gradient flow has to be divergence free, i.e. $\mathrm{div}\nabla u = 0$, which leads to the familiar Laplace equation,

$$\Delta u = 0. \tag{4.1}$$

We look for the solution of the Laplace equation that is equal to 0 at the sphere and 1 at the object surface. The Laplace operator is rotation invariant and a solution to the Laplace equation has no local extrema, which makes it a suitable means to transport the mesh from the sphere to the surface of the object. If the sphere has a radius of R, then the external

boundary condition can be specified as

$$u(\mathbf{r})|_{|\mathbf{r}|=\mathbf{R}} = 0. \tag{4.2}$$

The internal boundary condition is discussed in Section 4.2.4. We use the method of fundamental solutions to solve the Laplace equation. The solution is continuous (as opposed to discrete) and it is represented as a linear combination of functions, each satisfying the Laplace equation and the external boundary condition and each having a singularity within the sphere (see Appendix C),

$$u(\mathbf{r}) = \sum_{m=1}^{M} c_m f_{\mathbf{s}_m}(\mathbf{r}), \tag{4.3}$$

where $\mathbf{s_m}$, $m = 1, ..., M$ are the locations of M singularities and c_m the corresponding coefficients. It is straightforward to show that u from (4.3) satisfies the Laplace equation (4.1) and the external boundary condition (4.2).

4.2.4 Internal Boundary Condition

While the expression (4.3) and the external boundary condition are in the continuous form, the internal boundary is discrete, defined by the object segmentation map. The strongly anisotropic voxels are the main reason for irregular triangles and terracing effects present in the meshes generated by methods based on the marching cubes. For this reason, we represent the internal boundary in the continuous form as a level set of u from (4.3). First, we define the set of boundary points $\mathbf{r_n}$, $n = 1, ..., N$. For each pair of neighboring voxels from the segmentation map that have different labels (i.e. one voxel belongs to the object and one does not) the midpoint between the two voxels is a boundary point. Then, we determine the parameters (singularity locations and coefficient values) of u such that its level set of 1 fits the boundary points in the least squares sense, i.e. we minimize

$$O = \frac{1}{2} \sum_{n=1}^{N} [u(\mathbf{r_n}) - 1]^2. \tag{4.4}$$

We require all the singularities to be located within the object. Each singularity has the corresponding singularity outside the sphere (see Appendix C). Scalar field u is well defined in the domain (between the object surface and the sphere) since there are no singularities. However, there is no closed form solution that involves the optimal locations of the singularities. To avoid numerical optimization which is prone to local extrema, we preset the

singularity locations, and then find the optimal coefficients c_m that minimize (4.4). While a closed form solution for the optimal coefficients can easily be obtained, in the general case some of the optimal coefficients can have positive and some negative values. However, around each singularity with a negative coefficient there will be a region with negative values of u (u will tend to $-\infty$ at such singularities). These "islands" of negative values may be fully contained within the object but they also may protrude into the domain between the object surface and the sphere, affecting the 1 level set in an undesired way. To prevent this from happening, one can constrain the optimization to have only positive values for c_m. However, there is no closed form solution of this problem. To avoid numerical optimization which is prone to local extrema, we resort to an alternative approach. We approximately uniformly place the singularities inside the object relatively close to the object surface (see Sec. 4.2.6), and assume that all the coefficients have the same value, i.e. $c_m = c$. The optimal value of c is obtained from

$$\frac{\partial O}{\partial c} = 0, \tag{4.5}$$

which has a closed form solution

$$c = \frac{\sum_{n=1}^{N} d_n}{\sum_{n=1}^{N} d_n^2}, \tag{4.6}$$

where $d_n = \sum_{m=1}^{M} f_m(\mathbf{r_n})$. It can be shown that $c > 0$, i.e. there will be no singularities with negative coefficients, which could lead to undesired mesh shapes. However, since the same coefficient is used for all the singularities, the fitting of the implicit surface (level set 1 of u) to the boundary points is not as accurate as in the case of singularities with non-equal coefficients. To increase the accuracy of the fitting, we use a stopping function (see Section 4.2.7).

4.2.5 Mesh Propagation from the Sphere to the Surface

To map the mesh from the sphere to the object surface, we propagate each mesh vertex along the gradient of u, i.e. the trajectory $\mathbf{r}(t)$ of a given vertex $\mathbf{v}$ on the sphere is

$$\frac{d\mathbf{r}(t)}{dt} = \nabla u(\mathbf{r}(t)), \tag{4.7}$$

$$\mathbf{r}(0) = \mathbf{v}. \tag{4.8}$$

where t is the parameter of the trajectory. We use the fourth-order Runge-Kutta method [38] to integrate the trajectory numerically. Since u is a continuous and exact solution of the Laplace equation, the only propagation error comes from the numerical integration error of the Runge-Kutta method. If the Laplace equation was solved approximately, the non-exactness of the solution would be translated into additional propagation error.

4.2.6 Placement of Singularities

To uniformly place the singularities inside the object relatively close to the object surface, we first approximately uniformly sample the sphere (as explained in Sec. 4.2.2) with the number of points equal to the number of singularities. Then, we resample the segmentation map to obtain isotropic voxels and erode the segmented object two times. In the next step, we numerically solve the Laplace equation between the sphere (with a boundary condition of 0) and the surface of the eroded object (with a boundary condition of 1) by using a relaxation method [38]. We utilize the isotropic voxels as the grid on which we solve the Laplace equation. Finally, we propagate the points from the sphere to the eroded object in the direction of the gradient of the solution of the Laplace equation to obtain the singularity locations.

4.2.7 Stopping Function

To increase the accuracy of the fitting of the object surface to the boundary points, instead of propagating the mesh from the sphere to the level set of 1, we define a "stopping" function on the sphere, which for every point on the sphere determines the value of u that point will be propagated to (that value would be 1 if the mesh was propagated to the level set of 1).

To represent the stopping function we use pseudo thin plate spline model on the sphere proposed by Wahba [75],

$$b(\hat{\mathbf{p}}) = \alpha_0 + \sum_{k=1}^{K} \alpha_k \psi(\hat{\mathbf{p}} \cdot \hat{\mathbf{q}}_k), \tag{4.9}$$

where $\hat{\mathbf{p}}$ is a unit vector representing a point on the sphere, K is the number of control points, $\hat{\mathbf{q}}_k$ are unit vectors defining the control points on the sphere, $\alpha_0, \ldots, \alpha_K$ are scalar coefficients, and ψ is defined in [75] for $m = 4$. We set the control points $\hat{\mathbf{q}}_k$ by approximately uniformly sampling a sphere (as explained in Sec. 4.2.2) with K points.

At this point the singularity locations as well as coefficient c are set, i.e. the scalar field u is completely defined. At each boundary point $\mathbf{r_n}$ we record the value of the scalar field $u(\mathbf{r_n})$. Let $\hat{\mathbf{p}}_n$ denote the unit vector of the point on the sphere obtained by propagating the boundary point $\mathbf{r_n}$ to the sphere by following the negative gradient of u. We determine $\alpha_0, \ldots, \alpha_K$ by requiring $b(\hat{\mathbf{p}})$ at points $\hat{\mathbf{p}}_n$ to approximate values $u(\mathbf{r_n})$ in the least squares sense, i.e. by minimizing

$$\sum_{n=1}^{N} \left[b(\hat{\mathbf{p}}_n) - u(\mathbf{r_n}) \right]^2 . \tag{4.10}$$

The closed form solution is

$$\begin{bmatrix} \alpha_0 \\ \alpha_1 \\ \vdots \\ \alpha_K \end{bmatrix} = \left(G^T G \right)^{-1} G^T \begin{bmatrix} u(\mathbf{r_1}) \\ u(\mathbf{r_2}) \\ \vdots \\ u(\mathbf{r_N}) \end{bmatrix} , \tag{4.11}$$

where

$$G = \begin{bmatrix} 1 \, \psi(\hat{\mathbf{p}}_1 \cdot \hat{\mathbf{q}}_1) \cdots \psi(\hat{\mathbf{p}}_1 \cdot \hat{\mathbf{q}}_K) \\ 1 \, \psi(\hat{\mathbf{p}}_2 \cdot \hat{\mathbf{q}}_1) \cdots \psi(\hat{\mathbf{p}}_2 \cdot \hat{\mathbf{q}}_K) \\ \vdots \quad \vdots \quad \vdots \\ 1 \psi(\hat{\mathbf{p}}_N \cdot \hat{\mathbf{q}}_1) \cdots \psi(\hat{\mathbf{p}}_N \cdot \hat{\mathbf{q}}_K) \end{bmatrix} . \tag{4.12}$$

Coefficient c is computed such that (4.4) is minimized, which means that the values $u(\mathbf{r_n})$ are close to 1. Coefficients $\alpha_0, \ldots, \alpha_K$ are computed such that (4.10) is minimized, which means that $b(\hat{\mathbf{p}}_n)$ is close to $u(\mathbf{r_n})$, which in turn is close to 1. Since typically points $\hat{\mathbf{p}}_n$ relatively densely cover the sphere, the stopping function $b(\hat{\mathbf{p}})$ is close to 1 everywhere on the sphere.

We propagate the mesh vertices from the sphere to the object surface according to (4.7) and (4.8). For a given mesh vertex $\mathbf{v}$ on the sphere, the corresponding unit vector is $\frac{\mathbf{v}}{|\mathbf{v}|}$ and the value of the stopping function for that vertex is $b(\frac{\mathbf{v}}{|\mathbf{v}|})$. Over the course of propagation the underlying value of the scalar field $u(\mathbf{r}(t))$ grows and when it reaches $b(\frac{\mathbf{v}}{|\mathbf{v}|})$ the propagation stops.

Instead of using the value of 1 to stop all the vertices, we increase the accuracy of the fitting of the boundary points by using the stopping function. The more control points the more accurate the fitting, and the fewer control points the smoother the final surface.

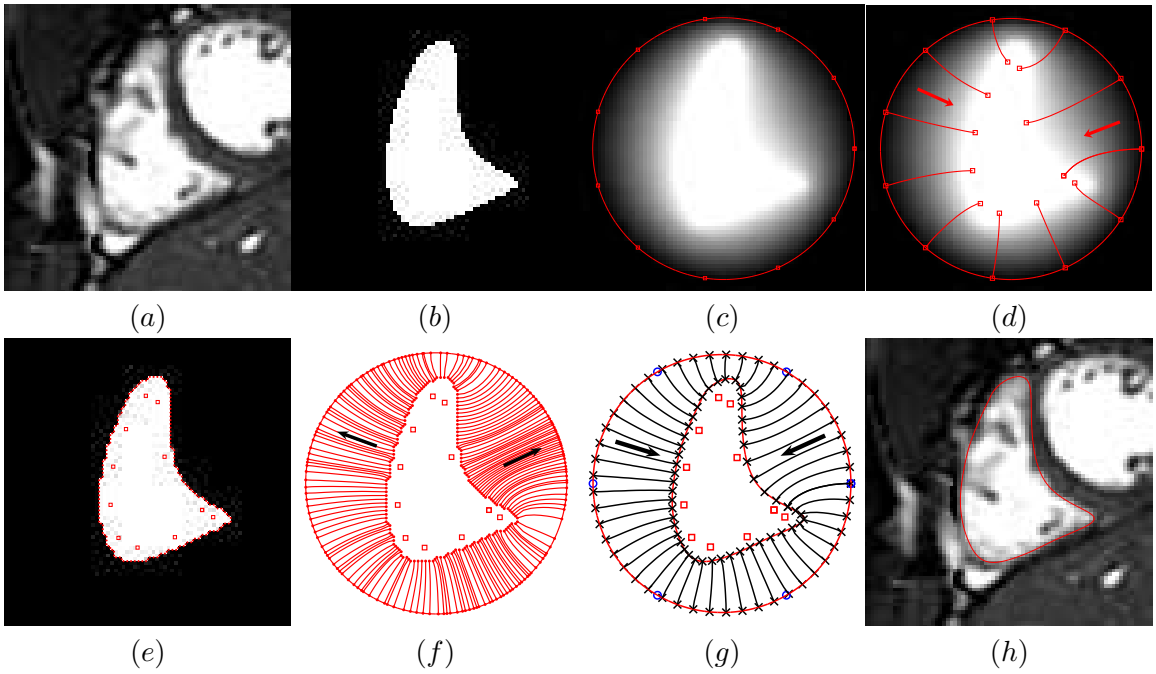

Figure 39. Mesh generation summary. The input image (a) is segmented into the object and background, resulting in a binary image (b). A sphere enclosing the object is centered at the object barycenter (c). The sphere is uniformly sampled with the number of points equal to the number of singularities. The binary image is resampled with isotropic voxels and the Laplace equation is numerically solved between the sphere (boundary condition of 0) and the object (boundary condition of 1). The solution of the Laplace equation is encoded in the gray levels in (c) and (d). The binary object is eroded and the points are propagated from the sphere to the eroded object in the direction of the gradient of the Laplace equation solution to define the singularity locations, shown as red squares in (d) and (e). Boundary points, specified as midpoints for each pair of neighboring voxel, where one voxel is in the object and the other is in the background, are shown as red dots in (e). The singularity locations as well as the boundary points are used to specify the analytic solution of the Laplace equation. The boundary points are propagated in the negative gradient direction of the solution of the Laplace equation from the object boundary to the sphere (f). Their values of the underlying solution of the Laplace equation are interpolated at the sphere to the define the stopping function. The number of degrees of freedom of the stopping function is defined by the number of control points, which are shown as blue circles in (g). An approximately uniform mesh is generated on the sphere. The vertices of the mesh on the sphere, shown as black crosses in (g), are propagated from the sphere in the direction of the gradient of the solution of the Laplace equation until the value of the underlying solution of the Laplace equation is equal to the corresponding value of the stopping function. The propagated mesh nodes define the final mesh, shown in (h). Figures (a)-(h) are two-dimensional for illustration purposes, while the method is three-dimensional.

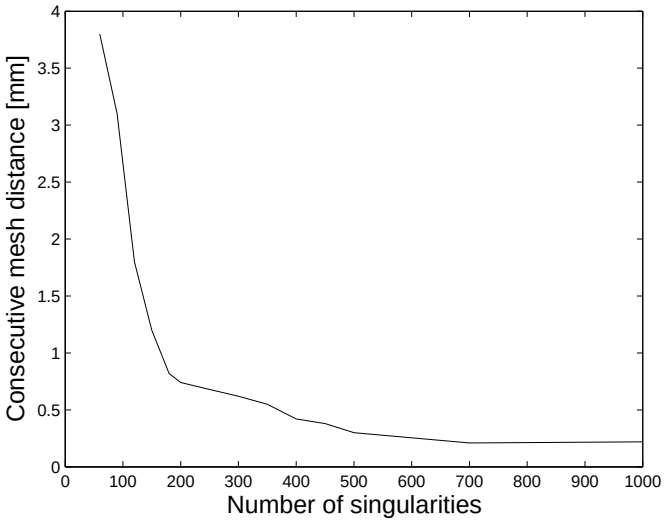

Figure 40. Average distance between consecutive meshes as a function of the number of singularities.

4.3 Results

4.3.1 Method Parameters

The presented method has three parameters: the number of singularities (M), the number of control points (K) and the number of mesh vertices (V). Note that M and K affect the shape of the continuous implicit surface, while V affects the triangulation of the continuous implicit surface.

In this section we analyze the effect of the parameter values on the resulting mesh. The studies were done on the right ventricle of one of the subjects, since the right ventricle is more curved than the other three chambers and is the only chamber that has both convex and concave regions.

In the first study we generated a sequence of surface meshes by increasing the number of singularities. Then we computed the average distance between consecutive meshes in the sequence to quantify the change the mesh undergoes as M is increased (Fig. 40).

In the second study we generated a sequence of surface meshes by increasing the number of control points. Then we computed the average distance between consecutive meshes in the sequence to quantify the change the mesh undergoes as K is increased (Fig. 41).

In the third study we generated a sequence of surface meshes by increasing the number of mesh vertices. Then we computed the average distance between consecutive meshes in

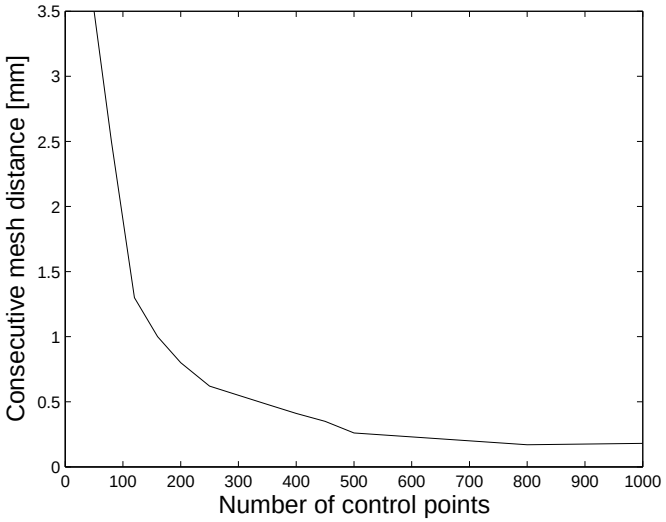

Figure 41. Average distance between consecutive meshes as a function of the number of control points.

the sequence to quantify the change the mesh undergoes as V is increased (Fig. 42).

4.3.2 Mesh Quality

To measure the mesh quality, we use a triangle quality index suggested in [61], which can be evaluated as

$$Q = \frac{8(p-a)(p-b)(p-c)}{abc}, \quad p = \frac{a+b+c}{3}, \tag{4.13}$$

where a, b, and c are the lengths of the three sides of the triangle. It can be shown that $0 \leq Q \leq 1$ for any triangle, $Q = 1$ for an equilateral triangle, Q is close to zero for irregular triangles, and $Q = 0$ for a zero-area triangle. Triangles with $Q > .5$ are considered to be of reasonably good quality.

We generated a sequence of surface meshes by increasing the number of mesh vertices. Then we computed the average quality index for each mesh in the sequence (Fig. 43).

One can see that the quality index is practically independent of the number of mesh vertices and that it is relatively high ($Q \approx .85$).

It should be noted that the average Q cannot be 1. This is true even for the sphere, since it cannot be triangulated with an arbitrary number of equilateral triangles. Fig. 44 shows the mesh on the sphere and the corresponding right ventricular mesh for four different numbers of mesh vertices and reports the corresponding Q values.

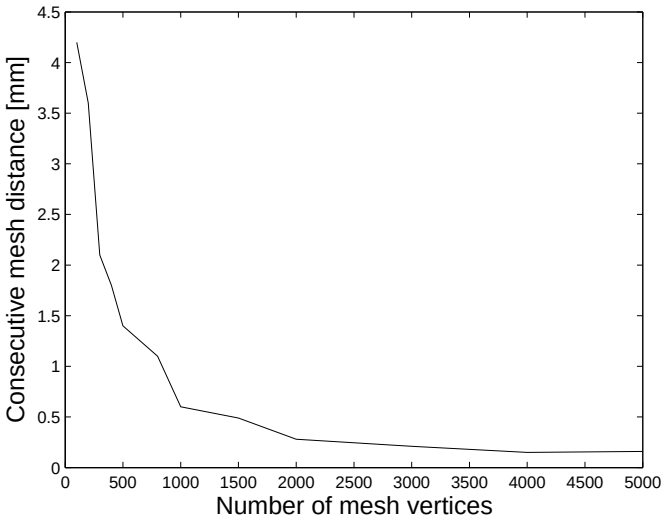

Figure 42. Average distance between consecutive meshes as a function of the number of mesh vertices.

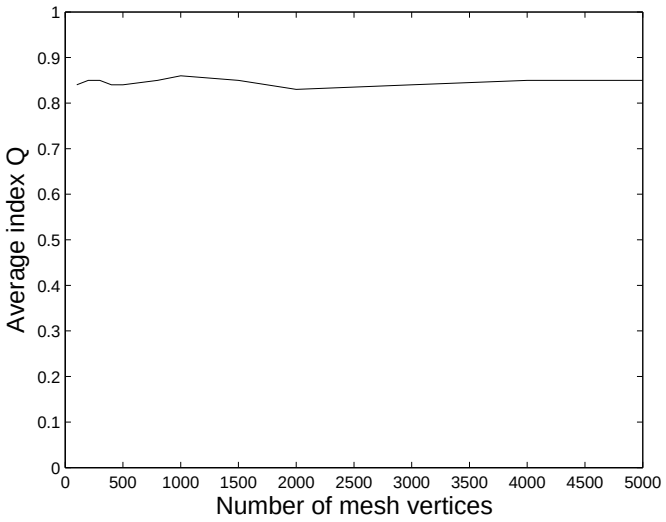

Figure 43. Average triangle quality index as a function of the number of mesh vertices.

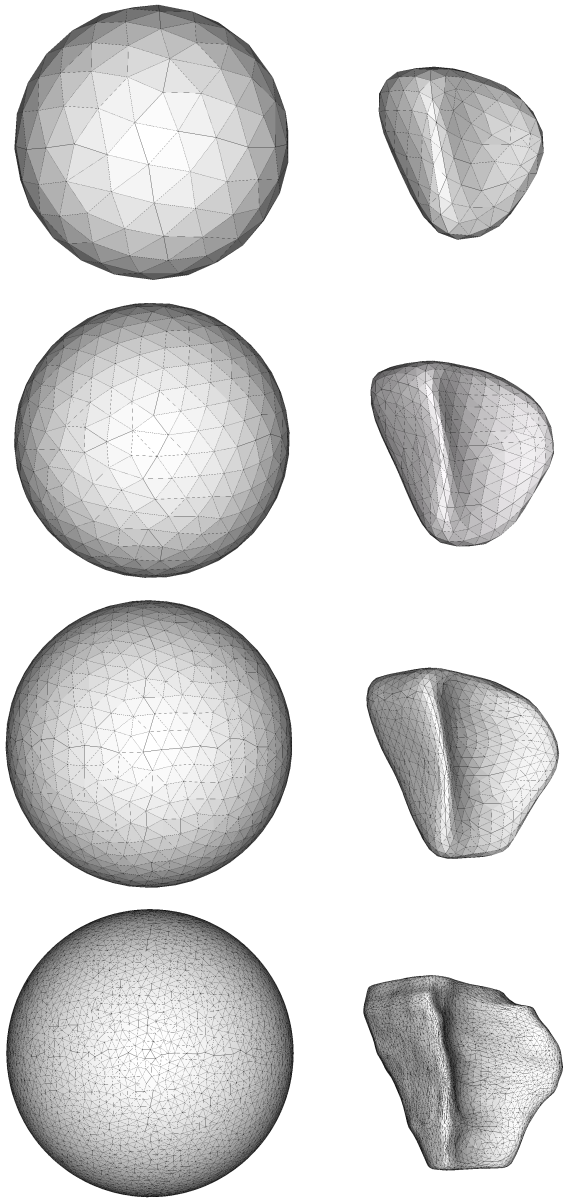

Figure 44. Each row shows a mesh on the sphere and the corresponding right ventricular mesh obtained by propagating the mesh from the sphere to the right ventricular surface. The number of mesh vertices for the four rows are 200, 500, 1000, and 5000. The corresponding mean ± std (min, max) Q values for the mesh on the sphere are $.93 \pm .07(.75, 1)$**,** $.94 \pm .06(.78, 1)$**,** $.93 \pm .07(.77, 1)$**, and** $.95 \pm .05(.76, 1)$**, and for the right ventricular mesh are** $.85 \pm .07(.68, .99)$**,** $.84 \pm .06(.62, .99)$**,** $.86 \pm .06(.65, .99)$**, and** $.85 \pm .07(.63, .99)$**.**

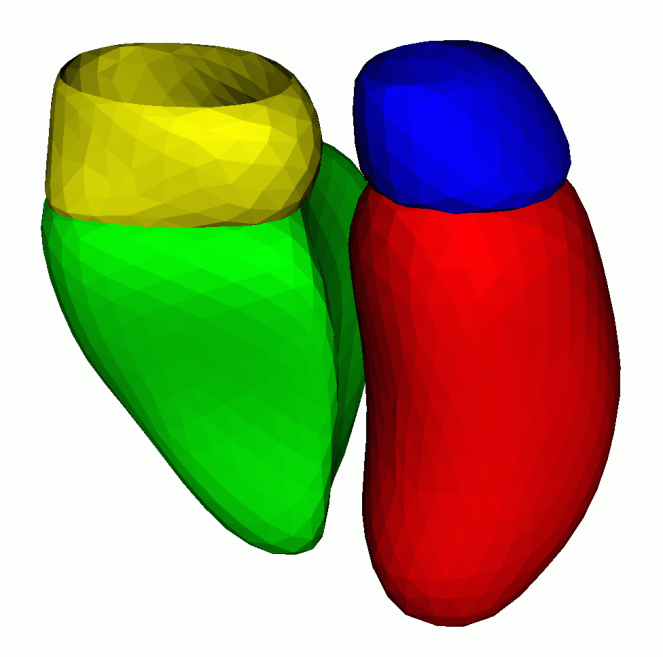

Figure 45. Endocardium surface meshes generated by the proposed method for the left ventricle (red), right ventricle (green), left atrium (blue), and right atrium (yellow).

4.3.3 Comparison to the Marching Cubes

The method was tested on the endocardial surfaces of the four cardiac chambers as well as on the epicardial surface of the entire heart for five subjects. The number of singularities, control points, and mesh vertices used for the test are reported in Table 8. Figs. 45 and 46 show the endocardial and epicardial surface meshes for one of the subjects.

Since the marching cubes is the most widely used method, either as a stand-alone method or as a part of other methods, we compared the endocardial and epicardial surface meshes of the five subject generated by the proposed method to the corresponding surface meshes generated by the marching cubes. The comparison was done in the short-axis slices since the in-plane resolution was 5 times higher than the out-of-plane resolution. Fig. 47 shows cross-sections of segmented blood pools and the corresponding contours from endocardial meshes obtained by the marching cubes and the proposed method.

Table 8 provides the average in-slice distance between the surface meshes generated by the marching cubes and the proposed method. The averages were computed over all the short-axis slices of each cardiac chamber for the five subjects.

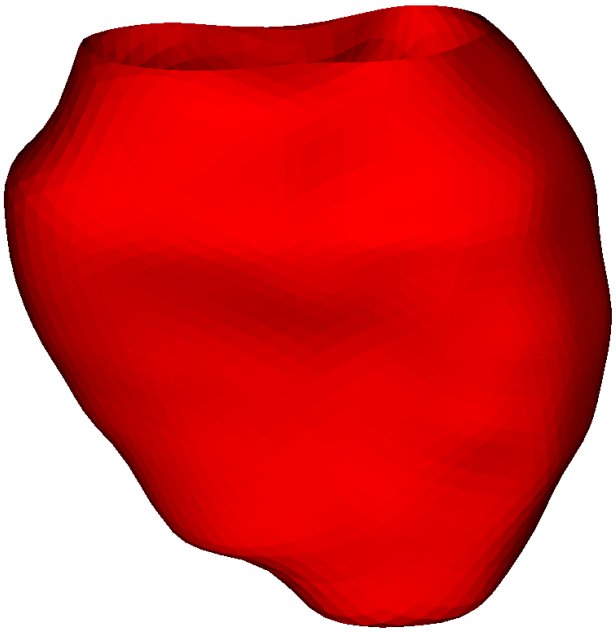

Figure 46. Epicardium surface mesh generated by the proposed method for the entire myocardium.

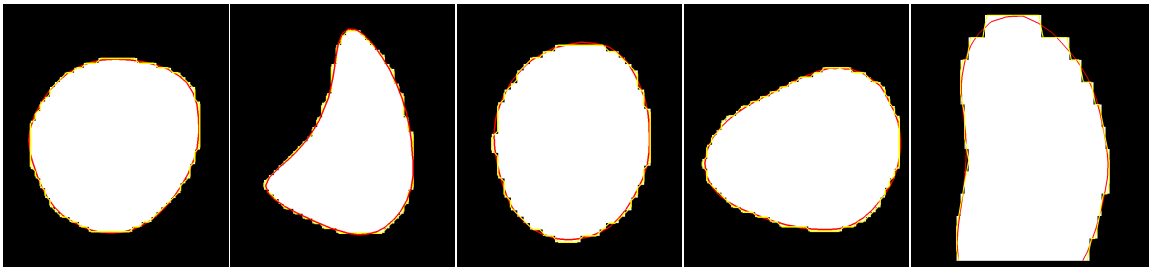

Figure 47. Contours of endocardial meshes generated by the marching cubes (yellow) and the proposed method (red) in short-axis sections for (a) left ventricle, (b) right ventricle, (c) left atrium, and (d) right atrium, and in a long-axis section for (e) left ventricle. The endocardial boundaries are defined by the blood pool segmentation shown in the binary images.

Table 8. The average in-slice distance (D) between the surface meshes generated by the marching cubes and the proposed method is given for each mesh. The in-plane resolution was 1.44 mm x 1.44 mm. The number of singularities (M), control points (K), and mesh vertices (V) used to generate the meshes with the proposed method are also reported.

	M	K	V	D [mm]
LV endocardium	227	204	1180	0.4 ±.07
RV endocardium	246	225	1220	0.3 ±.05
LA endocardium	62	66	748	0.5 ±.06
RA endocardium	57	58	684	0.4 ±.05
Myocardium epicardium	422	406	2472	0.3 ±.05

4.4 Discussion

The presented method can be used for the surface mesh generation of any object that is topologically equivalent to a sphere. While the method can be extended to control the triangle size based on the surface curvature, there is no need for such an approach in the case of myocardial wall surfaces since they are not highly curved. The method, unlike other mesh generation methods, allows for a direct control of the number of triangles and vertices in the mesh, which is particularly useful in modeling (e.g. FEM) applications.

Figs. 40 and 41 show that the method converges as the number of singularities or number of control points is increased, which is a desirable behavior. It means that beyond certain number of singularities and control points the method behaves the same. By comparing Figs. 40 and 41 one can see that the two parameters have very similar behavior, and this is why we used similar values for the two parameters (Table 8) when we compared our method to the marching cubes (Section 4.3.3). The two parameters have the same effect: they control the smoothness of the underlying continuous surface. The higher their values the smoother the surface, and the lower their values the better the surface fits the boundary points. For these reasons, one can use the same value for the two parameters and treat them as one parameter.

While the number of singularities and number of control points control the smoothness of the underlying implicit continuous surface, the number of mesh vertices affects the triangulation of the continuous surface. From Fig. 42 one can see that the method converges as the number of vertices is increased, which is a desirable behavior.

The reason why the graphs in Figs. 40, 41 and 42 do not exactly go to zero are the numerical errors in the implementation of the method resulting in sub-millimeter differences in the final location of the mesh vertices. We use a continuous and exact solution of the Laplace equation, since an approximate solution would increase the numerical errors.

The constant and relatively high value of the triangle quality index in Fig. 43 shows that the mesh has close-to-regular triangles for a range of numbers of vertices. The same conclusion can be made from Fig. 44.

The proposed method generates meshes that are very close to the ones obtained by the marching cubes (Fig. 47). While the differences in the short axis planes between the meshes generated by the two methods were sub-millimeter (Table 8), the meshes generated by the proposed method had about five times fewer triangles than the corresponding meshes generated by the marching cubes. However, unlike the meshes generated by the marching cubes (Fig. 38), the meshes generated by the proposed method (Figs. 45 and 46) are smooth and have close-to-regular triangles.

The proposed method can be used with segmented images that have anisotropic voxels. The segmentation boundary points are not strictly interpolated. Instead, they are approximated with an implicit surface that fits them in the least square sense. The surface smoothness vs. the goodness of fit is controlled by the number of singularities and number of control points, which can take the same value. If the implicit surface is smooth then the resulting mesh is also smooth. Thus, there is no need for artificial smoothing of the mesh that may shrink or affect the mesh in some other undesired way.

The entire method has been designed to completely avoid numerical optimization and consequently the problem of local extrema.

In the proposed method the segmentation boundary points are approximated with an implicit surface, which is then triangulated by propagating a regular mesh from a sphere to the surface. There are other ways to construct continuous surfaces that interpolate or approximate a given set of points (e.g. [76]). However, our representation allows for an exact continuous solution of the Laplace equation, while other surface models would require a numerical solution, which in turn would increase the mesh propagation error. Instead of propagating a regular mesh from the sphere to the surface, one can use a method for direct

triangulation of implicit surfaces (e.g. [77, 78, 79]). These methods are more general than our method since they can deal with an arbitrary topology. They march triangles over the surface and use heuristics to close the triangulation. Unlike these method, the proposed method, while restricted only to spherical topology, does not need a heuristics to close the triangulation and it can generate meshes with a pre-specified number of triangles.

We note that harmonic functions have already been used to represent shapes [80] and that there are other ways to map a sphere to the surface or vice versa (e.g. [81]).

CHAPTER 5

VELOCITY INTERPOLATION USING A DIVERGENCE FREE INTERPOLATION MODEL

5.1 Motivation

5.1.1 Relation between the volume ratio and the velocity field

Let us consider a continuum body $\mathcal{B}$, which is embedded in the three-dimensional Euclidean space at a given instant of time t. A right-handed orthonormal coordinate system with a fixed origin $\mathcal{O}$ is used. Region Ω_0 with the position of a point X corresponds to a fixed reference time. This region is referred to as the fixed reference configuration of the body of interest $\mathcal{B}$. I assume that the initial configuration coincides with the reference configuration, hence the reference time is at $t = 0$. The point X has the position of a particle occupied by $P \in \mathcal{B}$ at $t = 0$. P can be identified by the position vector $\mathbf{X}$ of point X relative to the fixed origin $\mathcal{O}$.

Now, the region Ω_0 moves to a new region Ω which is occupied by the body $\mathcal{B}$ at a subsequent time $t > 0$. The configuration of $\mathcal{B}$ at t is called current configuration. The point X of the reference configuration corresponds to the point x in the current configuration. The position vector $\mathbf{x}$ serves as a label for the point x with respect to the fixed origin $\mathcal{O}$. The components of the vector X along the introduced axes are labeled as the material or referential coordinates of the point X, and the components of the vector x along the introduced axes are labeled as the spatial or current coordinates of the point x.

In the following, all the operators or variables written with capital letters refer to the material coordinates and those with small letters to the spatial coordinates.

In 2.1.5, I introduced the deformation gradient, F, which characterizes the behavior of motion in the neighborhood of a point. The expression of F is the following:

$$\mathbf{F}(\mathbf{X}, t) = Grad\,(\mathbf{x}(\mathbf{X}, t)) \tag{5.1}$$

F is the Jacobian of the transformation applied to $\mathcal{B}$ between the reference and the current configuration. The determinant of F is known as the volume ratio or Jacobian determinant and it is denoted as:

$$J(\mathbf{X}, t) = det\,(\mathbf{F}(\mathbf{X}, t)) \tag{5.2}$$

The change in volume between the reference and the current configurations is:

$$dv = J(\mathbf{X}, t)dV \tag{5.3}$$

where dV and dv denote infinitesimal volume elements defined in the reference and current configuration respectively. For real material, the deformation gradient is invertible, which means $J \neq 0$.

Referring to the equation (1.239) in [82]:

$$d\phi = \frac{\partial \phi(\mathbf{A})}{\partial \mathbf{A}} : d\mathbf{A} = tr\left(\left(\frac{\partial \phi(\mathbf{A})}{\partial \mathbf{A}}\right)^T d\mathbf{A}\right), \tag{5.4}$$

where $d\phi$ denotes the total differential of the scalar-valued function $\phi(\mathbf{A})$ of one second-order tensor variable $\mathbf{A}$, and : represents the double contraction of two tensors. Using the chain rule and Eq. 5.4, the material time derivative of the volume ratio can be derived:

$$\dot{J} = \frac{\partial J}{\partial \mathbf{F}} : \dot{\mathbf{F}} = tr\left(\left(\frac{\partial J}{\partial \mathbf{F}}\right)^T \dot{\mathbf{F}}\right), \tag{5.5}$$

where $\dot{J}$ and $\dot{\mathbf{F}}$ are the material time derivative of the volume ratio and deformation gradient respectively. By substituting $\mathbf{F}$ as the tensor in the equation (1.241) in [82], one obtains:

$$\frac{\partial det(\mathbf{F})}{\partial \mathbf{F}} = det(\mathbf{F})\mathbf{F}^{-T} \tag{5.6}$$

By combining Eq. 5.5 and Eq. 5.6, one can derive:

$$\dot{J} = J\mathbf{F}^{-T} : \dot{\mathbf{F}} \tag{5.7}$$

Now, referring to the equation (2.141) in [82]:

$$grad(\mathbf{v}) = \dot{\mathbf{F}}\mathbf{F}^{-1}, \tag{5.8}$$

where $\mathbf{v}$ denotes the spatial description of the velocity field. Thus, using Eq. 5.7 and Eq. 5.8 , it follows:

$$\begin{aligned}
\dot{J} &= J\mathbf{F}^{-T} : \dot{\mathbf{F}} \\
&= J\mathbf{F}^{-T} : grad(\mathbf{v})\mathbf{F} \\
&= J\mathbf{F}^{-T}\mathbf{F}^T : grad(\mathbf{v}) \\
&= J\mathbf{I} : grad(\mathbf{v}) \\
&= Jtr\left(grad(\mathbf{v})\right) \\
&= Jdiv(\mathbf{v}),
\end{aligned} \tag{5.9}$$

where $\mathbf{I}$ is the identity tensor. The last equation links the volume ratio to the velocity field. Let us write it in the following way:

$$\dot{J} = J\nabla \cdot \mathbf{v}, \tag{5.10}$$

5.1.2 Cardiac Deformation Recovery from phase velocity MRI

A continuum body is said to be incompressible if every motion it undergoes is isochoric, which means dv is constant. So for an incompressible body, Eq. 5.3 leads to:

$$J = 1 \tag{5.11}$$

As $J = 1$ for incompressible materials, Eq. 5.10 leads to:

$$\nabla \cdot \mathbf{v} = 0 \tag{5.12}$$

Thus, a continuum body is incompressible if $\nabla \cdot \mathbf{v} = 0$.

Velocity interpolation using a divergence free model can be used for cardiac deformation recovery form phase velocity MRI. The idea is to interpolate the velocity vector field in each frame of a phase velocity MR sequence. The divergence free interpolation will provide a continuous velocity vector field that is divergence free, which means that the corresponding deformation is incompressible, a desirable property since the myocardium has been shown to be close to incompressible (section 1.4). Then, it remains to integrate the velocity vector field to obtain the displacement field of the myocardium throughout the cardiac cycle.

5.2 Methods

The goal is to interpolate a velocity vector field over a domain of arbitrary topology. First, nodes are automatically distributed in a form of a uniform grid that covers entirely the domain. Only the nodes located inside the domain are selected. The velocity field is interpolated at the nodes using the divergence-free matrix-valued radial basis function scheme introduced in section 3.1.1 defined by:

$$\mathbf{v}(\mathbf{r}) = \sum_{j=1}^{M} \mathbf{\Phi}(\mathbf{r} - \mathbf{n}_j)\mathbf{c}_j, \tag{5.13}$$

where $\mathbf{r}$ is the point where the interpolation is evaluated, $\mathbf{n}_j$ are the M nodes where the velocity field is interpolated, and $\mathbf{c}_j$ the corresponding coefficients. Then, the coefficients

$\mathbf{c}_j$ are computed such that the interpolated velocity field fits the data on the least squares sense. This corresponds to solving the system:

$$\underbrace{\begin{bmatrix} \mathbf{\Phi}(\mathbf{r}_1-\mathbf{n}_1)\ \mathbf{\Phi}(\mathbf{r}_1-\mathbf{n}_2)...\mathbf{\Phi}(\mathbf{r}_1-\mathbf{n}_M) \\ \mathbf{\Phi}(\mathbf{r}_2-\mathbf{n}_1)\ \mathbf{\Phi}(\mathbf{r}_2-\mathbf{n}_2)...\mathbf{\Phi}(\mathbf{r}_2-\mathbf{n}_M) \\ . \\ . \\ . \\ \mathbf{\Phi}(\mathbf{r}_N-\mathbf{n}_1)\mathbf{\Phi}(\mathbf{r}_N-\mathbf{n}_2)...\mathbf{\Phi}(\mathbf{r}_N-\mathbf{n}_M) \end{bmatrix}}_{G} \underbrace{\begin{bmatrix} \mathbf{c}_1 \\ \mathbf{c}_2 \\ . \\ . \\ . \\ \mathbf{c}_M \end{bmatrix}}_{p} = \underbrace{\begin{bmatrix} \mathbf{v}(\mathbf{r_1}) \\ \mathbf{v}(\mathbf{r_2}) \\ . \\ . \\ . \\ \mathbf{v}(\mathbf{r_N}) \end{bmatrix}}_{h}, \tag{5.14}$$

where $\mathbf{r}_i$ are the N data location used for the least squares sense fitting and $\mathbf{v}(\mathbf{r_i})$ the corresponding measured velocity vectors.

The corresponding least squares solution is:

$$p = (G^T G)^{-1} G^T h, \tag{5.15}$$

which defines the divergence free interpolation of the velocity vector field over the domain. Two quantitative measures are used to evaluate the performance of the interpolation. The first one is to compute the difference in magnitude between the measured velocity vectors (data) and the interpolated vector field. The second measure is to compute the angle between the two. The smaller these two measures are, the more accurate the interpolation is.

5.3 Results

5.3.1 Simulated Data

Before applying the divergence free interpolation on real cases, I used simulated data to test the method. A cube centered at the origin with edge length of 2 mm is used as the region of interest. Nodes and velocity measurements are uniformly distributed as 4x4x4 and 22x22x22 grids, respectively, as seen in Fig. 48. Three different divergence free vector fields are used to simulate the velocity vector field of the myocardium:

$$\mathbf{v}_1(x,y,z) = 0.3 \begin{pmatrix} -zy \\ zx \\ 1 \end{pmatrix} \tag{5.16}$$

$$\mathbf{v}_2(x,y,z) = \begin{pmatrix} 0.3y^2 \\ 0.3(1-x^2)(y-1)+x \\ -z(1-x^2) \end{pmatrix} \tag{5.17}$$

$$\mathbf{v}_3(x,y,z) = 0.3 \begin{pmatrix} xsin(z) \\ x \\ cos(z) \end{pmatrix} \tag{5.18}$$

Fig. 48 displays both the vector fields (data) and the corresponding interpolated vector fields. Figs. 49 and 50 show the histograms of the difference in magnitude and the angle between the data and the interpolated vector field. Tables 9 and 10 show the mean of the differences in magnitude and of the angles between the original vector fields and the corresponding interpolated ones.

5.3.2 Real Data

For real case applications, I used the data of the healthy volunteer of the section 3.2.2.1. I tested the divergence free interpolation on the measured velocity vectors provided by the phase velocity MRI scan. Like in section 3.2.2.1, the scan was performed on a 1.5 T clinical MRI scanner (Intera, Philips Medical Systems, Best, The Netherlands). A segmented, navigator-echo and ECG-gated phase-contrast sequence was used to acquire velocity. Velocities were encoded in an interleaved fashion with reference and velocity-encoded scans acquired in successive cardiac cycles. In-place resolution was 1.4 mm, slice thickness was 8 mm and a velocity-encoding value of 30 cm/second was used to encode through-plane velocities of the myocardial tissue. The scan had 15 contiguous short axis slices and seven phases for each slice were obtained during the cardiac cycle.

The anatomical sequence acquired with the phase velocity ones allowed for manual segmentation of the left ventricle, which defined the region of interest where the divergence free interpolation was performed. Fig. 51 displays both the measured velocity vectors (data) and the corresponding interpolated vector fields of the ED, mid systole (MS) and ES frames of the healthy volunteer. Figs. 52 and 53 show the histograms of the differences in magnitude and the angles between the data and the interpolated vector field for the three frames. Table 9 shows the mean of the differences in magnitude between the measured

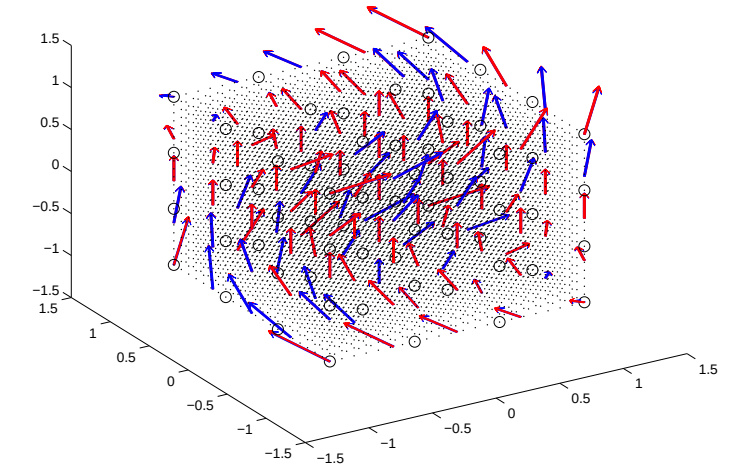

(a)

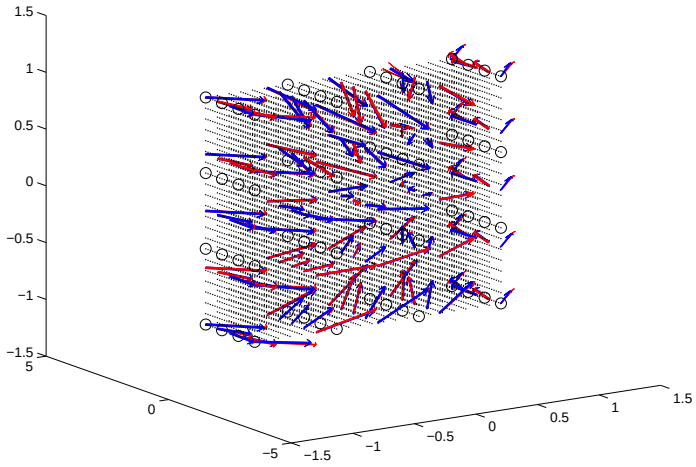

(b)

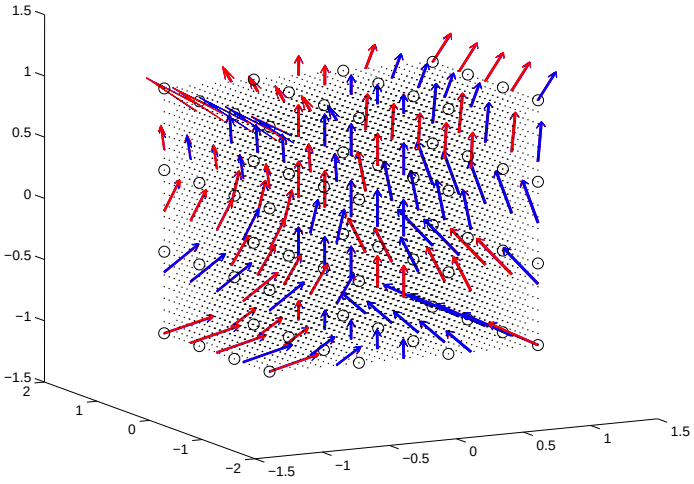

(c)

Figure 48. The original vector fields (data) are displayed in red and the corresponding interpolated ones using the divergence-free model in blue for (a) $\mathbf{v}_1$, (b) $\mathbf{v}_2$, and (c) $\mathbf{v}_3$. The black points are the locations of the measurements. The black circles are the locations of the nodes. The vector fields are shown at few measurements points for the clarity of the display.

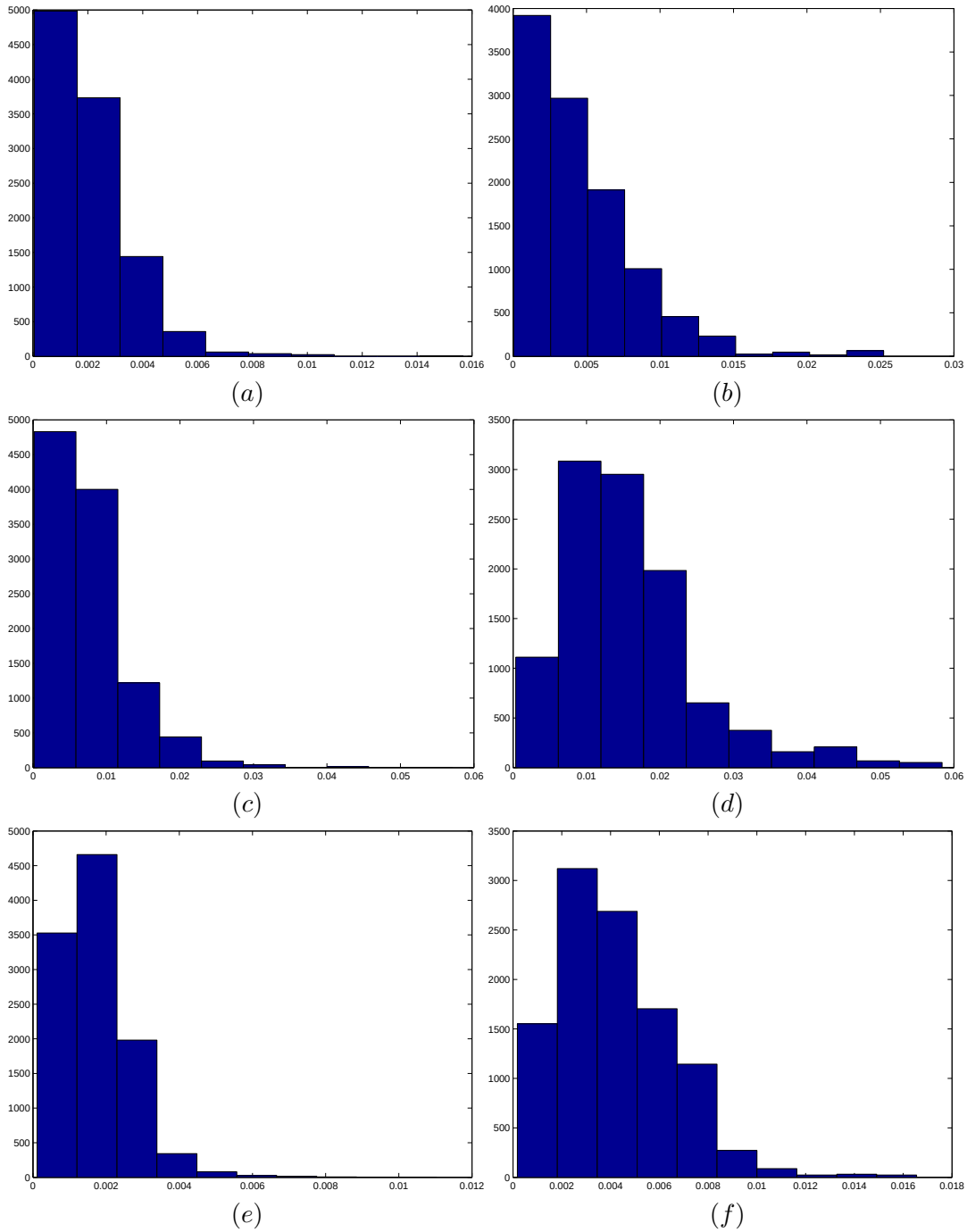

Figure 49. Histograms of the differences in magnitude (in cm/s) between the original vector fields and the corresponding interpolated ones using the divergence-free model for (a) $\mathbf{v}_1$, (c) $\mathbf{v}_2$, (e) $\mathbf{v}_3$ and using TPS for (b) $\mathbf{v}_1$, (d) $\mathbf{v}_2$, (f) $\mathbf{v}_3$.

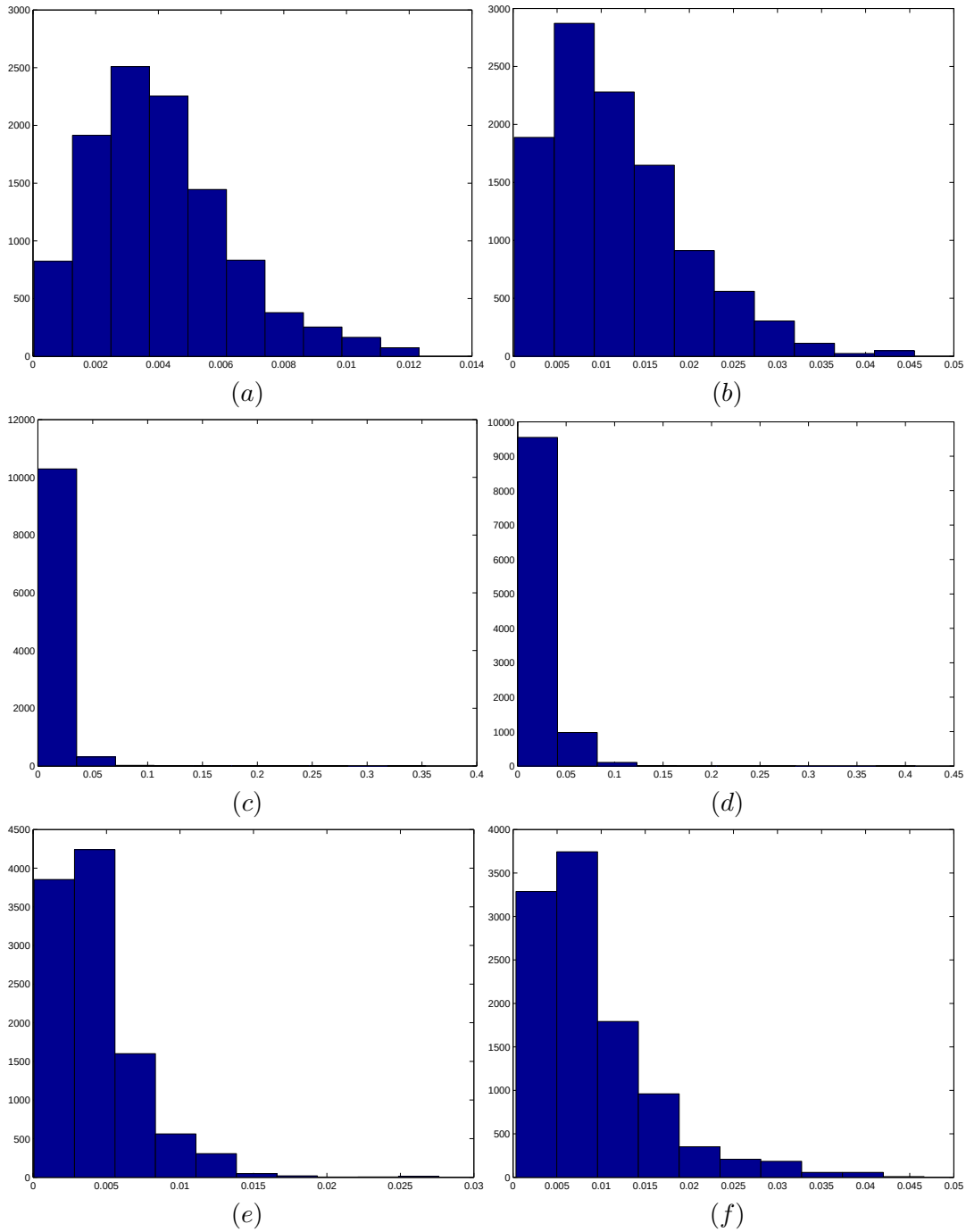

Figure 50. Histograms of the angles (in rad) between the original vector fields and the corresponding interpolated ones using the divergence-free model for (a) $\mathbf{v}_1$, (c) $\mathbf{v}_2$, (e) $\mathbf{v}_3$ and using TPS for (b) $\mathbf{v}_1$, (d) $\mathbf{v}_2$, (f) $\mathbf{v}_3$.

Table 9. Mean of the differences in magnitude between the original vector fields and the corresponding interpolated ones using the divergence-free model using the divergence-free model and TPS for the simulated and the real cases.

Mean of the magnitude errors [cm/s]	Divergence-free	TPS
simulated: $\mathbf{v}_1$	0.02 ± 0.01	0.04 ± 0.03
simulated: $\mathbf{v}_2$	0.007 ± 0.005	0.01 ± 0.009
simulated: $\mathbf{v}_3$	0.001 ± 0.0009	0.004 ± 0.002
healthy volunteer: ED frame	0.45 ± 0.30	0.59 ± 0.55
healthy volunteer: MS frame	0.44 ± 0.33	0.58 ± 0.47
healthy volunteer: ES frame	0.39 ± 0.28	0.53 ± 0.46

Table 10. Mean of the angles between the original vector fields and the corresponding interpolated ones using the divergence-free model using the divergence-free model and TPS for the simulated and the real cases.

Mean of the angle errors [rad]	Divergence-free	TPS
simulated: $\mathbf{v}_1$	0.004 ± 0.002	0.01 ± 0.007
simulated: $\mathbf{v}_2$	0.01 ± 0.009	0.02 ± 0.04
simulated: $\mathbf{v}_3$	0.004 ± 0.002	0.009 ± 0.007
healthy volunteer: ED frame	0.05 ± 0.04	0.06 ± 0.08
healthy volunteer: MS frame	0.05 ± 0.04	0.06 ± 0.08
healthy volunteer: ES frame	0.04 ± 0.03	0.05 ± 0.06

velocity vectors and the corresponding interpolated ones and Table 10 shows the mean of the angles in magnitude between the measured velocity vectors and the corresponding interpolated ones.

5.3.3 Comparison to Thin-Plate Spline

I compared the interpolation provided by the divergence-free scheme with the one given by TPS on the simulated data and the real data. Fig. 49 shows the histograms of the differences in magnitude between the data and the interpolated vector field for the three simulated vector fields and Fig. 52 for the three frames of the phase velocity MRI scan of the healthy volunteer. Fig. 50 shows the histograms of the angles between the data and the interpolated vector field for the three simulated vector fields and Fig. 53 for the three frames of the phase velocity MRI scan of the healthy volunteer. Table 9 shows the mean of the differences in magnitude between the original vector fields and the corresponding interpolated ones for all the cases and Table 10 shows the mean of the angles in magnitude

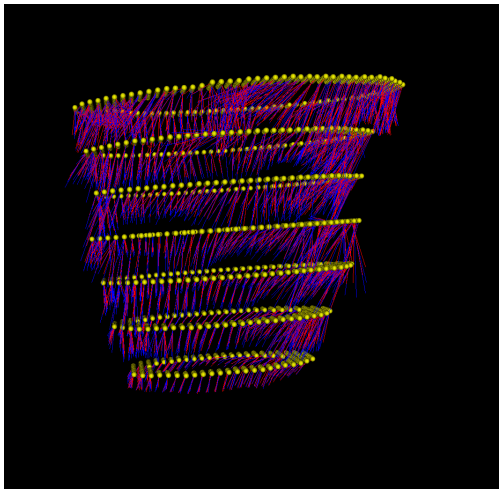

(a)

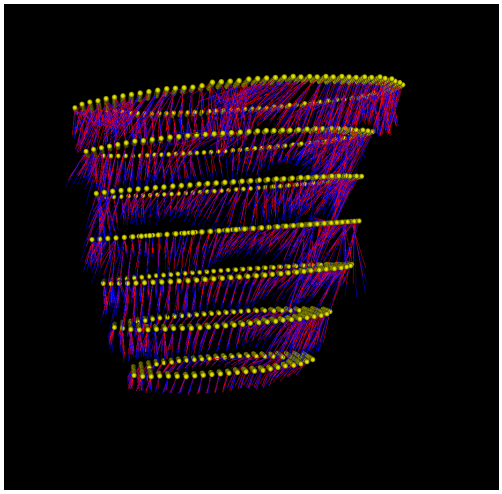

(b)

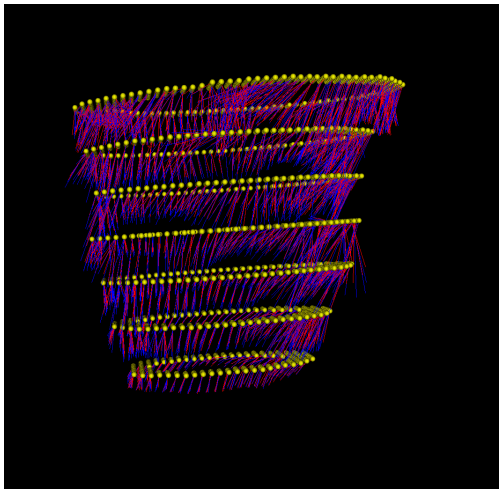

(c)

Figure 51. The measured velocity vectors (data) are displayed in red and the corresponding interpolated ones using the divergence-free model in blue for (a) ED, (b) MS, and (c) ES of a healthy volunteer. The yellow points are the centers of voxels from the myocardium.

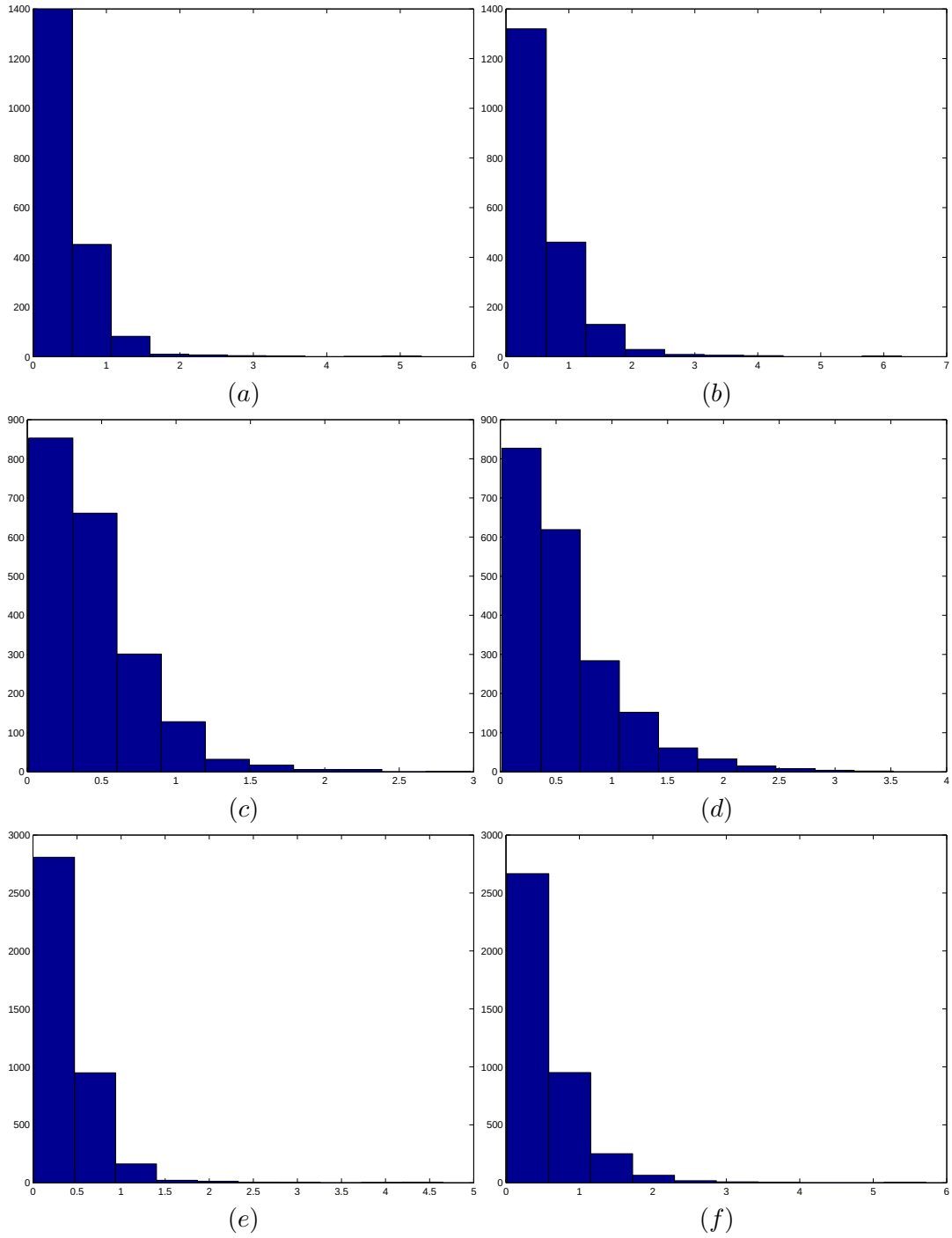

Figure 52. Histograms of the differences in magnitude (in cm/s) between the measured velocity vectors and the corresponding interpolated ones using the divergence-free model for (a) ED, (c) MS, and (e) ES of a healthy volunteer and using TPS for (b) ED, (d) MS, and (f) ES of the same sequence.

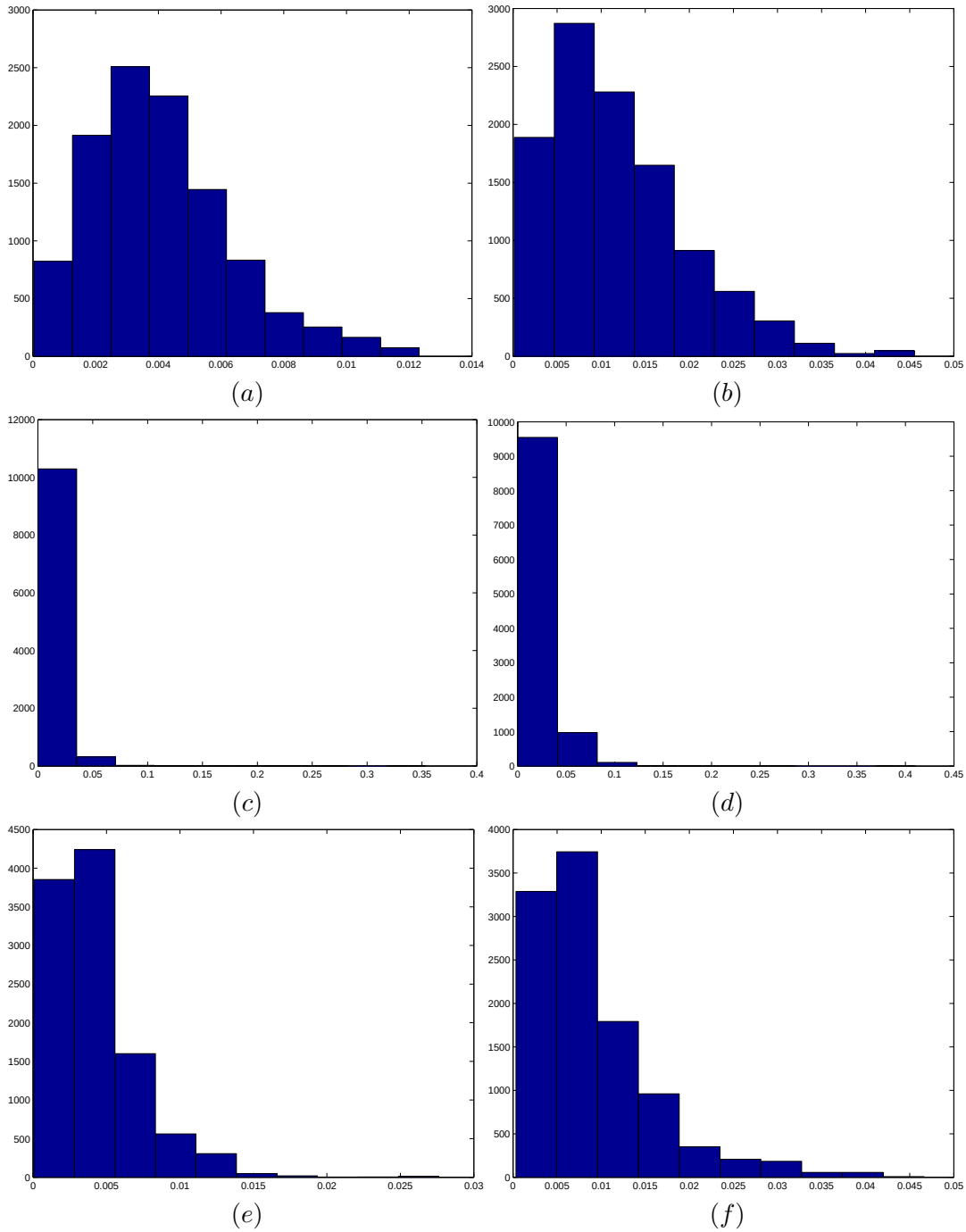

Figure 53. Histograms of the angles (in rad) between the measured velocity vectors and the corresponding interpolated ones using the divergence-free model for (a) ED, (c) MS, and (e) ES of a healthy volunteer and using TPS for (b) ED, (d) MS, and (f) ES of the same sequence.

between the original vector fields and the corresponding interpolated ones for all the cases.

5.4 Discussion

Figs. 51, 49, and 50 show that the divergence free interpolation is able to provide a vector field that is close to the simulated ones. Figs. 51, 52, and 53 show that it is also the case for the frames of a phase velocity MRI scan of the LV of a human subject.. The advantage of using the divergence free interpolation model for modeling the velocity filed of the myocardium is twofold: first, it provides a continuous vector field over the entire myocardium; second, it generates a divergence free vector field, which means that the corresponding deformation is incompressible, a desirable property since the myocardium has been shown to be close to incompressible (section 1.4).

Figs 49, 50, 52, and 53 show that TPS interpolation also provides a reasonable interpolation of the simulated and real data. However, Tables 9 and 10 show that the differences in magnitude and the angles between the original vector fields and the corresponding interpolated ones are larger for TPS than for the divergence free model. Furthermore, the difference in performance between the two interpolation schemes is more pronounced in the case of simulated data because the original field are divergence free by construction. For the real data, the velocity vector field is affected by the noise due to the acquisition and by slice misalignment. This can explain why the difference in performance between the TPS and the divergence free interpolation is smaller than for the simulated data.

CHAPTER 6
CONCLUSION

I presented in this thesis two methods for cardiac deformation recovery from cine MRI. In chapter 2, I developed an automated method for the recovery of the LV wall based on a 3D deformable model that is exactly incompressible. Since this method is not suitable for the recovery of the biventricular wall, I introduced in chapter 3 an automated method for cardiac deformation recovery based on a 3D nearly incompressible deformable model that can model the motion of structures with arbitrary topologies. One can use the same model to represent the motion of the four cardiac chambers or any other topology.

The main contribution of my work is that the proposed methods are guaranteed to generate exactly or nearly incompressible deformations. This is a desirable property since the myocardium has been shown to be close to incompressible. The myocardium needs to be segmented in an initial frame after which the methods automatically determine the tissue deformation everywhere in the myocardium throughout the cardiac cycle. From the recovered deformation, one can directly compute a number of clinically useful parameters, including strains. We tested the methods on three normal subjects and three ventricular dyssynchrony patients. When the anatomical MR scan is acquired in short axis slices with pronounced voxel anisotropy in the out-of-plane direction, the longitudinal motion parameters are less reliable than the radial and circumferential ones. Despite this disparity, the recovered normal strains obtained from both models were similar for different normal subjects and similar to those reported by other researchers for normal subjects. Furthermore, the methods could clearly distinguish normal subjects from patients with ventricular dyssynchrony. Strains and displacements of the three patients were clearly smaller than those of the three normals indicating reduced cardiac function. The proposed methods were also applied to repeated scans of the same normal subject. It yielded very similar deformation recovery results. The proposed methods could be used to recover cardiac deformation from other imaging modalities, e.g. tagged cine MRI or cardiac cine CT, instead of anatomical cine MRI.

A method to generate a smooth and accurate surface of the myocardium is needed to

illustrate the cardiac deformation recovery. Thus, I presented in chapter 4 a novel technique for the construction of endocardial and epicardial surfaces from 3D segmented cardiac MR images. The same algorithm is applied independently to each heart chamber. A surface mesh is first constructed on a sphere that includes the cardiac chamber. Then, the mesh vertices are propagated along the gradient of a potential that satisfies the Laplace equation. The resulting surface meshes are smooth despite the strong voxel anisotropy. Furthermore, the presented method generates regular mesh triangles and allows for a complete control of the number of triangles. For the five tested cases, the average distance between the surfaces generated by our method and by the marching cubes was 0.4 mm.

Finally, I presented a method to interpolate the velocity vector field in a phase velocity MRI sequence. The method uses the divergence free interpolation model presented in the biventricular deformation recovery. The divergence free interpolation provides a continuous velocity vector field that is divergence free, which means that the corresponding deformation is incompressible, a desirable property since the myocardium has been shown to be close to incompressible. The method has been tested on three simulated cases and three real cases. The interpolation obtained is close to the original vector field in terms of difference in magnitude and angle. Furthermore, it is more accurate than the interpolation given by thin-plate spline because of its divergence free property. The proposed method will be used in a future work to recover the cardiac deformation from phase velocity MRI, which is an acquisition technique that encodes directly the velocity of the myocardium and thus may provide more reliable information about the myocardial motion than cine MRI.

APPENDIX A

PSEUDO THIN PLATE SPLINE INTERPOLATION ON THE SPHERE

This section summarizes the pseudo thin plate spline interpolation on the sphere [75]. The smoothest interpolator of arbitrarily located data points is commonly referred to as thin plate splines and its closed form expression has been obtained for the d-dimensional Euclidean space [83]. However, the closed form expression for the smoothest interpolator of arbitrarily located data points on the sphere does not exist [75]. An approximation of the smoothest interpolator is referred to as pseudo thin plate splines. Wahba [75] proposed a class of pseudo thin plate splines on the sphere and provided the corresponding closed form expressions.

Let $\mathbb{R}$ represent the set of real numbers and let

$$\mathbf{S} = \left\{ \hat{\mathbf{u}} | \hat{\mathbf{u}} \in \mathbb{R}^3 \text{ and } ||\hat{\mathbf{u}}|| = 1 \right\} \tag{A.1}$$

represent the unit sphere, i.e. the set of all unit vectors. Let $\hat{\mathbf{u}}_i \in \mathbf{S}$ represent points on the unit sphere and $v_i \in \mathbb{R}$ the corresponding values for $i = 1, \ldots, N$. The goal is to find the smoothest function $f : \mathbf{S} \mapsto \mathbb{R}$ that interpolates the data points $(\hat{\mathbf{u}}_i, v_i)$. The pseudo thin plate splines interpolator proposed by Wahba [75] has the following form

$$f(\hat{\mathbf{u}}) = \alpha_0 + \sum_{i=1}^{N} \alpha_i \psi(\hat{\mathbf{u}} \cdot \hat{\mathbf{u}}_i), \tag{A.2}$$

where the function $\psi : [-1, 1] \mapsto \mathbb{R}$ defines the type of the pseudo thin plate splines, α_0 is the coefficient of the constant term and $\alpha_i,\ 1 \leq i \leq N$ is the coefficient corresponding to the data point $(\hat{\mathbf{u}}_i, v_i)$. We used ψ for the case of $m = 4$ in [75], i.e.

$$\psi(x) = \frac{1}{2\pi} \left[\frac{1}{6!} q(x) - \frac{1}{7!} \right], \tag{A.3}$$

where

$$q(x) = \begin{cases} a + b + c & -1 \leq x < 1, \\ \frac{1}{6} & x = 1, \end{cases} \tag{A.4}$$

$$a = \left(924w^6 - 1260w^5 + 420w^4 - 20w^3\right) \ln\left(1 + \frac{1}{\sqrt{w}}\right), \tag{A.5}$$

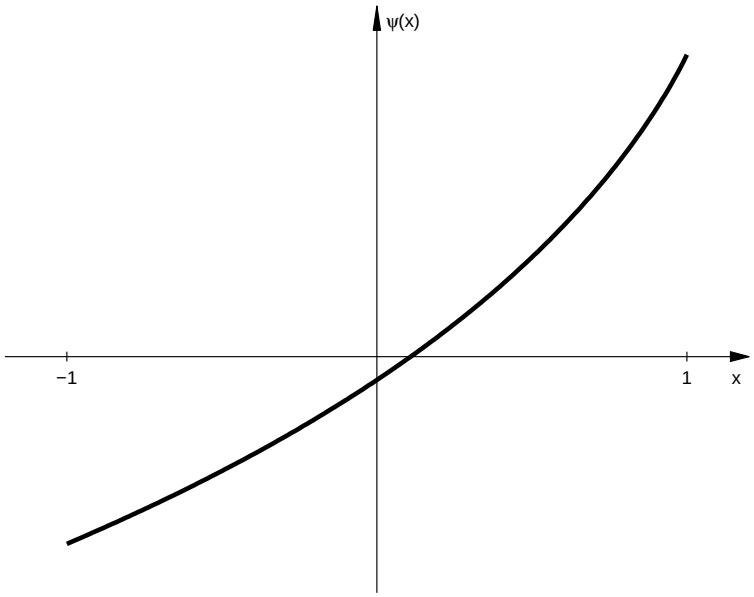

Figure 54. The graph of $\psi(x)$ given by Eqs. A.3-A.8 shows that the function monotonically increases from negative values for $x = -1$ to positive values for $x = 1$. The scale of the y-axis is irrelevant.

$$b = \left(-924w^5 + 952w^4 - \frac{924}{5}w^3\right)\sqrt{w}, \tag{A.6}$$

$$c = 462w^5 - 399w^4 + 49w^3 + \frac{1}{2}w^2 - \frac{1}{10}w + \frac{1}{6}, \tag{A.7}$$

and

$$w = \frac{1-x}{2}. \tag{A.8}$$

Fig. 54 shows the graph of ψ. It should be noted that $\hat{\mathbf{u}} \cdot \hat{\mathbf{u}}_i$, which is the argument of ψ in Eq. A.2, takes values from -1, when $\hat{\mathbf{u}}$ and $\hat{\mathbf{u}}_i$ point in opposite directions, to 1, when $\hat{\mathbf{u}}$ and $\hat{\mathbf{u}}_i$ coincide. Thus, ψ provides more weight to the coefficients α_i of those points $\hat{\mathbf{u}}_i$ that are close to the point of interpolation $\hat{\mathbf{u}}$, and less or negative weight to the coefficients of the points further away.

The coefficients $\alpha_0, \alpha_1, \ldots, \alpha_N$ can be computed from the requirement that $f(\hat{\mathbf{u}})$ interpolates the data points and that the coefficients $\alpha_1, \ldots, \alpha_N$ sum to 0 [75]. This leads to a system of $N + 1$ linear equations

$$f(\hat{\mathbf{u}}_i) = v_i, \quad i = 1, \ldots, N, \tag{A.9}$$

$$\sum_{i=1}^{N} \alpha_i = 0, \tag{A.10}$$

that can be solved for the $N+1$ unknown coefficients $\alpha_0, \alpha_1, \ldots, \alpha_N$ given N data points $(\hat{\mathbf{u}}_i, v_i)$. The resulting function $f(\hat{\mathbf{u}})$ is a smooth interpolator of the data points on the sphere.

APPENDIX B
DERIVATION OF THE INCOMPRESSIBILITY EQUATION

Let the unit sphere (Eq. A.1) be parameterized with parameters α and β locally around a given unit vector. This means that $\hat{\mathbf{u}}$ is a function of α and β, i.e. one can write $\hat{\mathbf{u}}(\alpha, \beta)$ around that unit vector. For the purposes of this derivation, instead of using the curvilinear coordinates $(\hat{\mathbf{u}}, \gamma)$, we will use the curvilinear coordinates (α, β, γ). It turns out that the result of the derivation does not depend on the choice of the particular parametrization, i.e. one can use any parametrization or use different parameterizations for different local neighborhoods; the result will be the same.

The location of the point with curvilinear coordinates (α, β, γ) in the reference configuration is

$$\mathbf{r}(\alpha, \beta, \gamma) = \mathbf{m}(\alpha, \beta) + \gamma \hat{\mathbf{n}}(\alpha, \beta), \tag{B.1}$$

where $\mathbf{m}(\alpha, \beta)$ is a point on the midsurface and $\hat{\mathbf{n}}(\alpha, \beta)$ the corresponding midsurface unit normal. Thus, α and β represent a parametrization of the midsurface, too, and γ is the distance of the point from the midsurface. This equation corresponds to Eq. 2.4 for the case of $(\hat{\mathbf{u}}, \gamma)$ coordinates. Assuming "no transmural bending", the location of the point with curvilinear coordinates (α, β, γ) in the current configuration is

$$\mathbf{R}(\alpha, \beta, \gamma) = \mathbf{M}(\alpha, \beta) + \Gamma(\alpha, \beta, \gamma) \hat{\mathbf{N}}(\alpha, \beta), \tag{B.2}$$

where $\mathbf{M}(\alpha, \beta)$ is a point on the midsurface and $\hat{\mathbf{N}}(\alpha, \beta)$ the corresponding midsurface unit normal. Here, too, α and β represent a parametrization of the midsurface, whereas the distance of the point from the midsurface is $\Gamma(\alpha, \beta, \gamma)$. This equation corresponds to Eq. 2.7 for the case of $(\hat{\mathbf{u}}, \gamma)$ coordinates. Note that $\mathbf{r}(\alpha, \beta, \gamma)$ and $\mathbf{R}(\alpha, \beta, \gamma)$ depend on the same parameters, i.e. they represent corresponding points in the two configurations.

If the midsurface is defined in both the reference and current configuration, i.e. if functions $\mathbf{m}(\alpha, \beta)$, $\hat{\mathbf{n}}(\alpha, \beta)$, $\mathbf{M}(\alpha, \beta)$, and $\hat{\mathbf{N}}(\alpha, \beta)$ are known, then one can determine $\Gamma(\alpha, \beta, \gamma)$ such that the mapping from $\mathbf{r}(\alpha, \beta, \gamma)$ to $\mathbf{R}(\alpha, \beta, \gamma)$ is incompressible. To simplify the notation, the independent variables α, β, and γ will be dropped. Let dv represent the

infinitesimal volume defined by function $\mathbf{r}$ when α, β, and γ are varied by infinitesimal increments $d\alpha$, $d\beta$, and $d\gamma$, respectively. Similarly, let dV represent the infinitesimal volume defined by function $\mathbf{R}$ when α, β, and γ are varied by infinitesimal increments $d\alpha$, $d\beta$, and $d\gamma$, respectively. The transformation is incompressible, i.e. volume preserving, if

$$dv = dV \tag{B.3}$$

for any α, β, and γ. One can obtain dv by taking the triple scalar product of $\frac{\partial \mathbf{r}}{\partial \alpha} d\alpha$, $\frac{\partial \mathbf{r}}{\partial \beta} d\beta$, and $\frac{\partial \mathbf{r}}{\partial \gamma} d\gamma$, i.e.

$$dv = \frac{\partial \mathbf{r}}{\partial \gamma} \cdot \left(\frac{\partial \mathbf{r}}{\partial \alpha} \times \frac{\partial \mathbf{r}}{\partial \beta} \right) d\alpha d\beta d\gamma. \tag{B.4}$$

From Eq. B.1, it follows that

$$\begin{aligned} dv = \hat{\mathbf{n}} \cdot \Bigg[& \left(\frac{\partial \mathbf{m}}{\partial \alpha} \times \frac{\partial \mathbf{m}}{\partial \beta} \right) + \gamma \left(\frac{\partial \mathbf{m}}{\partial \alpha} \times \frac{\partial \hat{\mathbf{n}}}{\partial \beta} + \frac{\partial \mathbf{m}}{\partial \beta} \times \frac{\partial \hat{\mathbf{n}}}{\partial \alpha} \right) \\ & + \gamma^2 \left(\frac{\partial \hat{\mathbf{n}}}{\partial \alpha} \times \frac{\partial \hat{\mathbf{n}}}{\partial \beta} \right) \Bigg] d\alpha d\beta d\gamma. \end{aligned} \tag{B.5}$$

Assuming that $\frac{\partial \mathbf{m}}{\partial \alpha}$ and $\frac{\partial \mathbf{m}}{\partial \beta}$ are in the principal directions, then $\frac{\partial \hat{\mathbf{n}}}{\partial \alpha} = -\kappa_1 \frac{\partial \mathbf{m}}{\partial \alpha}$ and $\frac{\partial \hat{\mathbf{n}}}{\partial \beta} = -\kappa_2 \frac{\partial \mathbf{m}}{\partial \beta}$, where κ_1 and κ_2 are the two principal curvatures of the midsurface. The expression for the infinitesimal volume reduces to

$$dv = a \left(1 - 2h\gamma + k\gamma^2 \right) d\alpha d\beta d\gamma, \tag{B.6}$$

where $a = |\frac{\partial \mathbf{m}}{\partial \alpha} \times \frac{\partial \mathbf{m}}{\partial \beta}|$, and $h = \frac{\kappa_1 + \kappa_2}{2}$ and $k = \kappa_1 \kappa_2$ are the mean and Gaussian curvatures, respectively, of the midsurface in the reference configuration. This expression holds for any parametrization since $a d\alpha d\beta d\gamma$, h, and k are independent of the parametrization [84]. It is assumed that the surface normals are oriented outward. Similarly,

$$dV = \frac{\partial \mathbf{R}}{\partial \gamma} \cdot \left(\frac{\partial \mathbf{R}}{\partial \alpha} \times \frac{\partial \mathbf{R}}{\partial \beta} \right) d\alpha d\beta d\gamma. \tag{B.7}$$

From Eq. B.2, it follows that

$$\begin{aligned} dV = \hat{\mathbf{N}} \cdot \Bigg[& \left(\frac{\partial \mathbf{M}}{\partial \alpha} \times \frac{\partial \mathbf{M}}{\partial \beta} \right) + \Gamma \left(\frac{\partial \mathbf{M}}{\partial \alpha} \times \frac{\partial \hat{\mathbf{N}}}{\partial \beta} \right. \\ & \left. + \frac{\partial \mathbf{M}}{\partial \beta} \times \frac{\partial \hat{\mathbf{N}}}{\partial \alpha} \right) + \Gamma^2 \left(\frac{\partial \hat{\mathbf{N}}}{\partial \alpha} \times \frac{\partial \hat{\mathbf{N}}}{\partial \beta} \right) \Bigg] \frac{\partial \Gamma}{\partial \gamma} d\alpha d\beta d\gamma. \end{aligned} \tag{B.8}$$

This expression simplifies to

$$dV = A \left(1 - 2H\Gamma + K\Gamma^2 \right) \frac{\partial \Gamma}{\partial \gamma} d\alpha d\beta d\gamma, \tag{B.9}$$

where $A = |\frac{\partial \mathbf{M}}{\partial \alpha} \times \frac{\partial \mathbf{M}}{\partial \beta}|$, and H and K are the mean and Gaussian curvatures, respectively, of the midsurface in the current configuration. By combining Eqs. B.3, B.6, and B.9, one obtains the following differential equation

$$1 - 2h\gamma + k\gamma^2 = S\left(1 - 2H\Gamma + K\Gamma^2\right)\frac{\partial \Gamma}{\partial \gamma}, \tag{B.10}$$

where $S = \frac{A}{a}$ is the surface Jacobian, which measures the relative change of the local midsurface area. After integration, the differential equation becomes a cubic equation in Γ,

$$\gamma - h\gamma^2 + \frac{1}{3}k\gamma^3 + C = S\left(\Gamma - H\Gamma + \frac{1}{3}K\Gamma^3\right), \tag{B.11}$$

where C depends on α and β but not on γ. The transformation needs to map points on the midsurface in the reference configuration ($\gamma = 0$) to points on the midsurface in the current configuration ($\Gamma = 0$), which implies that $C = 0$, and the cubic equation reduces to Eq. 2.8. This equation does not depend on the parametrization of the sphere since h, k, S, H, and K are functions of $\hat{\mathbf{u}}$ only, i.e. they depend on the location on the surface and the shape of the surface and not on the choice of the particular parametrization.

APPENDIX C

HARMONIC FUNCTION WITH A SPHERICAL ISOLEVEL AND SINGLE SINGULARITY

This section describes the solution to the Laplace equation over a spherical domain that has a single singularity somewhere within the domain and that is equal to a constant on the boundary of the domain. Let the sphere center be the coordinate system origin, R denote the radius of the sphere, $\mathbf{s}$ the location of the singularity, and $\mathbf{r}$ the independent variable. The solution $f_{\mathbf{s}}(\mathbf{r})$ needs to satisfy the following

$$\lim_{\mathbf{r}\to\mathbf{s}} f_{\mathbf{s}}(\mathbf{r}) = \infty, \tag{C.1}$$

$$f_{\mathbf{s}}(\mathbf{r})\big|_{|\mathbf{r}|=R} = 0, \tag{C.2}$$

$$\Delta f_{\mathbf{s}} = 0. \tag{C.3}$$

The fundamental solution of the Laplace equation in 3-D is $\frac{1}{|\mathbf{r}|}$ and it represents a singularity at the origin. The fundamental solution centered at $\mathbf{s}$, i.e. function $\frac{1}{|\mathbf{r}-\mathbf{s}|}$, satisfies (C.1) and (C.3), but it does not satisfy the boundary condition (C.2). It turns out that the sum of two shifted fundamental solutions, one centered at $\mathbf{s}$ and one centered at $\frac{\mathbf{s}R^2}{|\mathbf{s}|^2}$ and multiplied by $-\frac{R}{|\mathbf{s}|}$, satisfies (C.1), (C.2), and (C.3). Note that the second singularity is outside the sphere, i.e. there is only one singularity within the spherical domain. The solution is

$$f_{\mathbf{s}}(\mathbf{r}) = \frac{1}{|\mathbf{r}-\mathbf{s}|} - \frac{R}{|\mathbf{s}|}\frac{1}{\left|\mathbf{r}-\frac{\mathbf{s}R^2}{|\mathbf{s}|^2}\right|}, \tag{C.4}$$

or, alternatively

$$f_{\mathbf{s}}(\mathbf{r}) = \frac{1}{\sqrt{|\mathbf{r}|^2 - 2\mathbf{r}\mathbf{s} + |\mathbf{s}|^2}} - \frac{R}{\sqrt{|\mathbf{s}|^2|\mathbf{r}|^2 - 2R^2\mathbf{r}\mathbf{s} + R^4}}. \tag{C.5}$$

It is straightforward to show that (C.5) satisfies (C.1), (C.2), and (C.3). Also, $f_{\mathbf{s}}(\mathbf{r}) > 0$ when $|\mathbf{r}| < R$, $f_{\mathbf{s}}(\mathbf{r}) = 0$ when $|\mathbf{r}| = R$, and $f_{\mathbf{s}}(\mathbf{r}) < 0$ when $|\mathbf{r}| > R$. In (C.2) it is assumed that $f_{\mathbf{s}}$ is zero at the domain boundary. The zero can be replaced by a constant C by simply

adding C to $f_{\mathbf{s}}$. The gradient of $f_{\mathbf{s}}$ is

$$\nabla f_{\mathbf{s}} = \frac{\partial f_{\mathbf{s}}}{\partial \mathbf{r}} \tag{C.6}$$

$$= \frac{\mathbf{s}-\mathbf{r}}{\left(|\mathbf{r}|^2 - 2\mathbf{r}\mathbf{s} + |\mathbf{s}|^2\right)^{\frac{3}{2}}} + \frac{R\left(|\mathbf{s}|^2\,\mathbf{r} - R^2\mathbf{s}\right)}{\left(|\mathbf{s}|^2\,|\mathbf{r}|^2 - 2R^2\mathbf{r}\mathbf{s} + R^4\right)^{\frac{3}{2}}}. \tag{C.7}$$

Expression (C.7) is used in the evaluation of ∇u in (4.7).

REFERENCES

[1] N. C. for Health Statistics, "Deaths: Final report for 2003," *National Vital Statistics Reports*, vol. 54, no. 13, 2006. http://www.cdc.gov/nchs/deaths.htm.

[2] V. Fuster, W. Alexander, and R. O'Rourke, *Hurst's THE HEART*. New York: McGraw Hill, tenth ed., 2001.

[3] E. Zerhouni, D. Perish, W. Rogers, A. Yang, and E. Shapiro, "Human heart: Tagging with mr imaging - a method for noninvasive assessment of myocardial motion," *Radiology*, vol. 169, pp. 59–63, October 1988.

[4] L. Axel and L. Dougherty, "Mr imaging of motion with spatial modulation of magnetization," *Radiology*, vol. 171, pp. 841–845, June 1989.

[5] J. Delfino, M. Bhasin, R. Cole, R. Eisner, J.Merlino, A. Leon, and J. Oshinski, "Comparison of myocardial velocities obtained with magnetic phase velocity mapping and tissue doppler imaging in normal subjects and patients with left ventricular dyssynchrony," *Journal of Magnetic Resonance Imaging*, vol. 24, pp. 304–311, 2006.

[6] N. Pelc, R. Herfkens, A. Shimakawa, and D. Enzmann, "Phase contrast cine magnetic resonance imaging," *Magnetic Resonance Quarterly*, vol. 7, no. 4, pp. 229–254, 1991.

[7] D. Kim, W. Gibson, C. Kramer, and F. Epstein, "Myocardial tissue tracking with two-dimensional cine displacement-encoded mr imaging: Development and initial evaluation," *Radiology*, vol. 230, pp. 862–871, March 2004.

[8] J. Garot, J. Lima, B. Gerber, S. Sampath, K. Wu, D. Bluemke, J. Prince, and N. Osman, "Spatially resolved imaging of myocardial function with strain-encoded mr: Comparison with delayed contrast-enhanced mr imaging after myocardial infarction," *Radiology*, vol. 233, pp. 596–602, November 2004.

[9] N. Tustison and A. Amini, "Biventricular myocardial strains via nonrigid registration of anatomical nurbs models," *IEEE Transactions on Medical Imaging*, vol. 25, pp. 94–112, January 2006.

[10] R. Chandrashekara, R. Mohiaddin, and D. Rueckert, "Analysis of 3-d myocardial motion in tagged mr images using nonrigid image registration," *IEEE Transactions on Medical Imaging*, vol. 23, pp. 1245–1250, October 2004.

[11] X. Deng and T. Denney, "Three-dimensional myocardial strain reconstruction from tagged mri using a cylindrical b-spline model," *IEEE Transactions on Medical Imaging*, vol. 23, pp. 861–867, July 2004.

[12] N. Rougon, C. Petitjean, F. Preteux, P. Cluzel, and P. Grenier, "A non-rigid registration approach for quantifying myocardial contraction in tagged mri using generalized information measures," *Medical Image Analysis*, vol. 9, pp. 353–375, 2005.

[13] L. Pan, J. Prince, J. Lima, and N. Osman, "Fast tracking of cardiac motion using 3d-harp," *IEEE Transactions on Biomedical Engineering*, vol. 52, pp. 1425–1435, August 2005.

[14] A. Amini and J. Price, *Measurement of Cardiac Deformations from MRI: Physical and Mathematical Models*. Dordrecht, The Netherlands: Kluwer Academic Publishers, 2001.

[15] M. Ledesma-Carbayo, J. Kubic, M. Desco, A. Santos, M. Suhling, P. Hunziker, and M. Unser, "Spatio-temporal nonrigid registration for ultrasound cardiac motion estimation," *IEEE Transactions on Medical Imaging*, vol. 24, pp. 1113–1126, September 2005.

[16] R. Shekhar, V. Zagrodsky, M. Garcia, and J. Thomas, "Registration of real-time 3-d ultrasound images of the heart for novel 3-d stress echocardiography," *IEEE Transactions on Medical Imaging*, vol. 23, pp. 1141–1149, September 2004.

[17] D. Comaniciu, X. Zhou, and S. Krishnan, "Robust real-time myocardial border tracking for echocardiography: An information fusion approach," *IEEE Transactions on Medical Imaging*, vol. 23, pp. 849–860, July 2004.

[18] H. van Assen, M. Danilouchkine, A. Frangi, S. Ordas, J. Westenberg, J. Reiber, and B. Lelieveldt, "Spasm: A 3d-asm for segmentation of sparse and arbitrary oriented cardiac mri data," *Medical Image Analysis*, vol. 10, pp. 286–303, 2006.

[19] M. Kaus, J. von Berg, J. Weese, W. Niessen, and V. Pekar, "Automated segmentation of the left ventricle in cardiac mri," *Medical Image Analysis*, vol. 8, pp. 245–254, 2004.

[20] C. Pluempitiwiriyawej, J. Moura, Y. Wu, and C. Ho, "Stacs: New active contour scheme for cardiac mr image segmentation," *IEEE Transactions on Medical Imaging*, vol. 24, pp. 593–603, May 2005.

[21] M. Lorenzo-Valdes, G. Sanchez-Ortiz, A. Elkington, R. Mohiaddin, and D. Rueckert, "Segmentation of 4d cardiac mr images using a probabilistic atlas and the em algorithm," *Medical Image Analysis*, vol. 8, pp. 255–265, 2004.

[22] J. Montagnat and H. Delingette, "4d deformable models with temporal constraints: application to 4d cardiac image segmentation," *Medical Image Analysis*, vol. 9, pp. 87–100, 2005.

[23] E. Bardinet, L. Cohen, and N. Ayache, "Tracking and motion analysis of the left ventricle with deformable superquadrics," *Medical Image Analysis*, vol. 1, no. 2, pp. 129–149, 1996.

[24] A. Bistoquet, J. Oshinki, and O. Skinjar, "Left ventricular deformation recovery form cine mri using an inompressible model," *IEEE Transactions on Medical Imaging*, vol. 26, pp. 1136–1153, September 2007.

[25] A. Bistoquet, J. W. Parks, and O. Skrinjar, "Myocardial deformation recovery using a 3d biventricular incompressible model," (Utrecht, The Netherlands), pp. 110–119, July 2006.

[26] M. Lorenzo-Valdes, G. I. Sanchez-Ortiz, R. Mohiaddin, and D. Rueckert, "Atlas-based segmentation and tracking of 3d cardiac mr images using non-rigid registration," in *Medical Image Computing and Computer Aided Intervention (MICCAI)*, (Tokyo, Japan), pp. 642–650, 2002.

[27] D. Rueckert, L. Sonda, C. Hayes, D. Hill, M. Leach, and D. Hawkes, "Nonrigid registration using free-form deformations: Application to breast mr images," *IEEE Transactions on Medical Imaging*, vol. 18, pp. 712–721, August 1999.

[28] C. Studholme, D. Hill, and D. Hawkes, "An overlap invariant entropy measure of 3d medical image alignment," *Pattern Recognition*, vol. 32, pp. 71–86, 1999.

[29] X. Papademetris, A. Sinusas, D. Dione, R. Constable, and J. Duncan, "Estimation of 3-d left ventricular deformation from medical images using biomechanical models," *IEEE Transactions on Medical Imaging*, vol. 21, pp. 786–800, July 2002.

[30] E. Remme, K. Augenstein, A. Young, and P. Hunter, "Parameter distribution models for estimation of population based left ventricular deformation using sparse fiducial markers," *IEEE Transactions on Medical Imaging*, vol. 24, pp. 381–388, March 2005.

[31] D. Shen, H. Sundar, Z. Xue, Y. Fan, and H. Litt, "Consistent estimation of cardiac motions by 4d image registration," in *Medical Image Computing and Computer Aided Intervention (MICCAI)*, (Palm Springs, CA, USA), pp. 902–910, 2005.

[32] F. Yin, C. Chan, and R. Judd, "Compressibility of perfused passive myocardium," *American Journal of Physiol.- Heart Circ. Physiol.*, vol. 8, pp. 1864–1870, 1996.

[33] J. Hoffman and J. Spaan, "Pressure-flow relations in coronary circulation," *Physiological Reviews*, vol. 70, pp. 331–390, 1990.

[34] R. Judd and B. Levy, "Effects of barium-induced cardiac contraction on large and small vessel intramyocardial blood volume," *Circulation*, pp. 217–225, 1991.

[35] Y. Liu, R. Bahn, and E. Ritman, "Dynamic intramyocardial blood volume: Evaluation with a radiological opaque marker method," *American Journal of Physiol.- Heart Circ. Physiol.*, vol. 12, pp. 963–967, 1992.

[36] I. Vergroesen, M. Noble, and J. Spaan, "Intramyocardial blood volume change in first moments of cardiac arrest in anesthetized goats," *American Journal of Physiol.- Heart Circ. Physiol.*, vol. 4, pp. 307–316, 1987.

[37] S. Ubbink, P. Bovendeerd, T. Delhaas, T. Arts, and F. van de Vosse, "Left ventrcular shear strain in model and experiment: The role of myofiber orientation," in *Functional Imaging and Modeling of the Heart*, (Barcelona, Spain), pp. 314–324, 2005.

[38] W. Press, B. Flannery, S. Teukolsky, and W. Vetterling, *Numerical Recipes in C: The Art of Scientific Computing*. Cambrige Univeristy Press, second ed., 1992.

[39] M. Cerqueira, N. Weissman, V. Dilsizian, A. Jacobs, S. Kaul, W. Laskey, D. Pennel, J. Rumberger, T. Ryan, and M. Verani, "Standardized myocardial segmentation and nomenclature for tomographic imaging of the heart," *Journal of Applied Mathematics and Physics (ZAMP)*, vol. 4, pp. 203–210, March 2002.

[40] B. Spottiswoode, X. Zhong, A. Hess, C. Kramer, E. Meintjes, B. Mayosi, and F. Esptein, "Tracking myocardial motion from cine dense images using spatiotemporal phase unwrapping and temporal fitting," *IEEE Transactions on Medical Imaging*, vol. 26, pp. 15–29, January 2007.

[41] M. Ledesma-Carbayo, A. Santos, J. Kybic, P. Mahia-Casado, M. Garcia-Fernandez, N. Malpica, E. Perez-David, and M. Desco, "Myocardial strain analysis of echocardiographic sequences using non-rigid registration," in *Computers in Cardiology*, (Chicago, USA), pp. 31:313–316, 2004.

[42] N. Saber and H. Wen, "Construction of the global lagrangian strain field in the myocardium using dense mri data," in *26th Annual International Conference of the IEEE EMBS*, (San Francisco, CA, USA), pp. 3670–3673, 2004.

[43] J. Huang, D. Abendschein, V. Davila-Roman, and A. Amini, "Spatio-temporal tracking of myocardial deformations with a 4-d b-spline model from tagged mri," *IEEE Transactions on Medical Imaging*, vol. 18, pp. 957–972, October 1999.

[44] S. Lowitzsch, *Approximation and Interpolation Employing Divergence-Free Radial Basis Functions with Applications*. PhD thesis, Texas A&M University, May 2002.

[45] O. Skrinjar, "Mathematical properties of information theoretic image similarity measures," in *SPIE Medical Imaging*, (San Diego, CA, USA), February 2007.

[46] F. Brookstein, "Principal warps, thin-plate splines and the decomposition of deformations," *IEEE Transactions on Pattern Analysis and Machine Intelligence*, vol. 29, pp. 567–585, June 1989.

[47] M. Sermesant, K. Rhode, G. I. Sanchez-Ortiz, O. Camara, R. Andriantsimiavona, S. Hedge, D. Rueckert, P. Lambiase, C. Bucknall, E. Rosenthal, H. Delingette, D. L. G. Hill, N. Ayache, and R. Razavi, "Simulation of cardiac pathologies using an electormechanical biventricular model and xmr interventional imaging," *Medical Image Analysis*, vol. 9, pp. 467–480, Oct. 2005.

[48] M. Wierzbicki, M. Drangova, G. Guiraudon, and T. Peters, "Validation of dynamic heart models obtained using non-linear registration for virtual reality training, planning, and guidance of minimally invasive cardiac surgeries," *Medical Image Analysis*, vol. 8, pp. 387–401, Sept. 2004.

[49] H. C. van Assen, M. G. Danilouchkine, A. F. Frangi, S. Ordas, J. J. M. Westenberg, J. H. C. Reiber, and B. P. F. Lelieveldt, "Spasm: A 3d-asm for segmentation of sparse and arbitrarily oriented cardiac mri data," *Medical Image Analysis*, vol. 10, pp. 286–303, Apr. 2006.

[50] C. Lorenz and J. von Berg, "A comprehensive shape model of the heart," *Medical Image Analysis*, vol. 10, pp. 657–670, Aug. 2006.

[51] J. Lötjönen, S. Kivistö, J. Koikkalainen, D. Smutek, and K. Lauerma, "Statistical shape model of atria, ventricles and epicardium from short- and long-axis mr images," *Medical Image Analysis*, vol. 8, pp. 371–386, Sept. 2004.

[52] M. Sermesant, C. Forest, X. Pennec, H. Delingette, and N. Ayache, "Deformable biomechanical models: Application to 4d cardiac image analysis," *Medical Image Analysis*, vol. 7, pp. 475–488, Dec. 2003.

[53] P. Shi, A. J. Sinusas, R. T. Constable, and J. S. Duncan, "Volumetric deformation analysis using mechanics-based data fusion: Application in cardiac motion recovery," vol. 35, pp. 87–107, Nov. 1999.

[54] J. F. Thompson, B. K. Soni, and N. P. Weatherill, *Handbook of Grid Generation*. Boca Raton, Florida: CRC Press, first ed., 1998.

[55] V. D. Liseikin, *Grid Generation Methods*. Berlin, Germany: Springer, first ed., 1999.

[56] E. Lorensen and H. Cline, "Resolution 3d surface construction algorithm," *Computer Graphics*, vol. 21, no. 4, pp. 163–169, 1987.

[57] G. Taubin, "Curve and surface smoothing without shrinkage," in *International Conference on Computer Vision*, (Boston, MA), pp. 852–857, June 1995.

[58] W. J. Schroeder, J. A. Zarge, and W. E. Lorensen, "Decimation of triangle meshes," *Computer Graphics*, vol. 26, pp. 65–70, July 1992.

[59] H. Hoppe, T. DeRose, T. Duchamp, J. McDonald, and W. Stuetzle, "Mesh optimization," *Computer Graphics*, vol. 27, pp. 19–25, 1993.

[60] E. J. Bekkers and C. A. Taylor, "Multiscale vascular surface model generation from medical imaging data using hierarchical features," *IEEE Transactions on Medical Imaging*, vol. 27, pp. 331–341, Mar. 2008.

[61] J. Peiro, L. Formaggia, and M. Gazzola, "Shape reconstruction from medical images and quality mesh generation via implicit surfaces," *International Journal for Numerical Methods in Fluids*, vol. 53, pp. 1339–1360, 2007.

[62] J.-O. Lachaud and A. Montanvert, "Defornable meshes with automated topology changes for coarse-to-fine three-dimensional surface extraction," *Medical Image Analysis*, vol. 3, pp. 187–207, June 1999.

[63] J. Lötjönen, P.-J. Reissman, I. E. Magnin, J. Nenonen, and T. Katila, "A triangulation method of an arbitrary point set for biomagnetic problems," *IEEE Transactions on Magnetics*, vol. 34, pp. 2228–2233, July 1998.

[64] S. F. F. Gibson, "Constrained elastic surface nets: Generating smooth surfaces from binary segmented data," in *Medical Image Computing and Computer Aided Intervention (MICCAI)*, (Cambridge, MA), pp. 888–898, Oct. 1998.

[65] A. B. Ekoule, F. C. Peyrin, and C. L. Odet, "A triangulation algorithm from arbitrary shaped multiple planar contours," *ACM Transactions on Graphics*, vol. 10, pp. 182–199, Apr. 1991.

[66] D. Meyers, S. Skinner, and K. Sloan, "Surfaces from contours," *ACM Transactions on Graphics*, vol. 11, pp. 228–258, July 1992.

[67] M. Ziólkowski and H. Brauer, "Methods of mesh generation for biomagnetic problems," *IEEE Transactions on Magnetics*, vol. 32, pp. 1345–1348, May 1996.

[68] J.-Y. Lai, J.-L. Doong, and C.-Y. Yao, "Three-dimensional cad model reconstruction from image data of computer tomography," *International Journal of Imaging Systems and Technology*, vol. 10, pp. 328–338, July 1999.

[69] I. N. Bronshtein and K. A. Semendyayev, *Handbook of Mathematics*. Berlin, Germany: Springer, third ed., 1998.

[70] E. B. Saff and A. B. J. Kuijlaars, "Distributing many points on a sphere," *Mathematical Intelligencer*, vol. 19, no. 1, pp. 5–11, 1997.

[71] A. Katanforoush and M. Shahshahani, "Distributing points on the sphere, i," *Experimental Mathematics*, vol. 12, no. 2, pp. 199–209, 2003.

[72] T. Erber and G. M. Hockney, "Equilibrium configurations of n equal charges on a sphere," *Journal of Physics A: Mathematical, Nuclear and General*, vol. 24, pp. L1369–L1377, Dec. 1991.

[73] L. Glasser and A. G. Every, "Energies and spacings of point charges on a sphere," *Journal of Physics A: Mathematical, Nuclear and General*, vol. 25, pp. 2473–2482, May 1992.

[74] J. O'Rourke, *Computational Geometry in C*. Cambridge, UK: Cambridge University Press, second ed., 2001.

[75] G. Wahba, "Spline interpolation and smoothing on the sphere," *SIAM Journal Sci. Stat. Comput.*, vol. 2, pp. 1–15, 1981.

[76] G. Turk and J. O'Brien, "Modelling with implicit surfaces that interpolate," *ACM Transactions on Graphics*, vol. 21, pp. 855–873, Oct. 2002.

[77] E. Hartmann, "A marching method for the triangulation of surfaces," *The visual computer*, vol. 14, pp. 95–108, July 1998.

[78] T. Karkanis and A. J. Stewart, "Curvature-dependent triangulation of implicit surfaces," *IEEE Computer Graphics and Applications*, vol. 21, pp. 60–69, March/April 2001.

[79] S. Akkouche and E. Galin, "Adaptive implicit surface polygonization using marching triangles," *COMPUTER GRAPHICS forum*, vol. 20, pp. 67–80, June 2001.

[80] A. Duci, A. Yezzi, S. Soatto, and K. Rocha, "Harmonic embeddings for linear shape analysis," *Journal of Mathematical Imaging and Vision*, vol. 25, pp. 341–352, Oct. 2006.

[81] S. Angenent, S. Haker, A. Tannenbaum, and R. Kikinis, "On the laplace-beltrami operator and brain surface flattening," *IEEE Transactions on Medical Imaging*, vol. 18, pp. 700–711, Aug. 1999.

[82] G. Holzapfel, *Nonlinear Solid Mechanics*. Chichester: Wiley, 2000.

[83] J. Meinguet, "Multivariate interpolation at arbitrary points made simple," *Journal of Applied Mathematics and Physics (ZAMP)*, vol. 30, pp. 292–304, March 1979.

[84] M. do Carmo, *Differential Geometry of Curves and Surfaces*. Englewood Cliffs, New Jersey: Prentice Hall, 1976.